

Microwave Surfing

Wrath of Grapes Redux

■ Rajeev Bansal

YouTubers have gone grape crazy. In a plethora of Internet videos, kitchen scientists have cut a grape almost in half—leaving just a strip of skin connecting the two sides—and stuck it in the microwave. In seconds, sparks erupt [1].

As I wrote in a previous column [2], [3], the quote comes from an article in *Science* [1], which even included a link to an impressive video demonstration of the phenomenon, accompanied by rousing music. However, for a long time, a proper scientific explanation for this crowd pleaser was missing. That changed in 2019 with the publication of an article [4] in the *Proceedings of the National Academy of Sciences (PNAS)*. Canadian physicists Khattak, Bianucci, and Slepko claimed to have cracked the problem:

This work ties the source of the plasma to microwave photonic hotspots at the junction of aqueous dielectric spherical dimers. We use

Rajeev Bansal (rajeev.bansal@uconn.edu) is with the University of Connecticut, Storrs, Connecticut, 06269, USA.

Digital Object Identifier 10.1109/MMM.2021.3131836
Date of current version: 3 February 2022

a combination of thermal-imaging techniques and computer simulations to show that grape-sized fruit and hydrogel beads form resonant cavities that concentrate electromagnetic fields to extreme subwavelength regions. This is enabled by the large dielectric susceptibility of water at microwave frequencies. Furthermore, the absorptive properties of water are key to washing out complex internal modes and for allowing the evanescent hotspot build-up [4].

The *PNAS* article generated much public interest worldwide and was listed among the *PNAS* “top 10 stories of 2019” [5]. However, not everyone was convinced. Now a team of physicists from Taiwan has proposed a different mechanism in a *Physics of Plasmas* article [6] to explain the sparks in the narrow gap between the two grape halves. Prof.

Editor’s Note: An earlier version of this column appeared originally in the February 2022 issue of *IEEE Antennas and Propagation Magazine*.



©IMAGE LICENSED BY INGRAM PUBLISHING

Chu and his colleagues find the mechanism to be electrical in nature (\pm polarization charge buildup across the gap). As Prof. Chu wrote to me in an e-mail:

*The “electromagnetic hotspot” proposed in the *PNAS* paper and the “electrical hotspot” in our study have entirely different physical origins. So it’s relatively simple to check which one has really caused the sparks. For example, the former would produce a radiation pressure to repel the two grapes, while the latter would produce an electrical force to attract them. As shown in our video (https://youtu.be/ACWp9_vc2aY), the attractive force between the grapes convincingly establishes the validity of the electrical origin.*

(continued on page 86)



IMS2022 PREVIEW

19-24 June 2022

DENVER • COLORADO

IMS & RFIC KEYNOTES



Dr. Curtis Ling
Founder and CTO, MaxLinear



Prof. Sorin Voinigescu
University of Toronto



Prof. Dana Z. Anderson
Fellow of the JILA Institute and Dept.
of Physics, University of Colorado, Founder
and CTO of ColdQuanta, Inc.



Gregory E. Edlund
Vice President and Chief Architect,
Lockheed Martin Space
Systems Company



Prof. W. Bernard Carlson
Vaughan Professor of Humanities
Department of Engineering and Society,
University of Virginia, TechInnovate, National
University of Ireland Galway

Mark Your Calendar! Registration will open February 2022!



For the latest information, visit: ims-ieee.org



IMS2022 Week – AT A GLANCE

	Sunday 19-Jun-22	Monday 20-Jun-22	Tuesday 21-Jun-22
Workshops & Short Courses			
Technical Lectures			
RFIC Plenary Session, Reception, Industry Showcase			
Quantum Bootcamp			
RF Bootcamp			
RFIC Technical Sessions and Interactive Forum			
Three Minute Thesis			
IMS Plenary Session and Welcome Reception			
IMS Technical Sessions and Interactive Forum			
Panel Sessions			
Connected Future Summit			
Exhibition			
MicroApps and Industry Workshops			
Amateur Radio Talk and Reception			
Young Professionals Talk and Reception			
Industry Hosted Reception			
Women In Microwaves Talk and Reception			
IMS Closing Ceremony and Awards			
99th ARFTG			

Tell Your Boss You Want to Attend IMS!
 Use the *At a Glance* to plan your week!



Wednesday
22-Jun-22

Thursday
23-Jun-22

Friday
24-Jun-22

- Workshops
- Technical Lectures
- RFIC
- Bootcamp
- Three Minute Thesis
- IMS
- Panel Sessions
- Connected Future Summit
- Exhibitor Activities
- Focus Groups
- ARFTG

Schedule subject to change, visit ims-ieee.org for the most up to date information

New for 2022: The Systems Forum

With a special focus on systems design across three days, The Systems Forum includes technical topics showcased in the Connected Future Summit, panel sessions, focused sessions, and an interactive Systems Pavilion on the show floor.

TUESDAY

**Connected
Future Summit
and Quantum
Systems**

WEDNESDAY

**Radar and
Aerospace**

THURSDAY

**Phased
Arrays and
Over-the-Air**

For the latest information, visit: ims-ieee.org

Exhibitor

List

3D Glass Solutions Inc
3G Shielding Specialties
3RWAVE
A-Alpha Waveguide Inc.
ACE-Accurate Circuit Engineering
ACEWAVETECH
Advanced Assembly
Advanced Circuitry International
Aerospace & Defense Technology
AGC Multi Material America Inc.
Agile Microwave Technology Inc.
AI Technology Inc.
AJ Tuck Co.
Akoustis Inc.
ALMT Corp.
Altum RF
American Microwave Corp.
American Standard Circuits Inc.
Ampleon
AmpliTech Inc.
Analog Devices Inc.
AnaPico Inc.
Anoisson Electronics LLC
Anokiwave
Anritsu Co.
Ansys
APITech
AR RF/Microwave Instrumentation
Artech House
ASI CoaxDepot
Astronics Test Systems
AT Wall Company
Atlanta Micro Inc.
Auden Techno
B&Z Technologies
Barry Industries Inc.
Cadence Design Systems Inc.
Cernex/Cernexwave
Charter Engineering Inc.
Ciao Wireless Inc.
Cicor Group
Cinch Connectivity Solutions
CML Microcircuits
Colorado Engineering Inc.
Colorado Microcircuits Inc.
Communications & Power Industries
Component Distributors Inc.
Connectronics Inc.
Copper Mountain Technologies
Corning Inc.
Corry Micronics LLC a Quantic Company
Crane Aerospace & Electronics
Criteria Labs Inc
Crystek Corp.
CTT Inc.
Cubic Nuvotronics
Custom Cable Assemblies Inc.
CW Swift & Associates Inc.
CX Thin Films
Dassault Systemes SIMULIA
dB Control
Delta Electronics Mfg. Corp.
Denka Corporation
DeWeyl Tool Company
Diamond Antenna & Microwave Corp.
Diramics
DiTom Microwave Inc.
Doosan Electro Materials
dSPACE Inc.
Eclipse MDI
Element Six
Elite RF
EM Labs Inc.
Empower RF Systems Inc.

EMSS Antennas
Eravant
ETL Systems Ltd.
ETS-Lindgren
European Microwave Week
Evans Capacitor Company
Everything RF/Microwaves 101
evispaP Inc
F&K Delvotec Inc.
Filtronics Inc.
Filtronic Broadband
Fine-Line Circuits Limited
Flann Microwave Ltd.
Flexco Microwave Inc.
Focus Microwaves Inc.
FormFactor Inc.
Fortify
Frontynk Technologies Inc.
Geib Refining Corp.
General Microwave Corporation
GGB Industries Inc.
Global Communication Semiconductors
GLOBALFOUNDRIES
Gowanda Components Group (GCG)
Guerrilla RF
Harbour Industries LLC
HASCO INC
Hermetic Solutions Group
Herotek Inc.
Hesse Mechatronics
High Frequency Electronics
HRL Laboratories LLC
HYPERLABS
IHP GmbH
IMST GmbH
InCompliance Magazine
Indium Corp.
Innertron Inc.
Innovative Power Products Inc.
In-Phase Technologies Inc.
Integra Technologies Inc.
Intellconnect LLC
International Manufacturing Services Inc.
inTEST Thermal Solutions
Ironwood Electronics
Isola / Insulectro
ITF Co. Ltd.
IWWorks Co. Ltd.
IW Microwave Products
JFW Industries Inc.
Johanson Technology Inc.
JQL Technologies Corporation
Junkosha Inc.
Keysight Technologies
Knowles Precision Devices
KOSTECSYS Co. Ltd.
KRYTAR
KVG Quartz Crystal Technology GmbH
Kyocera AVX
Kyocera International Inc.
L3Harris Technologies
LadyBug Technologies LLC
Lake Shore Cryotronics Inc.
Laser Processing Technology Inc.
Leader Tech Inc.
Liberty Test Equipment Inc.
Linearizer Technology Inc.
Logus Microwave
LPKF Laser & Electronics
M2 Global
MACOM
Marki Microwave Inc.

Maury Microwave
MaXentric Technologies LLC
MCV Microwave
Measure Tech Inc.
MECA Electronics Inc.
Mega Circuit Inc.
MegaPhase
Menlo Microsystems Inc.
Mercury Systems
Metamagnetics Inc.
Mician GmbH
Micro Harmonics Corporation
Micro Lambda Wireless Inc.
MicroFab Inc.
Micro-Mode Products Inc.
Microsanj LLC
Microwave Applications Group
Microwave Engineering Corp.
Microwave Journal
Microwave Product Digest
Microwave Products Group
Microwave Techniques LLC
Microwaves & RF
Millimeter Wave Products Inc.
Milliwave Silicon Solutions Inc.
Mini-Circuits
Mini-Systems Inc.
Mitsubishi Electric US Inc.
Modelithics Inc.
Modular Components National
Morion US LLC
Mouser Electronics Inc.
MPI Corp.
MRSI Systems, Myconic
MtronPTI
Muegge Gerling
NDK America
Netcom Inc.
Networks International Corp.
NI
Ningbo Somefly Technologies
Norden Millimeter Inc.
Northrop Grumman
NuWaves Engineering
Nxbeam Inc.
Ohmega Technologies
Ophir RF Inc.
Optomec
Orbel Corp.
Orolia USA
Pasquali Microwave Systems
Passive Plus Inc.
Pasternack
Pickering Interfaces
Piconics Inc.
Planar Monolithics Industries
Plymouth Rock Technologies
PM Industries Inc.
Polyfet RF Devices
PPG Cuming Microwave
Presidio Components Inc.
PRFI Ltd.
pSemi Corporation
Q Microwave Inc.
Qorvo
QP Technologies
Quest Microwave Inc.
QuinStar Technology Inc.
R&K Company Limited
Rapidtek Technologies Inc.
Reactel Inc.
RelComm Technologies Inc.
Remtec Inc.
Renaissance Electronics/HXI
Renesas Electronics America Inc
Res-Net Microwave
Response Microwave Inc.
RF Globalnet
RF Morecom Corea
RF-Lambda USA LLC
RFMW
Richardson Electronics Ltd.
Richardson RFPD
RJR Technologies Inc.
RLC Electronics Inc.

Rogers Corp.
Rohde & Schwarz USA Inc.
Rosenberger North America
Samtec Inc.
San-tron Inc.
Sawnics Inc.
Schmid & Partner Engineering AG
Scientific Microwave Corp.
SemiDice (Microcross Components)
SGMC Microwave
Siglent Technologies NA
Signal Hound
Signal Microwave
SignalCore Inc.
Skyworks Solutions Inc.
Smiths Interconnect
SOMACIS
Sonnet Software Inc.
Southwest Microwave Inc.
Space Machine & Engineering Corp.
SRTechnology Corp.
SSI Cable Corporation
Starwave Sdn Bhd
State of the Art Inc.
Statek Corp.
Stellar Industries Corp.
StratEdge Corp.
Sumitomo Electric Device Innovations
Sung Won Forming
SuperApex Corporation
Susumu International (USA) Inc.
SV Microwave
Switzer
SynMatrix Technologies Inc.
Tagore Technology Inc.
Tai-Saw Technology Co. Ltd.
Taitien
Teccia Inc.
Teledyne Technologies
Telegartner Inc.
Telonic Berkeley Inc.
TEVET
Texas Instruments
The Boeing Company
The Goodsystem Corp.
TICRA
Times Microwave Systems
TMY Technology Inc.
Tower Semiconductor
TPT Wire Bonder
Transcat Inc.
Transcom Inc.
Transline Technology Inc.
TRM Microwave
TRS-RenTelco
TTM Technologies
Ulbrich Specialty Wire Products
Ultra
UTE Microwave Inc.
Varioprint AG
Vaunix Technology Corp.
Virginia Diodes Inc.
Vishay Intertechnology Inc.
Waka Manufacturing Co.Ltd.
WAVEPIA Co. Ltd.
Wavice
Weinschel Associates
Wenzel Associates Inc.
Werlatone Inc.
West Bond Inc.
WIN Semiconductors Corp.
Winchester Interconnect
WIPL-D
Wireless Telecom Group
Withwave Co. Ltd
WL Gore & Associates Inc.
Wolfspeed Inc.
XMA Corporation
X-Microwave
Xpedic Technology Inc.

Exhibitor List is accurate
at time of release



Awards

MTT-S Honorary Life Members: A Short History

■ Józef Modelski

The highest purpose of the Honorary Life Member is to recognize and honor a deserving Society participant. Of equal importance are the continuity of purpose, intent, and corporate memory encouraged by the Honorary Life Member designation, thus helping to institutionalize the highest motives and objectives that have always been present within the MTT-S.

MTT-S Bylaw 3.3.2.1

The Honorary Life Member (HLM) is given to an individual of national and international prominence who has performed outstanding service to the profession and the IEEE Microwave Theory and Techniques Society (MTT-S) and whose contributions, technical or otherwise, have made an important impact in the field of interest of the Society (particularly those made after finishing service as an elected Administrative Committee [AdCom] member). Furthermore, this award carries the



©IMAGE LICENSED BY INGRAM PUBLISHING

expectation that the candidate will continue to contribute to the Society and participate in its activities as an individual contributor, as an advisor, and/or by serving on Society ad hoc and standing committees (<https://mtt.org/honorary-life-members/>).

It is interesting to look at the list of HLMs in Table 1 in the Society's history. As I said in *IEEE Microwave Magazine* in 2008, when I was MTT-S president (the first one not living and working in the United States), "Our Society is a gift of American microwave engineers to the world," because the birth of microwaves had a very strong U.S. base. Since my tenure as

the president, there have been five other MTT-S presidents from outside the United States, and the sixth has been just chosen as president-elect. It is a sign that, each year, the MTT-S becomes more international. In my opinion and without any exaggeration, our Society has become truly transnational in the last decade.

What makes this Society so influential in the professional life of so many microwave engineers around

TABLE 1. The HLMs of the MTT-S.

George C. Southworth	1960
Andre G. Clavier	1961
William W. Mumford	1965
Alfred C. Beck	1967
Donald D. King	1973
Theodore S. Saad	1973
Kiyo Tomiyasu	1978
Seymour B. Cohn	1978
Arthur A. Oliner	1978
Leo Young	1982
Tatsuo Itoh	1994
Peter W. Staecker	2006
Richard A. Sparks	2014
John T. Barr	2017
Józef Modelski	2019

Józef Modelski (modelski@ieee.org) is with the MTT-S Administrative Committee.

Digital Object Identifier 10.1109/MMM.2021.3131946

Date of current version: 3 February 2022

the world? What feeds its continuing vitality? First, it was established for the pursuit of a very noble goal: the creation and dissemination of knowledge. Second, it was established as a self-governing volunteer organization, with its members committing themselves to the highest ethical and professional conduct (see the IEEE Code of Ethics). Third, it is a nonprofit, nongovernmental organization working for a greater common good that is self-financed by its scientific, literary, and educational activities. Therefore, it may offer and propagate unbiased opinions based only on scientific evidence. The Society's publication

policies make MTT-S journals open to contributions from all countries around the world, with editorial judgment based on merit alone.

In short, our professional society is based on principles in common with what, in political science, is called a *civic society*; therefore, I think it is important to restate again these simple and obvious values. However, these obvious truths are still not at all manifest in many countries around the globe. At the top of Table 1, we can see founders ("fathers") of our Society. Unfortunately, in the past decade, many of our great HLMs passed away.

Newly Selected MTT-S HLMs

On 10 October 2021, in the 69th year of the Society's existence, the MTT-S AdCom selected simultaneously by acclamation Manfred (Fred) Schindler and Richard (Dick) Snyder as HLMs. For the first time since the 1970s, we have selected more than one new HLM. This proves again that our Society is lucky to have many great individuals who have been successfully continuing the mission of our founders. I have the great honor and pleasure to present Dick's and Fred's biographies in this issue of *IEEE Microwave Magazine*.

Manfred (Fred) Schindler: MTT-S Honorary Life Member

■ Józef Modelski

Fred Schindler (Figure 1) was born in the spring of 1957 in Vienna, Austria. That summer, the family moved to Dayton, Ohio, when his father, Max, took a position with the Air Force at Wright Labs. One year later, the Schindlers moved to New Jersey when Max took a job designing microwave electron tubes for the Radio Corporation of America. Maximilian Josef Schindler and Manfred Johannes Schindler shared initials, which would subsequently result in Max's publications occasionally being credited to Fred, who was not, in fact, an engineering prodigy in kindergarten.

The family eventually settled in Boonton, New Jersey, where Fred grew up with older brother Chris and younger brother Norbert. The boys and their mother, Dudy, spent many summers in her hometown of



©SHUTTERSTOCK.COM/BLACK MOON

Kufstein, a small alpine city in Austria. His Austrian heritage left Fred with an affection for skiing, hiking, and beer. Dudy, who had paused her studies when she was married, earned her M.S. degree in library science at Rutgers University. Fred became enamored with electronics at an early age, building and repairing various devices. The family's first color television set was a discarded one that he picked up and repaired.

Fred enrolled in the Columbia University School of Engineering in 1975, earning his B.S.E.E. degree

in June 1979. At Columbia, Fred met Marcia Felth, who lived across the hall in their dorm. Marcia wasn't impressed with Fred's homemade stereo system and its massive speakers, but she eventually found other charming qualities in him. Marcia moved to Vermont to earn her master's degree in 1977, with Fred making frequent visits. This cemented their lasting affection for Vermont.

Upon completing their degrees in 1979, Fred and Marcia moved to the



Figure 1. Fred Schindler.

Digital Object Identifier 10.1109/MMM.2021.3131902
Date of current version: 3 February 2022

Józef Modelski (modelski@ieee.org) is with the MTT-S Administrative Committee and was assisted by Marcia Felth in preparing this column.

Boston, Massachusetts, area and eventually settled in Newton, Massachusetts. They married in 1982 and have three children, Anna, Eric, and Greta (Figure 2). Anna is a community college math professor, Eric is an established musician in Boston, and Greta is a psychology major working in human resources for a technology company. Marcia started her career as a manager in technology companies and is now the development manager for Young Man With a Plan, a mentoring program supporting the achievement of young men of color in Boston schools.

Fred started working at Raytheon in a communications lab in 1979. It was an upbeat time in engineering, coming out of a slowdown spurred by the end of the Vietnam War and winding down of the Apollo program. In 1980, Raytheon invited Fred to participate in the new Raytheon UMass microwave engineering program, to earn an M.S.E.C.E. degree by spending a year on the Amherst, Massachusetts, campus. Fred was awarded his degree in 1982, one of six Raytheon Microwave Scholars in that initial class.

Shortly after earning his M.S. degree, Fred was assigned to Raytheon's Research Division to work on 44-GHz gallium arsenide (GaAs) IMPATT amplifiers. In 1984, he transferred to the group developing GaAs MMIC technology. Raytheon was an early innovator in this technology, and Fred had the opportunity to work with and for



Figure 2. Fred Schindler and his family: Anna, Greta, Eric, and Marcia.

well-know pioneers, including Bob Pucel, Yalcin Ayasli, Yusuke Tajima, and Bob Bierig. The next several years were, for Fred, a period of significant technical and professional growth. Most of his technical papers and all of his patents came out of this period. A circuit he developed for a 6–18-GHz phase shifter remains widely used today. He made several contributions to broadband amplifier technology. His dc 40-GHz MMIC switch is included in the IEEE Microwave Theory and Techniques Society (MTT-S) MMIC Historical Exhibit. Fred was

elevated to IEEE Fellow in 2019 “for developments in microwave switch technology for radar and wireless communications systems,” for work primarily done in this period.

Fred's management responsibilities grew at the Research Division, and he led multiple research programs. He recognized the need to develop more microwave engineers and sent several to UMass Amherst to study in its Raytheon Microwave Engineering program.

Fred was the manager of the Microwave Circuits Research Lab when



Figure 3. The Qorvo Design Center, Boston, 2014.

Raytheon closed its Research Division in 1994. He moved his entire organization to a commercial operation in Andover, Massachusetts. In 1996, he left Raytheon to become the engineering manager at ATN Microwave. ATN specialized in microwave test systems and technology, including device characterization, multipoint analyzers, and electronic calibration. In 1998, he became the applications manager for IBM's wireless products business, which was commercializing SiGe technology.

In 1999, Fred received a call from his former Raytheon colleague Leonard Reynolds, who had joined RF Micro Devices (RFMD) in North Carolina a few years earlier. RFMD was seeking someone to start a design center in Boston, with its pool of microwave engineering talent. Within weeks, Fred was in North Carolina, interviewing with RFMD Chairman and CTO Bill Pratt. RFMD offered Fred the job, and, by the 1999 International Microwave Symposium (IMS) in Anaheim, California, Fred was handing out RFMD business cards.

Fred worked out of his home while he hired staff and looked for office and lab space. For many years, he had been taking a mid-day run, a break during which he solved numerous technical problems. Now, lunchtime was for meetings with job candidates, and runs were relegated to the morning. By November 1999, Fred had hired five engineers and moved into a temporary office space. By January 2000, the RFMD Boston Design Center employed 14 people and moved into an 8,600-ft² (800-m²) space in Billerica, Massachusetts. By June 2000, the design center staff was more than 25 people, and, anticipating further growth, the facility was doubled in size.

Some of Fred's employees in Billerica had started bike commuting to work, and, in 2008, realizing that many of them lived farther from the office than he did, Fred gave it a try. That 26-km (16-mi) commute was just a start. Fred became an enthusiastic cyclist and has logged well over 50,000 km (31,000 mi) since.

Fred continued with RFMD for 19 years, including after its 2015 merger to create Qorvo. His talented teams developed a wide range of products for cellular handsets, Wi-Fi products, and wireless and wired infrastructure. The products developed in his design center sold in the billions, generating billions in revenue. The technology he helped develop in the 1980s now was mainstream. Fred was able to find, hire, and develop many talented engineers at RFMD. His close connections with engineering faculties around the world, including at UMass Amherst, played an important role in the success of the design center (Figure 3).

In 2018, Fred left Qorvo and has been working as an independent consultant and the CTO of Anlotek Ltd. In his consultancy work, he has performed due diligence for potential acquisitions, served as an expert witness, and managed engineering projects.

Fred's volunteer work with the MTT-S and IEEE began in the 1980s. In 1992, at the recommendation of Bob Pucel, MTT-S President-Elect Peter Staecker invited Fred to serve as



Figure 4. The IMS2009 Chair's Dinner: (back row) John Osepchuk, Fred Schindler, George Oltman, and Barry Pearlman as well as (front row) Kiyo Tomiyasu, Theodore Saad, Arthur Oliner, and Robert Rivers.

the 1993 MTT-S secretary. Meeting agendas and minutes were still distributed to the MTT-S Administrative Committee (AdCom) via conventional mail. Fred's innovation as secretary was to collect email addresses for all of the AdCom members and begin using email for secondary communications. Fred was elected to the AdCom that year, and, when his first term began in 1994, he was the first chair of the Electronics Communications Ad Hoc Committee, the predecessor of the Electronic Information Committee. Fred served three terms on the AdCom and chaired a number of committees, including Membership Services (now Member and Geographic Activities), Operations, Marketing and Publicity (then an ad hoc committee), and Meetings and Symposia (which still had oversight of the IMS).

In 2000, the IMS returned to Boston. Peter Staecker served as the technical program chair and Fred was the vice chair. This was the first year the IMS accepted electronic paper submissions. Authors were also given the option of submitting a hard copy via mail. In the end, out of 845 total submissions (a record at the time), 841 were submitted electronically.

Fred was chosen as the 2002 vice president. The president that year, John Barr, tasked Fred with developing a plan for a second major conference. They decided on an event in January, coinciding with an AdCom meeting and the IMS Technical Program Review Committee meeting. It launched in 2006 with Fred as the general chair. That first IEEE Radio & Wireless Week (RWW) was held in San Diego and included the IEEE Radio and Wireless Symposium (which grew out of RAWCON); the University of California, San Diego-based PA Symposium; the established Si RF Conference, and a trade show. While the ambitions were grand, the outcome was modest. Fred chaired the RWW Executive Committee 2005–2007 and 2014–2015, and RWW developed into a stable ongoing event. Fred served as a member of the European Microwave Association

Steering Committee 2007–2008 and continues to serve as an associate editor of its *International Journal of Microwave and Wireless Technologies*.

In 2007, the MTT-S opened its IMS exhibition management contract for bids, starting with IMS2009. The 2007 MTT-S president, Steve Kenney, appointed Fred the chair to select a vendor and negotiate a contract. The committee recommended MP Associates as well as a contract arrangement that gave the MTT-S greater financial responsibility and required new budgeting and financial operations to be in place for IMS2009.

Fred was the general chair for IMS2009, held in the new Boston Convention and Exhibition Center (Figure 4). The conference came in the wake of the Great Recession and the shadow of the H1N1 "swine flu" pandemic. After a Boston area outbreak in May, some countries, notably Japan, restricted their citizens from attending. IMS2009 went on as planned, though it failed to maintain Boston's tradition of breaking records.

Following IMS2009, Fred continued serving the MTT-S in various capacities, including as chair of the IMS Executive Committee and MTT-19, the Technical Committee on Microwave Business Issues. With this, he became the editor for the "MicroBusiness"

column in *IEEE Microwave Magazine*. Finding it was easier to write the articles himself than find contributors, Fred has written the column ever since. In 2016, a set of his columns received the Apex Award of Excellence. In 2015, Fred received the MTT-S N. Walter Cox Award and, in 2018, the Distinguished Service Award.

In 2013, MTT-S President Madhu Gupta nominated Fred to serve on the IEEE Conferences Committee (ICC), which has oversight of policy and procedures for all IEEE-sponsored conferences. Fred was selected, and, as his two-year term was ending, he applied for reappointment. This time,

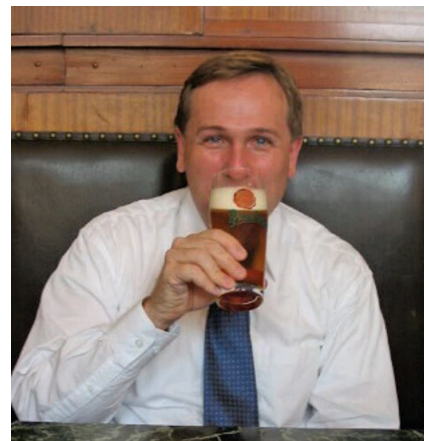


Figure 5. Fred Schindler and a beer in Prague.



Figure 6. The 2019 Region 10 Conference Leadership Workshop in Goa, India. Fred Schindler (right) is with Celia Shahmaz and Deepak Mathur.

Fred was not selected, but I (then the Division IV director) convinced him to instead stand for chair of the ICC. Fred reluctantly agreed, and I nominated him from the floor of the IEEE Technical Activities Board (TAB) meeting. Fred replaced the traditional headshot in his nomination with a photo of himself enjoying a glass of pilsner in Prague (Figure 5). He made a brief presentation to the TAB; answered questions, including some about beer; and left to visit his parents, certain that one of the other candidates would win. To his great surprise, when he arrived in Boonton, he received a message of congratulations.

Fred served two rewarding terms as the chair of the ICC from 2015

to 2018. He focused on increasing engagement with conference organizers and sponsors, growing committee member involvement, and improving collaboration across IEEE. The ICC evolved from a group that met three times a year to listen to some reports into a well-organized body with subcommittees focused on key topics. One of these, conference quality, is an area where Fred continues to provide leadership and training (Figure 6).

One of the roles of the ICC chair is to serve as the host of IEEE's conference about conference, first called POCO and then Convene. In keeping with Fred's tastes, beer has had a prominent

place at every POCO/Convene. POCO 2016 was held in Montreal, with a reception at Cirque Éloize. Fred was lowered in a harness from the third floor, above the reception, giving him a chance to perform some aerobatics (<https://www.youtube.com/watch?v=zwcXmKsW4lc>).

In 2019, Fred was elected to the IEEE Board of Directors as the Division IV director. He continues to serve on committees of the Board, TAB, ICC, and Products and Services Committee as well as in various capacities in the MTT-S.

Fred has been a major contributing force to the MTT-S, and we look forward to that continuing. Congratulations, Fred!

Richard V. Snyder: MTT-S Honorary Life Member

■ Józef Modelski

Dick Snyder (Figure 1) was born in Brooklyn, New York, in December 1939. His family relocated to Santa Monica, California, in 1944. He was the oldest son of a lawyer and a Juilliard-trained classical pianist, accomplished people who cherished education and nurtured Dick's talents and abilities. (He practiced the piano at 6 a.m. from the time he was about five years old.) As a child, he adored his grandfather, who taught him to read at three years old and gave him a love of learning. Grandpa was also an engineer, educated at Cooper Union, and introduced his grandson to math. (Dick still has Grandpa's



©SHUTTERSTOCK.COM/BLACK MOON

old wooden logarithmic slide rule in his desk.)

Dick was a precocious youth and advanced two grades ahead of his peers in his elementary school years. He loved sports, music, school, homework, and learning everything he could, but he had a particular penchant for math and science (particularly

chemistry and astronomy). Fancying himself a junior chemist early on, he would perform experiments in his very well-equipped garage laboratory, often to his mother's dismay. Once, he even blew up—accidentally (?)—a

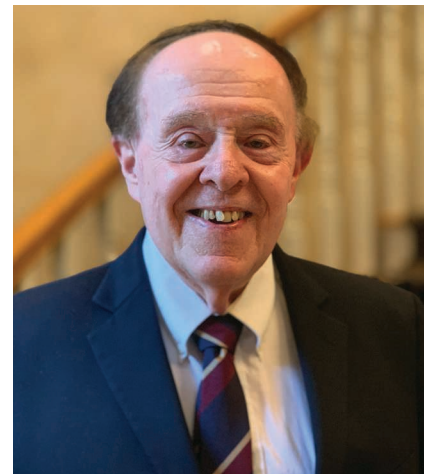


Figure 1. Dick Snyder.

Józef Modelski (modelski@ieee.org) is with the MTT-S Administrative Committee and was assisted by Valerie Snyder in preparing this column.

Digital Object Identifier 10.1109/MMM.2021.3131948
Date of current version: 3 February 2022

mailbox with nitroglycerin in a Halloween prank. He built telescopes, made evening pilgrimages to the Griffith Park observatory (his dad being a willing source of transportation), and went to local chemical supply companies to stock his home laboratory. He became a licensed “radio ham” at 13, participating in DX contests and running what was then known as a *California kilowatt*, i.e., extra transmitter power.

As with most budding engineers, Dick enjoyed building electronic gadgets, and he always tried for a bit more performance than others. He thought he would become a great scientist or chemist one day. Having graduated from high school early, he went on to Loyola University in California, majoring in electrical engineering, and took part in the Air Force Reserved Officer Training Program. He was permitted to continue on to graduate school at the University of Southern California for a master’s degree in electrical engineering before taking his Air Force commission.

After his military service, Dick worked as an engineer at what was then ITT-Gilfillan, but he did not feel sufficiently challenged. He published his first paper in *Proceedings of the IEEE* in 1967, and that was an adventure. During the review process, Dick received a phone call from Dr. Leo Young, telling him he had talent and, in unequivocal language, also telling him that improvement was seriously needed. However, it worked out pretty well, and the article on low-pass filters was published. Later, he met Prof. Arthur Oliner and Dr. Harold Seidel at a microwave conference in Detroit [the 1968 PGMTT, the predecessor of the IEEE International Microwave Symposium (IMS)] and was convinced to “go East” to work for a small company (Merrimac Research) and enroll in a Ph.D. program at New York Polytechnic University (then known as Brooklyn Poly). Electrophysics, network theory applied to filters and in general, and microwave engineering became his passions.

Dick became active in the North Jersey IEEE Section, and, when the 1976 IMS in Cherry Hill was in the planning stages, he acted as secretary for the event, meeting his future IEEE mentor, Dr. Kiyomi Tomiyasu (to whom Dick is truly grateful for the IEEE tough-love education provided over the course of the next 35 years) (Figure 2). Dick soon started a family and established his company, RS Microwave, Inc., finishing his Ph.D. program at Poly 40 years ago.

Dick’s professional volunteerism started as a student, and he continued being active as he grew in his career. “Active” is kind of an understatement, as Dick was (and still is) involved with the local IEEE Section in North Jersey, acting as IEEE Microwave Theory and Techniques Society (MTT-S)/IEEE Antennas and Propagation Society Chapter chair for about 14 years and IEEE Circuits and Systems Society/IEEE Electron Devices Society Chapter chair for another seven years as well as



Figure 2. Ray Camisa, Kiyomi Tomiyasu, Dick Snyder, and Fred Snyder at IMS2003.



Figure 3. Dick Snyder, Fred Snyder, and a friend (in the middle) at IMS2003.

fulfilling a term as Section chair and then IEEE Metropolitan Sections Activities Council chair. He is a person who loves his profession, IEEE (particularly the MTT-S), and microwave filters. He has been heard to say that he would doubtless pursue all of these things without reward or remuneration. He is completely dedicated to everything he does, committing 110% of his energy with joy and pride in participation and achievement.

His company, RS Microwave, is a successful filter manufacturer, but, although he is president, with various corporate responsibilities, when asked what he does, he says very proudly, "I am a filter engineer." He has been heard to say, "The best job I ever had was as the IEEE Technical Coordinating Committee [now known as the *Future Directions/Technical Coordinating Committee*] chair for four years, in the Administrative Committee." He continues in filter research, with current interests in new topologies and trying to get more performance in less volume—keeping up with the current trends, which seem to be always wanting "more for less."

Conferences are another of Dick's passions, especially his beloved IMS, in which he has participated since the 1960s. He has missed only a few over the

last 50 years or so, at that was only due to military and other commitments. After several unsuccessful proposals, Philadelphia was awarded the hosting of the 2003 IMS, for which he was the general chair (Figure 3), and then he was the emeritus chair of the more recent IMS 2018, also in Philadelphia. Dick works tirelessly in the various Technical Paper Review Committee (TPRC) committees associated with the IMS, European Microwave Week (EuMW), International Microwave and Radar Conference (MIKON), and almost any other large or small microwave conference attracting a global audience.

Dick has provided numerous papers to international conferences, both as an invited speaker or simply with a peer-reviewed submission. He has been on the organizing committees for many non-U.S. conferences and meetings, including the International Wireless Symposium (IWS) in China, COMCAS in Israel, MIKON in Poland, and APMC in several locations. He served as a Distinguished Microwave Lecturer (DML) from 2007 to 2010 (with almost 40 presentations worldwide) and organized filter workshops at the IMS and EuMW, among many other conferences. He has most recently been a cochair of the International Workshop on Microwave Filters (IMFW 2021), held in Perugia, Italy, in November 2021, where he

coauthored the paper that received the first-place Best Paper Award (Figure 4).

Dick has frequently chaired TPRC subcommittees, been a reviewer for many of the MTT-S publications, and served as associate editor of *IEEE Transactions on Microwave Theory and Techniques*. He served as the IMS Executive Committee chair as well as Nominations and Appointments chair. He was the MTT-S president in 2011, and he helped start the very popular IWS in China (together with Ke Wu). For his contributions, Dick has been awarded the IEEE Millennium Award and various best paper awards.

He is the author/coauthor of more than 140 peer-reviewed papers, holds 28 patents, and is a Life Fellow of IEEE. He is a visiting professor at the University of Leeds in the United Kingdom and has been a research professor at the New Jersey Institute of Technology, serving as an advisor/committee member to many Ph.D. degree recipients. He received the Distinguished Service Award from the



Figure 4. Dick Snyder, Simone Bastioli, and Linda Sorrentino receiving the IMFW2021 Best Paper Award.

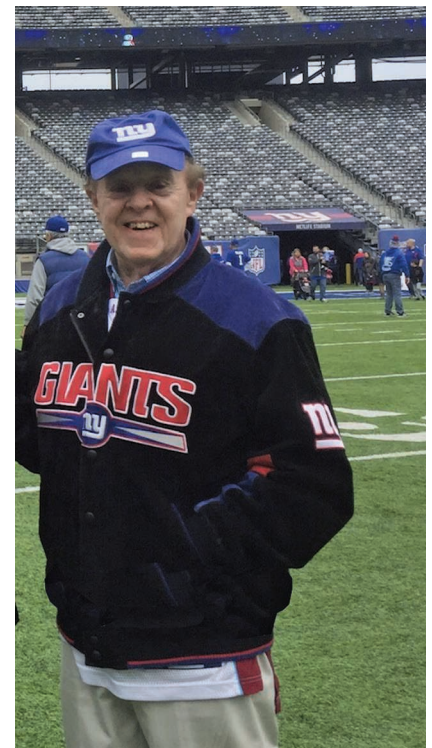


Figure 5. Dick Snyder has supported the New York Giants for as long as he has served the MTT-S.

MTT-S and Microwave Career Award from the European Microwave Association (EuMA), both in 2021. He is also a member of the General Assembly for the EuMA, representing North America. He previously spent five years as the MTT-S representative to the EuMA Board of Directors. His philosophy has always been “Whatever benefits the global microwave community is what we should all support,” and this is something he emphasized during his DML tenure from 2007 to 2010 as well as during and after his term as the Society president in 2011.

Dick is a devoted husband (to his wife, Valerie, of course), father, and all-around family man. He has one brother, a cellist (37 years with the Los Angeles Philharmonic), and is the proud father of three professionally accomplished daughters—one with a Ph.D. degree in computational linguistics (Kieran Snyder); one an attorney (Meredith Little); and the youngest, (Noëlle Santelli-Snyder) a psychotherapist; as well as the grandfather of two grandchildren.

Dick’s interests include attending and watching Yankees baseball and Giants football games (he has taken each of his three daughters to a Giants Super Bowl) (Figure 5), classical and jazz music, the ballet, and golf (but bad knees have reduced his golf to the driving range). He has always thoroughly enjoyed competition of any sort, including roller skating, which he taught in his younger years; baseball (he played in college); golf; and table tennis. He enjoys playing the flute and participates in a band performing for local charity events. In his youth, he was a backup singer for the one-time rock-and-roll hit “Ally-Oop.”

His relaxation is always best enjoyed somewhere near the water (except when it involves fishing golf balls out of a water hazard). He is a former ocean lifeguard and loves swimming daily in his pool at home (in as many months as the New Jersey weather will allow) or racing around on the



Figure 6. Dick Snyder tooling around on the lake.

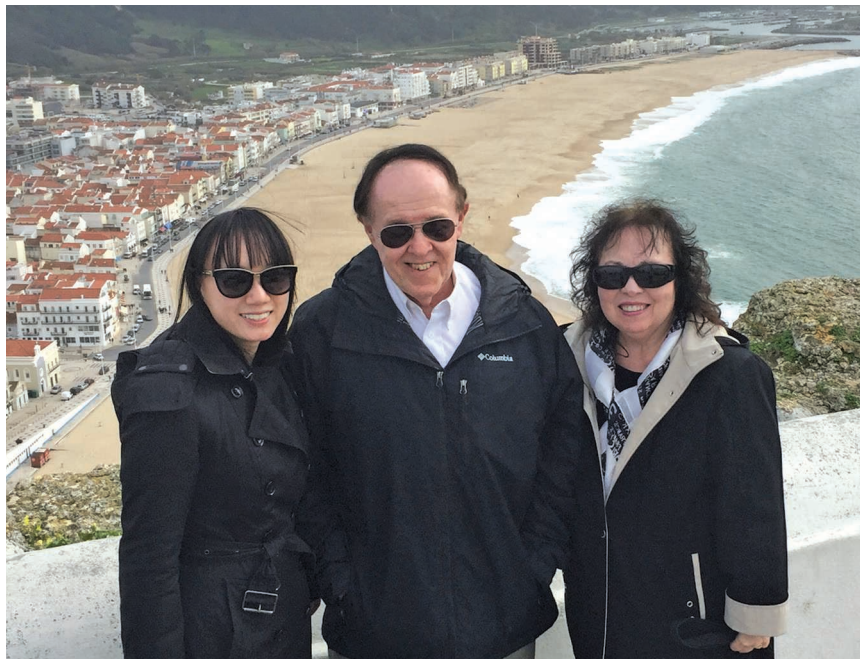


Figure 7. Dick Snyder with Valerie and Noëlle in Portugal, 2017.



local community lake in his 14-ft pontoon boat (Figure 6).

Dick is an adventurous traveler and always loves to have his wife and family with him wherever he goes (Figure 7). Valerie is quite multilingual, and so Dick (who pretty much speaks English only) has no issues communicating thanks to her interpreting abilities. According to Dick, it is a big world with many places yet unseen . . . so far, that is. He also enjoys winemaking

with his father-in-law—and consuming the products, of course.


Dick has been a major contributing force to the MTT-S. His fervent wish is to be part of the continuing successful future of the MTT-S, and he can be counted on for lifelong dedication to the Society. See him reflect on his career at <https://www.youtube.com/watch?v=dA7jA5SreEg>. Congratulations, Dick!





*Alessandra Costanzo,
Francesca Benassi,
and Giuseppina Monti*

Wearable, Energy- Autonomous RF Microwave Systems



In the near future, we will be surrounded in our daily lives by a multitude of small and relatively inexpensive computing devices that are equipped with wireless communication and sensing featuring the concept of “pervasive intelligence,” a basis from which we can envision our future world as an Internet of Things/Internet of Everything (IoT/IoE) in terms of both a consumer IoT/IoE and the Industrial IoT. One of the key desired characteristics of an IoT wireless sensor node is its ability to operate autonomously by means of energy harvesting (EH) rather than relying on bulky batteries, which have a limited lifetime. Furthermore, for many of the aforementioned scenarios, wear-

able solutions are foreseen to further increase the pervasive diffusion of the IoT paradigm, enabling a multitude of devices and individuals to be connected to each other.

The key metrics for the development of successful RF autonomous systems, possibly wearable, are the following:

- *nonintrusiveness*: users must be able to carry out their activities without the limitation caused by the wireless device
- seamless integration with wearable accessories and clothes
- *energy autonomy*: the device must guarantee a long energy autonomy, possibly over its lifetime

Alessandra Costanzo (alessandra.costanzo@unibo.it) and Francesca Benassi (francesca.benassi9@unibo.it) are with Alma Mater Studiorum, the Department of Electrical, Electronic and Information Engineering “Guglielmo Marconi,” University of Bologna, Bologna, 40136, Italy. Giuseppina Monti (giuseppina.monti@unisalento.it) is with the Department of Engineering for Innovation, University of Salento, Lecce, 73100, Italy.

Digital Object Identifier 10.1109/MMM.2021.3130708

Date of current version: 3 February 2022

- *sensing and localization*: the device must be localized and equipped with one or more sensors
- wireless connectivity by means of ultralow-power solutions
- *human-centered design*: fundamental for the success of wearable devices, whose main purpose should be to optimize the user experience.

Nonintrusiveness and seamless integration into wearable accessories and garments require creative manufacturing techniques and unconventional materials, such as flexible ones, to adapt to the soft curves of a human body, or textiles, able to integrate IoT devices into clothing that will be subjected to washing and ironing [1]. Another strategy is to develop devices that can be applied directly to the skin, like patches, or so-called epidermal electronics [2]–[5].

Energy autonomy is certainly a fundamental enabling technology for the IoT paradigm, and it is currently demonstrated by many RF wireless systems, which are based on either fully passive devices or active ones, exploiting “on-demand” wireless power transfer or energy scavenging technologies. For passive wireless systems, an attractive solution is chipless technology, which was originally exploited for RF identification (RFID). Recently, it has been used for sensing and localization purposes, demonstrating a high level of integrability into wearable garments or accessories. Indeed, the absence of chips and electronic components makes this approach particularly suitable for being integrated into garments, using conductive textile materials (threads or fabrics), thereby making possible RF systems that can be washed and ironed. Energy-autonomous devices, based on wireless power transfer or EH, can include chips or electronic circuitry not only for RF-to-dc conversion purposes but also for implementing sensing and localization activities.

This article presents an overview of some recently proposed energy-autonomous wearable devices that exploits both of the approaches described previously, with an emphasis on devices fabricated using textile or flexible materials.

Electromagnetic-Based EH Systems

The first category of RF energy-autonomous systems described in this work is based on electromagnetic EH. It either adopt substrates suitable for RF applications to minimize losses and achieve good performance even in the presence of low received power, or it can be implemented on daily-use materials, such as paper or even clothes [6], with acceptable, although reduced, performance.

The common thread is the circuitry, which can either be an integrated circuit (IC), as in RFID devices,

or a customized implementation, exploiting microstrip technology [7]. There are many application fields in which devices powered by EH can be adopted, as described in the following.

Harmonic Tags

EH exploiting harmonics is an interesting technique that has been applied in RFID sensor-tag applications [8], [9]. These tags are not developed solely for identification purposes; they are also equipped with sensors to perform a more thorough analysis of the environment in which they are located [10]–[12]. The basic operating principles rely on the generation of a backscattered signal at one or more higher harmonics. This principle has been exploited to overcome issues related to RFID systems, which can be vulnerable to clutter noise or self-jamming in the presence of multiple readers [13].

In [14], a paper-based harmonic tag transponder is presented. The antenna is designed as an annular slot antenna tuned to receive an RF signal, transmitted by the reader at a fundamental frequency f_0 of 1.2 GHz and to transmit a signal at $2f_0$ generated by the nonlinearity of the rectifier diodes. A schematic block representation of the system is reported in Figure 1, together with a photo of the prototype.

The antenna is designed with full-wave simulations and demonstrates good matching for both operating frequencies, experiencing a -10 -dBm fractional bandwidth of 22% for f_0 and 12% for $2f_0$, respectively, while maintaining good decoupling. The second harmonic is generated by a Schottky diode HSMS-2850 operating as a frequency doubler and connected to the antenna through a matching network. As the

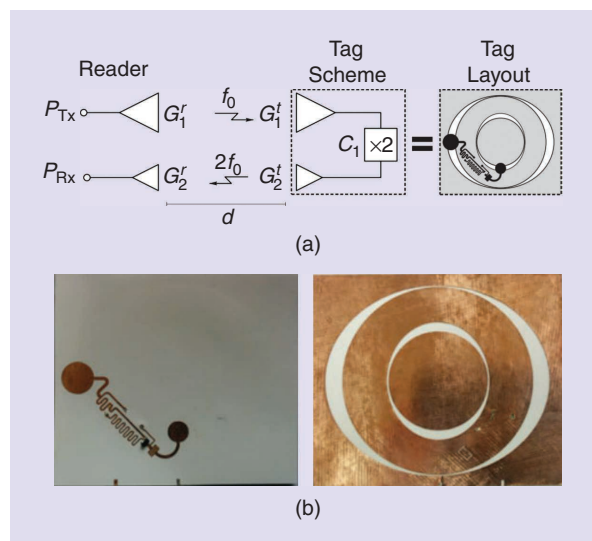


Figure 1. (a) A schematic description of the harmonic tag. (b) Photos of the front and back of the prototype [14].

circuit schematic in Figure 1(b) shows, at the input, two meandered quarter-wave stubs are used as a harmonic filter, allowing only the fundamental frequency to flow into the diode. At the output, a high-pass filter is optimized, with the twofold goal of providing the complex conjugate condition at -13 dBm of input power, thus maximizing the power flow to the transmitting antenna, and a short at f_0 . The experimental validation used a reader equipped with a circularly polarized antenna to avoid degradation due to tag-reader misalignment. Figure 2 shows the received power at $2f_0$ as a function of the distance between the reader and the tag [14] for a transmitted power of 11 dBm. The maximum reading range is found to be approximately 4 m, showing good agreement with the expected performance. Compactness, flexible materials, and energy autonomy make this system suitable for modern IoT scenarios, fulfilling some of the most

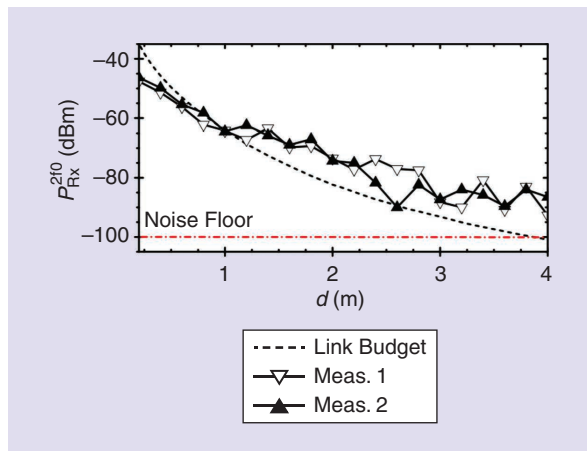


Figure 2. The measured and simulated received power for the harmonic tag in [14] at 11 dBm of transmitted power; labels “meas. 1” and “meas. 2” refer to the tag aligned with the horizontal and vertical polarization of the antenna, respectively.

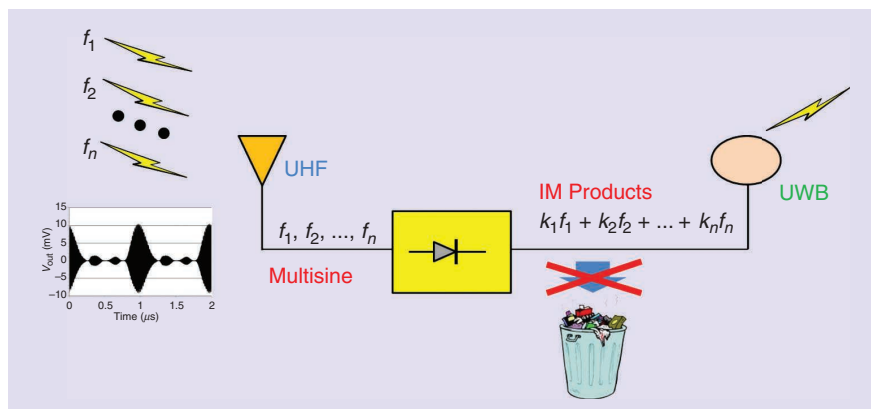


Figure 3. The concept for a passive, batteryless UWB-pulse generator tag. IM: intermodulation.

important requirements, such as energy autonomy, miniaturization, and lightness.

EH Systems for Localization

Indoor positioning systems are considered a developing technology, and the methods adopted for its realization are several and different; out of these, the use of ultrawideband (UWB) (possibly backscattered) signals [15] is promising for its exploitation of a very large range of frequencies, allowing it to avoid the possible effects of fading and shadowing that are likely in indoor environments at certain frequencies. At the same time, these approaches need reference nodes for safe implementation of the signal processing technique to obtain centimeter-level localization. Batteryless UWB tags with onboard, ultralow-power, UWB pulse generator chips have recently been demonstrated for localizing objects in space [16], but a similar performance can be reached with the chipless solution presented in [17], where multisine excitation at ultrahigh frequency (UHF), normally adopted only for increasing the rectifier RF-to-dc efficiency [18], is exploited for two different goals: 1) EH, by converting energy from RF to dc, and 2) passive generation of a quasi-UWB impulse by backscattering the intermodulation products of the same multisine excitation, which are normally filtered out and wasted. Figure 3 depicts the passive, batteryless UWB tag concept [17].

Figure 4 shows the circuit schematic of the UWB tag. It consists of a standard rectenna designed for EH purposed at UHF (centered at 871.5 MHz), with a frequency-multiplexing output section consisting of a dc path and a UWB path, which is connected to a UWB antenna radiating a quasi-UWB pulse (in the lower-UWB European bandwidth: 2–6 GHz) composed of the intermodulation (IM) products generated by the rectifier nonlinearities.

The batteryless tag is interposed between a multisine UHF transmitter (Tx) and a set of UWB receivers (Rx), acting as anchor nodes. Tag localization

is performed by processing the time difference of arrival among the UWB signals received by the anchor nodes backscattered by the tag. Typically, when the tag is close to the anchor nodes (i.e., within 1 m), all the third-, fourth-, and fifth-IM harmonics of the backscattered multisine can be used by the signal processing algorithm. Indeed, as depicted in Figure 5, where the power spectrum at the tag UWB output for a four-tone

UHF excitation is reported, a rich number of spectral lines exceeding -90 dBm is obtained.

In contrast, when the tag is farther away (i.e., 4 m), the fifth harmonic is discarded because it is too corrupted by noise. Increasing the spacing of the tones (i.e., the multisine excitation bandwidth) improves the localization accuracy: for example, if eight tones and a tone spacing of 500 kHz are used, high accuracy (error below 20 cm) can be reached up to a tag-Rx distance of 8 m for an observation time of $T_{\text{obs}} = 200$ ms, and up to 12 m for $T_{\text{obs}} = 500$ ms; while if a larger tone spacing (2 MHz) is allowed, high accuracy is obtained up to 12 and 16 m, respectively. The predicted root-mean-square error for increasing the tag-Rx distances is shown in Figure 6.

One important aspect of the design approach used in [17] is the representation of the multisine as a periodic excitation instead of a quasi-periodic one, with each tone corresponding to a higher harmonic of the same fundamental frequency, that is, the tones' spacing. With this approach, the nonlinear analysis is carried out as a single-tone analysis with a very large number of harmonics instead of a multitone one, thus allowing a large number of tones to be accounted for with a much faster simulation: the computational time comparison is reported in the table of Figure 7, where the multisine waveforms resulting from a periodic and quasi-periodic representation are compared.

It is clear that, in multisine excitations, tone spacing is a crucial design parameter for improving localization: the higher the tone spacing, the better the localization accuracy. Simulations have then led to optimizations aimed at quantifying the number of tones and the frequency spacing Δf to be used to obtain the highest harmonic content.

As can be seen from the plots in Figure 8, where the spectra contents are plotted for each harmonic window, for the same average input power, an increase in the harmonic content is achieved with increasing frequency spacing Δf .

Passive Sensing by Exploiting Wearable RF EH

Another field in which EH techniques are receiving more interest is wearables for biomedical applications. Advanced technology in the biomedical sector has led to the realization of an enormous number of wearable sensors for real-time monitoring [19] and identification of patients both inside the hospital environment [20]

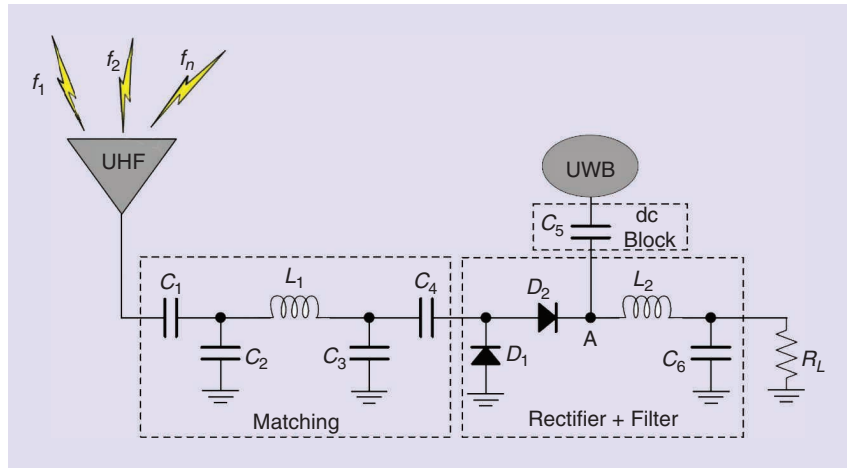


Figure 4. A circuit schematic of the passive, UWB-pulse generator tag in [17].

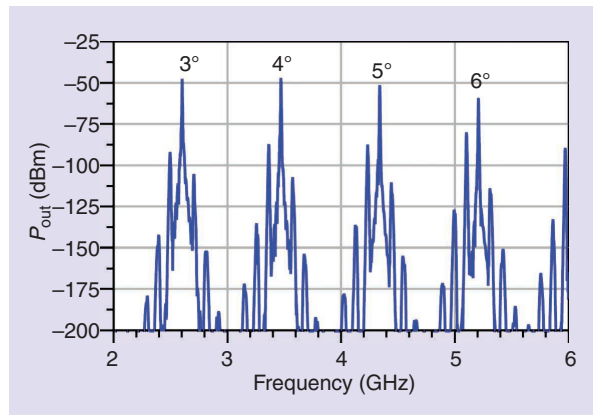


Figure 5. The power spectrum of the UWB-pulse generator tag resulting from the intermodulation of a four-tone UHF excitation with an average input power of -10 dBm [17].

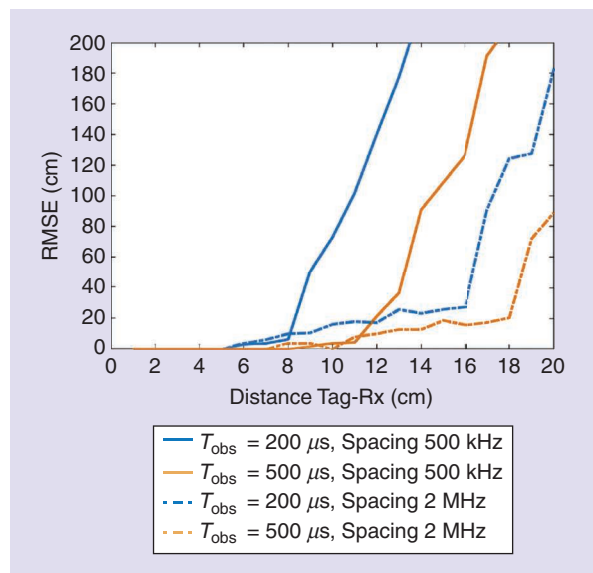


Figure 6. The RMSE tag localization for varying multisine spacings of 100 kHz and 2 MHz, respectively, for an eight-tone excitation.

Regime	Number Tones	IMD Order	Number Spectral Lines	CPU Time (s)
Quasi-Periodic	4	6	644	36
Quasi-Periodic	8	4	19,912	74,280
Periodic	4	–	6,000	35
Periodic	8	–	6,000	42
Periodic	16	–	6,000	55

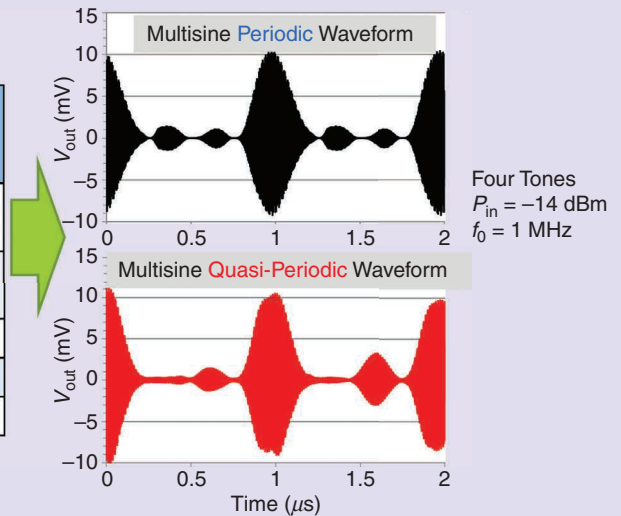


Figure 7. A comparison between multisine waveforms resulting from a periodic and a quasi-periodic representation of the UHF excitation; the corresponding computational times are also reported [17]. IMD: intermodulation distortion.

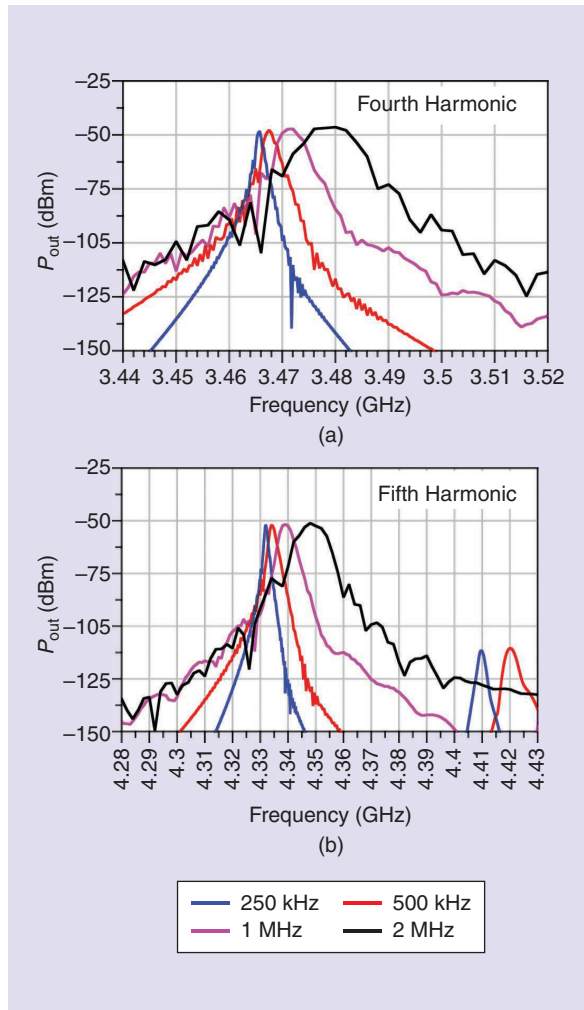


Figure 8. Power spectra of the fourth- and fifth-harmonic windows for the UHF signal versus frequency spacing [17].

and remotely. In [21], a low-power, passive tag performing pervasive monitoring of patient’s vital parameters, such as a phonocardiogram (PCG), is implemented and wirelessly powered. A schematic of the whole system is displayed in Figure 9(a), while the chip details are given in Figure 9(b). The system is able to read multiple-sensor information and generate an alarm when a parameter exceeds set limits.

The system is powered by an external Tx operating at 900 MHz and transferring 4 W of equivalent isotropic radiated power (EIRP). The available power is estimated for increasing distances of the tag from the transmitting antenna, showing that the operating range is limited to 12 m. The experimental validation shows 15 μ W of output power for an operating distance of 1.3 m from the Tx antenna transmitting 800 mW of EIRP. A small microphone for the PCG is used as the primary actuator, and the 15 μ W of received power is sufficient to run both the chip and the microphone at a bias current of 30 μ A. The data are sent from the tag to the base station through backscatter modulation, allowing the tag to operate in low-power conditions, making it suitable for wireless power.

EH can also be exploited to detect the presence of specific fluids or materials. In [22], an energy-autonomous filtering antenna operating at 2.45 GHz is used to perform wireless detection of ethanol solutions on a hand surface for checking hand-sanitizing procedures.

The system is designed on a Rogers substrate RT/Duroid 5880, whose flexibility and thickness make it suitable for wearable applications, as shown in Figure 10. The sensing area consists of a microstrip open stub embedding a microfluidic channel at its open end;

the stub is tuned to resonate at a 2.45-GHz operating frequency when a given target ethanol solution is filling the channel. When any other fluid is present, the stub is detuned. To enhance frequency selectivity, the stub is placed in place of one open end of a two-section coupled line filter, enabling the system to act as a selective detector only in the presence of that specific ethanol solution made up of 70% ethanol and 30% water. This concentration was chosen because it is one of the most prevalent compositions of common hand sanitizers.

The power received by the patch antenna starts the detection process because it is transferred to the rectifier input depending on the fluid filling the loaded filter. In this way, the obtainable dc-output voltages vary significantly and can be used as the read-out quantities of the detection process. Figure 11 shows the predicted and measured output dc voltages of the rectifier as a function of the received RF power for different fluids (70% ethanol, water, and air) filling the filter channel. From these plots it is clear that for a given RF input power, the dc output voltage allows it to detect the target solution. The detector can be worn as a bracelet and is wirelessly activated by an external 2.45-GHz RF source, avoiding the need for batteries.

For the sake of completeness, performances of the detector for different water-ethanol concentrations were computed for a received power of 0 dBm. These performances are reported in Figure 12, where quite distinguishable dc-output voltages are obtained for different concentrations.

Chipless RFID

Chipless RFID is an attractive technological solution for developing passive sensors and devices, which can be seamlessly integrated into wearable accessories and clothes. Chipless sensors provide various advantages, such as almost-infinite service life, low cost, low environmental impact, and robust performance in harsh scenarios, where ICs could be damaged [23]–[26].

The general architecture and working mechanism of a chipless RFID are the same as for all RFID systems,

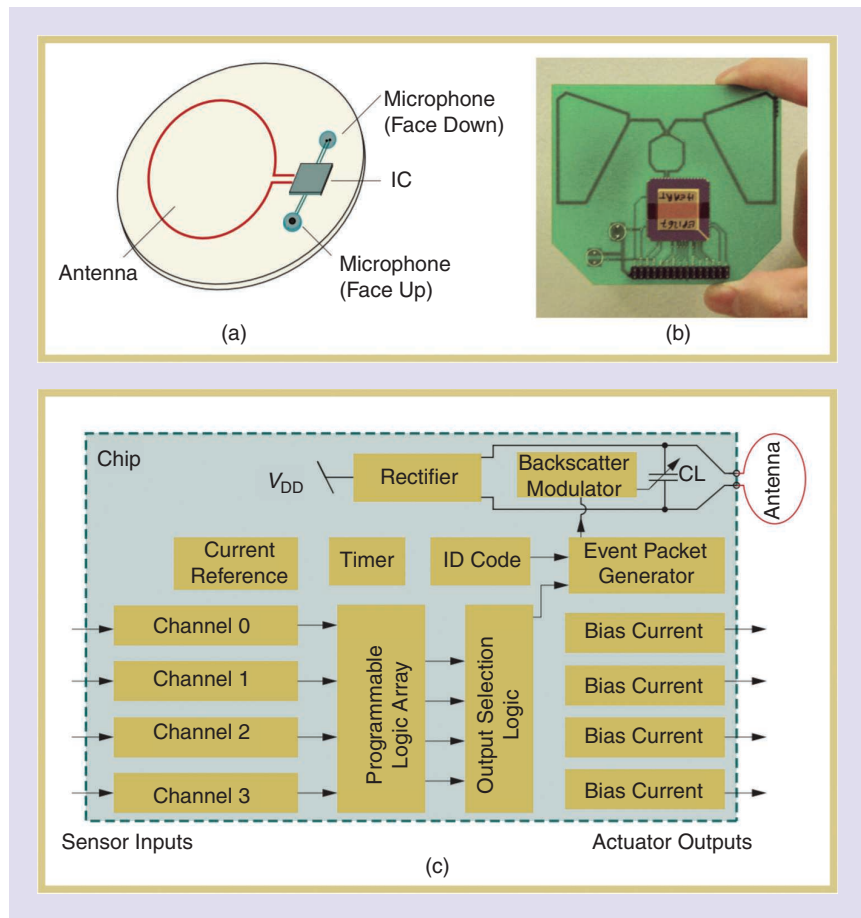


Figure 9. (a) A pictorial representation of a low-power, passive tag performing pervasive monitoring of patient's vital parameters and (b) a block diagram of the embedded chip [21]. CL: chip's input capacitance.

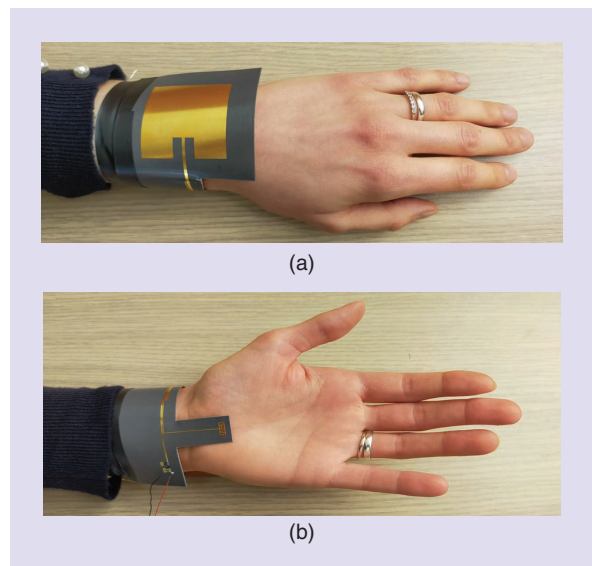


Figure 10. A wearable, energy-autonomous fluid detector. (a) A patch antenna for EH and (b) a microstrip bandpass filter, loaded with a stub-microfluidic channel and connected to the rectifier circuitry [22].

with a reader wirelessly connected to one or more tags and acting as the interrogator and data collector. The reader transmits an RF signal and receives back the sensed data in the form of a signal scattered by the tag [27]–[29].

However, with respect to chipped tags, the decoding of the identifier (or of the sensed data) is different as there is no communication protocol. The tag is passive; it does not contain any electronic component or chip and does not embed any power recovery system or transceiver. The decoding of the data is accomplished exclusively from the analysis of the signal (phase and amplitude) scattered by the tag.

Different encoding techniques have been proposed in the literature for chipless RFID. Depending on the domain adopted (frequency or time) for the analysis of the scattered signal, two main categories can be identified: time-domain reflectometry (TDR)-based tags and spectral signature-based tags [29].

TDR-based systems [30] are mostly based on surface acoustic wave technology and exploit an electroacoustic

transducer connected to an antenna as the tag; they encode the information in the time domain. Spectral signature-based systems are mostly based on resonant structures, and the sensed data are encoded by the presence/absence of resonance peaks in the signal scattered by the tag in such a way that the information is encoded in the frequency domain.

Figure 13 presents two possible system architectures:

- 1) Retransmission based, where both the tag and the reader are equipped with two cross-polarized antennas. The signal received by one of the antennas is encoded inside the tag and retransmitted by the cross-polarized one.
- 2) Backscatter based, where the tag acts as a reflective, frequency-selective surface, and the reader decodes the information by analyzing the scattered signal.

In both architectures, a UWB signal is used for interrogation. Wearable chipless tags have been proposed in [31]–[37] using textiles, and in [38] and [39] using flexible materials.

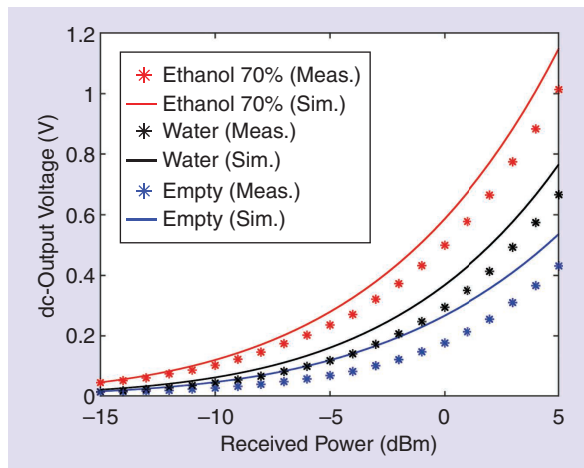


Figure 11. The dc-output voltage versus received power in the presence of different fluids filling the channel [22]. Meas.: Measured; Sim.: Simulated.

Ethanol Concentration (%)	ϵ_r	σ	dc-Output Voltage
30	60	2.45	0.42 V
40	52	2.45	0.463 V
50	44	2.45	0.508 V
60	33.5	2.18	0.585 V
70	30	2.18	0.586 V
80	22.8	1.91	0.608 V
90	16	1.63	0.571 V

Figure 12. The dc-output voltage rectified by the system [22] for different water-ethanol solutions for a 0-dBm impinging power.

Textile Chipless Tags Using Conductive Fabrics

In [34], two textile chipless tags used as touch sensors are presented. The two tags are fabricated using a layer of fleece as a substrate (a thickness equal to 0.5 mm, and a relative dielectric permittivity equal to 1.18) and

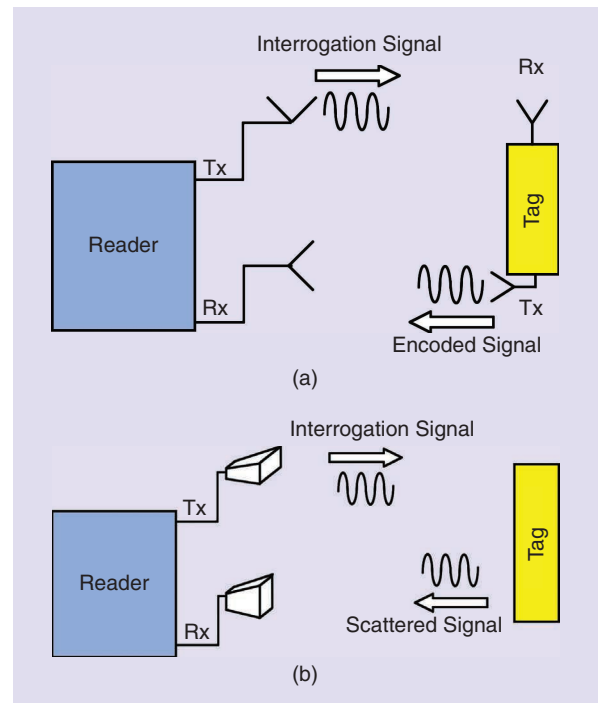


Figure 13. The possible architectures of a chipless RFID system. (a) The reader and the tag are equipped with two cross-polarized antennas. (b) The tag consists of a reflective frequency-selective surface.

an adhesive, nonwoven conductive fabric (NWCF) for all the conductive parts. A cutting plotter is used to shape the NWCF.

NWCF is an excellent material for the fabrication of textile devices. It has an electrical conductivity equal to 2.27×10^5 S/m and a thickness equivalent to 0.11 mm. Additionally, this fabric has good performance in terms of robustness with respect to washing and ironing and can be shaped by hand or by using a cutting

plotter [1], [40]–[42]. The geometry and photos of the tags are given in Figure 14. The tag shown in Figure 14(a) is a 2-bit, multiresonator chipless tag consisting of a microstrip line with two resonators slotted on the ground plane. The number of bits available for encoding is determined by the number of resonators (for the analyzed tag it is equal to two). The resonators on the ground plane introduce a zero in the transmission coefficient of the microstrip line (i.e., a minimum in the

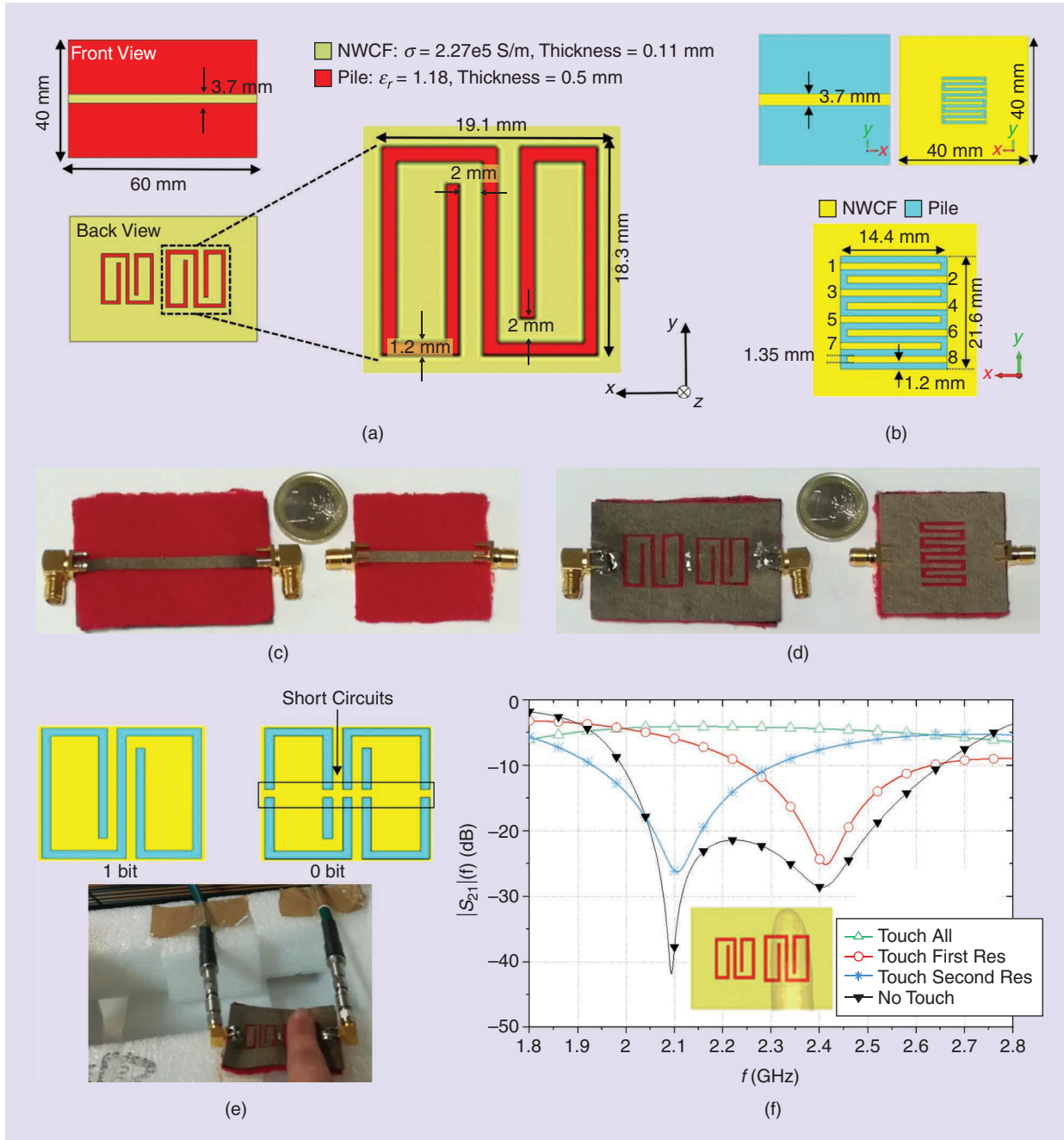


Figure 14. (a) and (b) A layout of the chipless tags presented in [34]. (c) and (d) The front- and back-view photos of the fabricated prototypes. (e) A touch-type deactivation of the resonators of the tag in (a) and the corresponding logic state. (f) The transmission coefficients' behavior when using the tag in (a) as a touch sensor. Res: resonator.

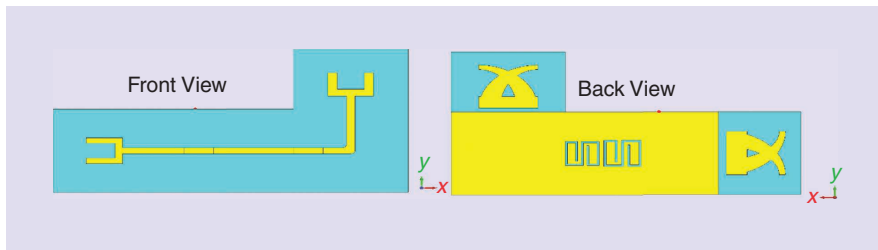


Figure 15. A wearable antenna for implementing the wireless connection with the reader for the tag illustrated in Figure 14. The front and back views of the tag assembly, consisting of the microstrip line loaded by the resonator, illustrated in Figure 14(c) and (d), connected to two cross-polarized antennas [31].

amplitude of the microstrip line-scattering parameter S_{21}). The resonant frequency of each resonator can be selected by fixing the geometrical dimensions in such a way that each zero of the microstrip transmission coefficient can be associated with the specific resonator.

Furthermore, a resonator can be “deactivated” by short-circuiting with a finger, as illustrated in Figure 14(e). In this way, each resonator can be used as a coding bit with two possible logic states: “0” and “1.” For a tag using n resonators, when all the resonators are active, the microstrip line will have n transmission zeroes (all bits are in the logic state of “1”). By short-circuiting one resonator, the associated transmission zero disappears

and the corresponding bit turns into a “0” logic state [see Figure 14(e) and (f)]. In this way, the tag can be exploited as a touch sensor and used, for example, as a wearable keyboard: when a finger touches one resonator, it deactivates it and modifies its logical state from “1” to “0” [see the photo in Figure 14(e) and (f)].

Figure 15(b) shows the layout of the antennas used

to establish the wireless connection of the tag with the reader. The antennas consist of two identical, microstrip-fed monopoles located on the ground-plane side and arranged in such a way that they are cross polarized [31], [42].

As depicted in Figure 14(b), the tag implements the frequency-shift-coding technique. It includes a microstrip line with a hairpin resonator slotted on its ground plane. The hairpin resonator, which loads the microstrip line, introduces a zero-transmission coefficient at a prescribed frequency. When some fingers are touched (see Figure 16), they are short-circuited and the zero-transmission coefficient undergoes a frequency shift. In this way, the position of the finger on the resonator can be retrieved. This behavior is illustrated in Figure 16.

In [35], a chipless tag for gesture-recognition applications is presented. Like the tags in Figure 14, the materials adopted for fabrication are fleece as dielectric substrates (a layer with a thickness of 1 mm was used) and NWCF for the conductive parts.

A photo of the tag embedded in a glove is shown in Figure 17(a). The tag consists of a stub-loaded microstrip line. The stubs are open-ended, quarter-wave resonators with different lengths and are separated from the microstrip line by a small gap.

When the tag is stretched out, the stubs are not electrically connected to the microstrip line, and there are no zeroes in the transmission coefficient. By bending one of the stubs in such a way that the corresponding stub-line gap is short-circuited, an electrical contact is established between the microstrip line and the stub. At the resonant frequency for which the stub length is equal to $\lambda/4$, the stub behaves as an impedance inverter, transforming its open-circuit load into a short circuit load for the microstrip line, thus leading to the presence of a transmission zero. In this way, the glove embedding the proposed tag can be exploited as a gesture-recognition sensor: the bending of a specific finger can be recognized by the presence/absence of the transmission zero corresponding to that finger.

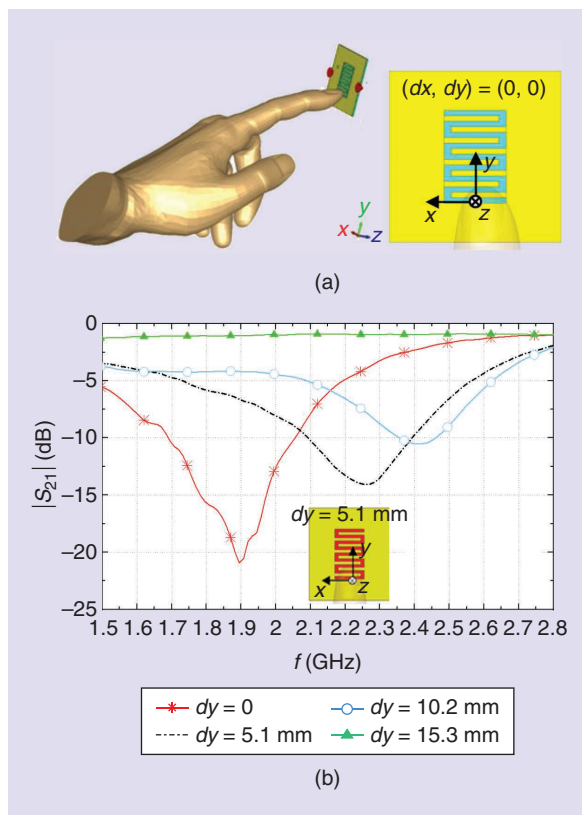


Figure 16. A touch-sensor response in terms of the microstrip line-transmission coefficient of the tag illustrated in Figure 14.

The results obtained for a three-finger prototype are reported and discussed in [35], with a photo presented in Figure 17(b). In this prototype, the electric contact due to the bending of the fingers is optimized by the presence on the microstrip line of a small fleece cylinder coated with conductive fabric at the stub positions. For this device, the stubs have been dimensioned to resonate in the [2.7-, 3.6-] GHz frequency band. The transmission coefficients of the gesture sensor for different positions of the fingers are illustrated in Figure 17(c) for bending of single and multiple fingers.

Two planar monopoles, integrated with the tag for wireless communication with the reader, have been conceived in [35] and are shown in Figure 18(a). For this device, the stubs have been dimensioned to resonate in the [3.4-, 4.6-] GHz frequency band.

According to the retransmission architecture of chipless tags, to exploit the device for gesture recognition, a reader with two cross-polarized antennas must be used. In [35], the details of the reader architecture

According to the retransmission architecture of chipless tags, to exploit the device for gesture recognition, a reader with two cross-polarized antennas must be used.

(both hardware and processing software) are not shown, but preliminary communication tests are presented. More specifically, experimental tests were performed by integrating one antenna into the tag as the receiving antenna [see Figure 18(a)] and using the other one as the transmitting antenna (i.e., as the reader transmitting antenna). The achieved results are reported in Figure 18(b) and refer to a distance between the two antennas of 60 cm. According to these results, a reading distance on the order of a few meters or better is expected with a suitable design of the reader. In fact, due to the lack of size constraints, in the final device, high-gain antennas can be used

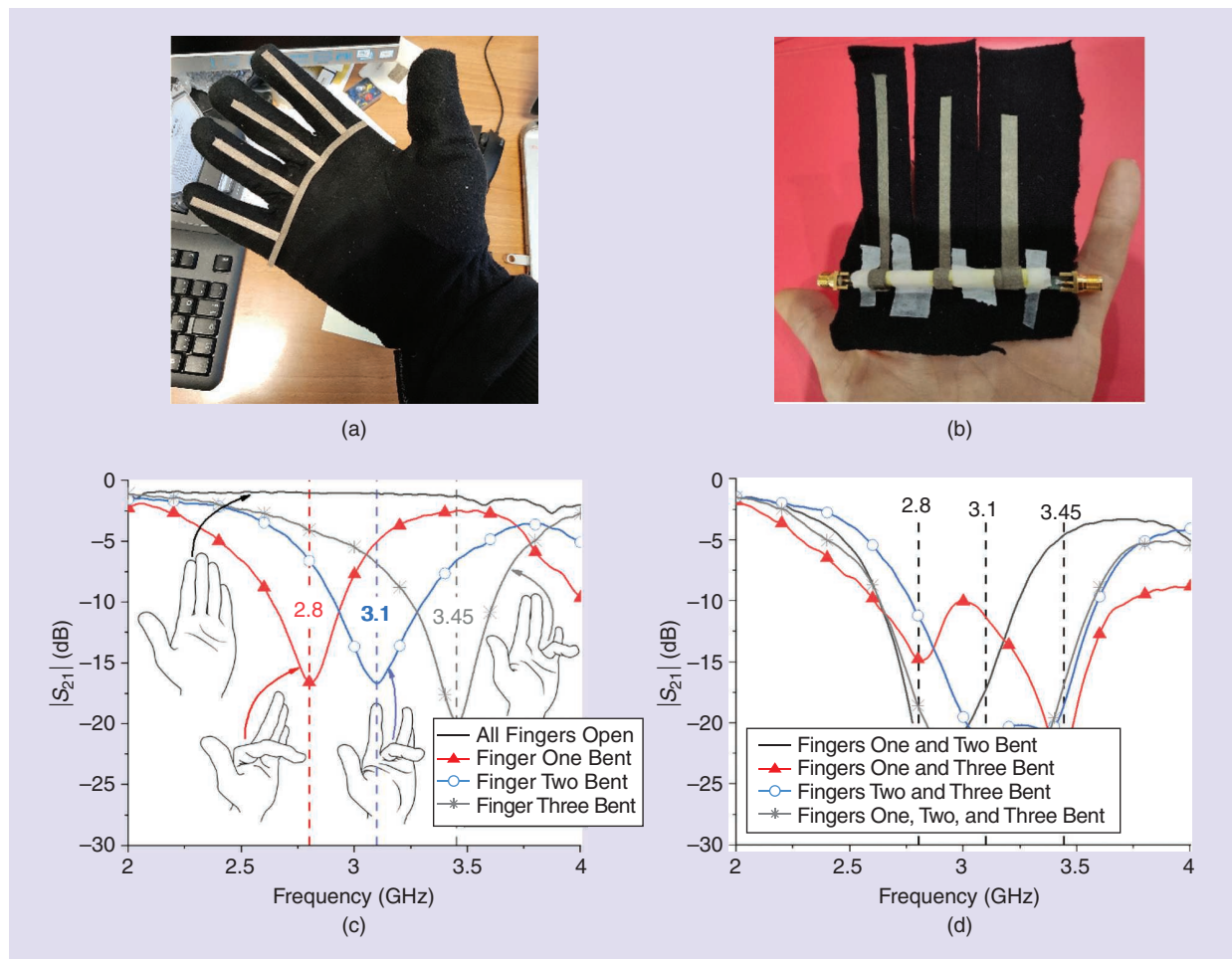


Figure 17. (a) Integration of the tag presented in [35] into a glove. (b) The three-finger prototype analyzed in the article. (c) The experimental results referring to a three-finger prototype [35].

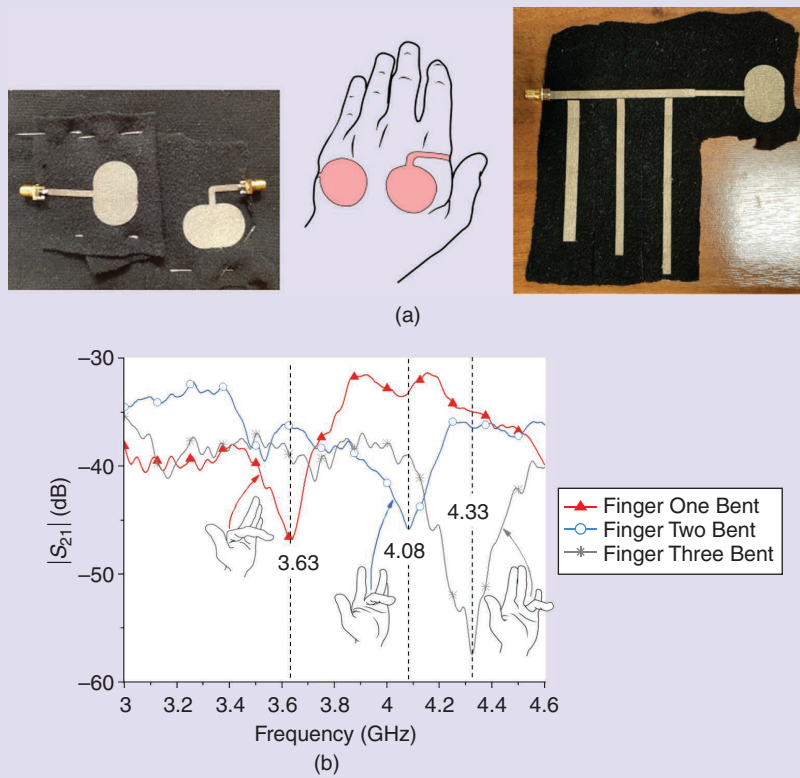


Figure 18. (a) An antenna-tag connection for wireless communication between the tag and the reader. (b) A measured transmission coefficient of the reader-to-tag link using the antennas in Figure 17: one at the tag and the other at the Tx side (the data refer to a link of 60 cm) [35].

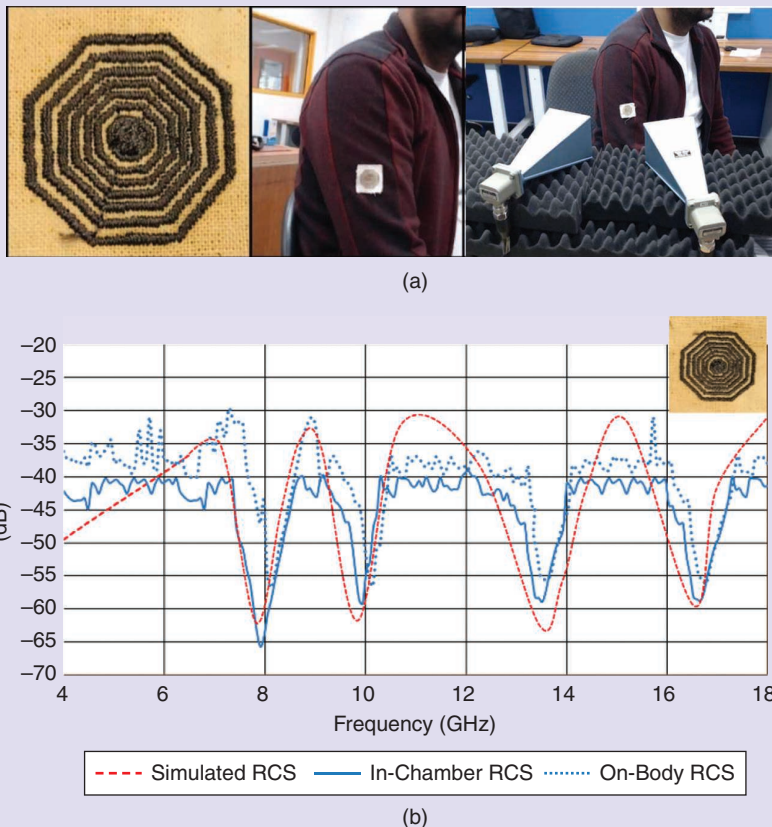


Figure 19. The embroidered tag presented in [36] and the simulated and measured radar cross section (RCS) [36].

for the reader side. Additionally, the reading distance can be improved via customized postprocessing of the received signal.

Embroidered, Fully Textile Tags

Another approach to the fabrication of wearable devices that are highly integrated into garments is to embroider the device on common textile materials (cotton, fleece, or denim) using conductive thread. Two chipless tags based on this approach are presented in [36] and [37], respectively.

In [36], an embroidered tag fabricated using a silver-coated, polyamide conductive fiber (HC12) on a cotton substrate with a commercial embroidery system is presented. The tag exploits a frequency-selective surface consisting of concentric, octagonal aperiodic loops (see Figure 19). A 4-bit tag is obtained using six concentric, octagonal loop resonators. The encoded data bits are obtained by radar cross-section (RCS) measurements.

The experimental data collected from placing the tag at a distance of approximately 1 cm from the human body are reported and analyzed (see Figure 19) and demonstrate a reading range of 180 cm.

In [37], an electrothread plated with silver is used to embroider three scatterers on a cotton textile. The presence of a zero in the tag RCS is related to the presence of a specific resonator. The proposed approach is demonstrated for a three-scatterer device corresponding to a 3-bit tag. The measured data, reported in Figure 20, were obtained in an unshielded environment using a horn antenna as the reader and by placing the tag at a distance of 20 cm from the horn aperture.

Tags on a Flexible Support

Another approach suitable for devices applicable to the human body and adaptable to its soft curves makes use of flexible materials as the substrate, such as the chipless tag for gesture recognition presented in [38], which uses

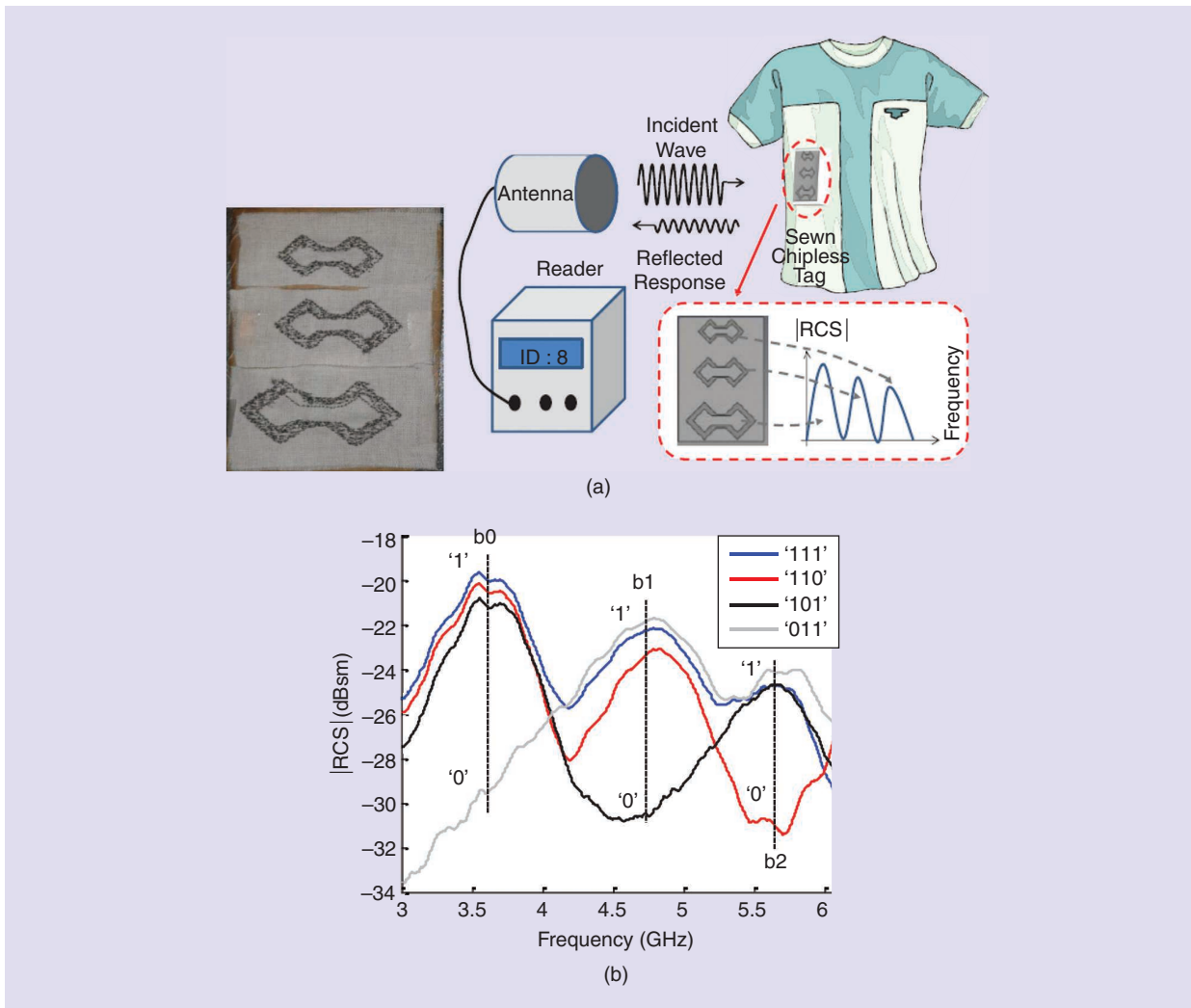


Figure 20. An embroidered tag with scatters and RCS measurements [37].

Silo-ECA has higher conductivity ($1.51 \times 10^6 \text{ S/m}^{-1}$) than other stretchable conductors, and it remains nearly unchanged after being subjected to 500 cycles of 100% applied strain.

resonators whose resonance frequency is a function of the induced strain. A stretchable, silicone-based electrically conductive adhesive (silo-ECA) and a silicone elastomer are used for the metallization and the substrate, respectively. Silo-ECA has higher conductivity ($1.51 \times 10^6 \text{ S/m}^{-1}$) than other stretchable conductors, and it remains nearly unchanged after being subjected to 500 cycles of 100% applied strain. The fabrication of high-definition devices is possible by exploiting stencil-printing techniques as well as soft lithography.

In this way, a flexible and very thin device is obtained, which can be attached to the hand, thus acting as “smart skin.” The encoding of different gestures is illustrated in Figure 21(a); the fabricated prototype and a schematic representation of the device applied on the hand are given in Figure 21(b) and (c), respectively. Figure 21(d) shows the measured transmission coefficients obtained for two different gestures. The blue and red lines correspond to all fingers up and to the pinky bent,

respectively: bending of the pinky leads to a shift of 136 MHz of the resonant frequency of the corresponding resonator. However, a shift up to 70 MHz is also observed for higher-resonant frequencies. As seen in [38], this behavior is probably due to the copper sheet at the bottom of the silicone substrate and could be solved (or at least alleviated) by replacing this layer with ECA to make the tag more flexible.

A millimeter-wave (mm-wave) chipless sensing sticker is presented in [39] and is based on a Van-Atta reflectarray. A high-performance reading system based on polarimetric interrogation and a time-frequency data processing scheme are implemented for the reading of this tag. The system operates in the Ka-band (i.e., a frequency range from 26.5 to 40 GHz) and provides a reading range of 30 m.

A photo of the front face of the fabricated tag is shown in Figure 22(a), it is inkjet printed using silver nanoparticle ink on a low-cost Kapton HN polyimide substrate (a thickness of 0.127 mm), while the ground plane consists of copper tape attached to the back. The advantages of a Kapton substrate are low cost and the possibility of fabricating high-precision circuits and antennas by means of inkjet printing. From experimental tests, in the gigahertz frequency band [25], [39], the relative electric permittivity of the adopted substrate is in the range of [3, 3.1]. The setup adopted for measurements is presented in Figure 22(c), while the spectrogram measured for a distance of 30.5 m is shown in Figure 22(d).

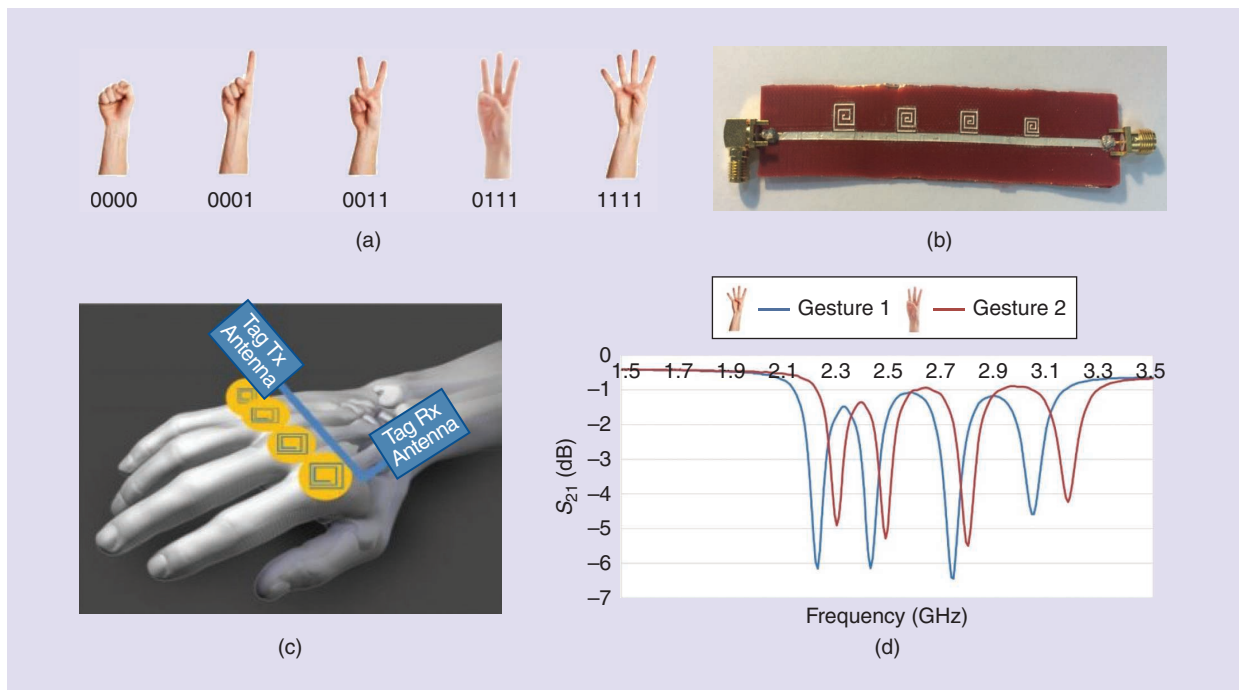


Figure 21. The gesture sensor on stretchable materials. (a) The encoding of different gestures. (b) A photo of the fabricated tag. (c) A rendering of the tag application to the hand. (d) The measured transmission coefficient obtained for two different gestures [38].

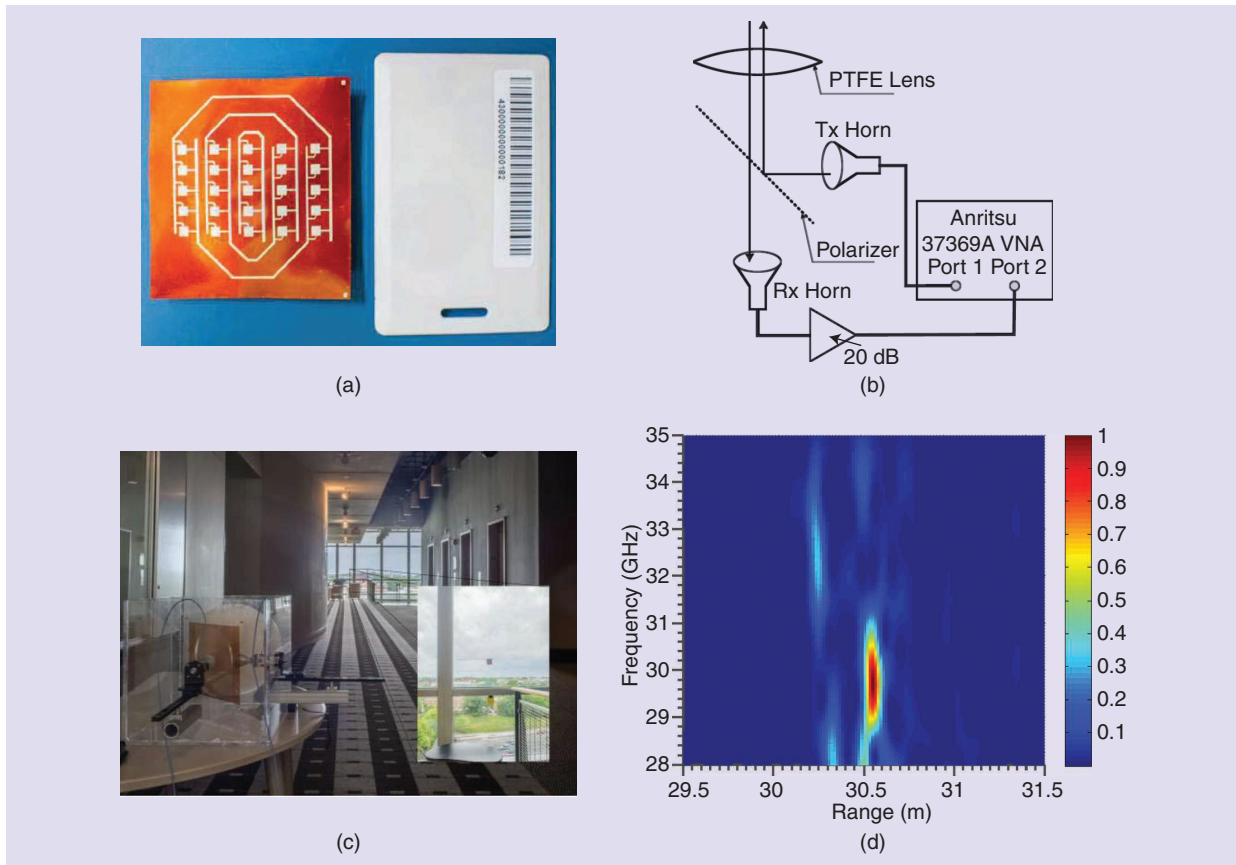


Figure 22. A flexible mm-wave Van-Atta reflectarray. (a) A photo of the prototype. (b) A schematic representation of the reading system based on polarimetric interrogation. (c) The measurements setup. (d) A measured spectrogram with a reader-tag distance of 30.5 m [39]. PTFE: polytetrafluoroethylene.

Conclusions

This article discussed selected microwave and mm-wave systems, augmented with sensing capabilities and designed on unconventional materials to allow for their use in wearable applications and/or in smart objects of complex shapes. They all share energy autonomy and battery operation. The considered approaches to reach energy autonomy can be divided into two categories: 1) EH-based systems, which include an RF-dc converter to provide the power for self-sustainable operation of the embedded chips and 2) chipless systems, whose operations do not rely on active chips but on the selective frequency responses of passive RF circuits, thus being fully embeddable in garments using textile materials.

These unconventional RF systems are suitable for enabling many IoT use cases, such as monitoring/control systems in smart homes, transportation, health care, emergency detection/response, soil monitoring, and precision agriculture. Indeed, energy autonomy can avoid the use of batteries with the twofold advantage of avoiding tag maintenance as well as the environmental impact of battery disposal. There are still many issues to be overcome for these solutions to be widely exploited, both on the tag side

and on the reader/energy-supplier side. On the tag side, the most challenging issues are increasing the reliability of manufacturing processes of materials not designed for high-performance RF applications, and the minimization of energy usage for secure activity and remote accessibility. On the energy-supplier side, smart solutions are still being sought to perform not only beamed energy transfer but also ranging, with the dual objective of guaranteeing sufficient energy supply and, at the same time, energy saving where there are no tags to be interrogated.

References

- [1] L. Corchia, G. Monti, and L. Tarricone, "Wearable antennas: Non-textile solutions versus fully-textile solutions," *IEEE Antennas Propag. Mag.*, vol. 61, no. 2, pp. 71–83, 2019, doi: 10.1109/MAP.2019.2895665.
- [2] M. Meyer, N. Van Binh, V. Calero, L. Baraban, G. Cuniberti, and J. A. Rogers, "Imperceptible sensorics for medical monitoring," in *Proc. IEEE 15th Int. Conf. Nanotechnol. (IEEE-NANO)*, 2015, pp. 1309–1312, doi: 10.1109/NANO.2015.7388873.
- [3] E. M. Amin, J. K. Saha, and N. C. Karmakar, "Smart sensing materials for low-cost chipless RFID sensor," *IEEE Sensors J.*, vol. 14, no. 7, pp. 2198–2207, Jul. 2014, doi: 10.1109/JSEN.2014.2318056.
- [4] C. Occhiuzzi, S. Parrella, F. Camera, S. Nappi, and G. Marrocco, "RFID-based dual-chip epidermal sensing platform for human skin monitoring," *IEEE Sensors J.*, vol. 21, no. 4, pp. 5359–5367, 15 Feb. 2021, doi: 10.1109/JSEN.2020.3031664.

- [5] C.-W. Chang, P. Riehl, and J. Lin, "Wireless charging for smart garment with textile-based receiver coils," in *Proc. IEEE Wireless Power Transf. Conf. (WPTC)*, 2020, pp. 484–487, doi: 10.1109/WPTC48563.2020.9295550.
- [6] J. Antonio Estrada *et al.*, "RF-harvesting tightly coupled rectenna array tee-shirt with greater than octave bandwidth," *IEEE Trans. Microw. Theory Techn.*, vol. 68, no. 9, pp. 3908–3919, Sep. 2020, doi: 10.1109/TMTT.2020.2988688.
- [7] V. Palazzi, M. Del Prete, and M. Fantuzzi, "Scavenging for energy: A rectenna design for wireless energy harvesting in UHF mobile telephony bands," *IEEE Microw. Mag.*, vol. 18, no. 1, pp. 91–99, Jan./Feb. 2017, doi: 10.1109/MMM.2016.2616189.
- [8] P. Mezzanotte, V. Palazzi, F. Alimenti, and L. Roselli, "Innovative RFID sensors for Internet of Things applications," *IEEE J. Microw.*, vol. 1, no. 1, pp. 55–65, 2021, doi: 10.1109/JMW.2020.3035020.
- [9] D. Allane, G. Andia Vera, Y. Duroc, R. Touhami, and S. Tedjini, "Harmonic power harvesting system for passive RFID sensor tags," *IEEE Trans. Microw. Theory Techn.*, vol. 64, no. 7, pp. 2347–2356, Jul. 2016, doi: 10.1109/TMTT.2016.2574990.
- [10] H. Solar, A. Beriain, I. Zalvide, E. D'Entremont, and R. Berenguer, "A robust, -40° to $+150^{\circ}\text{C}$ wireless rotor temperature monitoring system based on a fully passive UHF RFID sensor tag," in *Proc. IEEE MTT-S Int. Microw. Symp. Dig.*, Tampa, FL, USA, Jun. 2014, pp. 1–3.
- [11] S. Rima, A. Georgiadis, A. Collado, R. Goncalves, and N. Carvalho, "Passive UHF RFID enabled temperature sensor tag on cork substrate," in *Proc. IEEE Int. Conf. RFID Technol. Appl.*, Tampere, Finland, Sep. 2014, pp. 82–85, doi: 10.1109/RFID-TA.2014.6934205.
- [12] A. Faul and J. Naber, "Design and test of a 915 MHz, RFID-based pressure sensor for Glaucoma," in *Proc. IEEE 5th Latin Amer. Symp. Circuits Syst.*, Santiago, Chile, Feb. 2014, pp. 1–4, doi: 10.1109/LAS-CAS.2014.6820300.
- [13] S. Mondal and P. Chahal, "A passive harmonic RFID tag and interrogator development," *IEEE J. Radio Frequency Identification*, vol. 3, no. 2, pp. 98–107, Jun. 2019, doi: 10.1109/JRFID.2019.2910234.
- [14] V. Palazzi *et al.*, "Highly integrable paper-based harmonic transponder for low-power and long-range IoT applications," *IEEE Antennas Wireless Propag. Lett.*, vol. 16, pp. 3196–3199, Nov. 2017, doi: 10.1109/LAWP.2017.2768383.
- [15] N. Decarli, F. Guidi, and D. Dardari, "Passive UWB RFID for tag localization: Architectures and design," *IEEE Sensors J.*, vol. 16, no. 5, pp. 1385–1397, Mar. 2016, doi: 10.1109/JSEN.2015.2497373.
- [16] D. Dardari *et al.*, "An ultra-low power ultra-wide bandwidth positioning system," *IEEE J. Radio Frequency Identification*, vol. 4, no. 4, pp. 353–364, Dec. 2020, doi: 10.1109/JRFID.2020.3008200.
- [17] N. Decarli, M. Del Prete, D. Masotti, D. Dardari, and A. Costanzo, "High-accuracy localization of passive tags with multisine excitations," *IEEE Trans. Microw. Theory Techn.*, vol. 66, no. 12, pp. 5894–5908, Dec. 2018, doi: 10.1109/TMTT.2018.2879806.
- [18] N. Pan, D. Belo, M. Rajabi, D. Schreurs, N. B. Carvalho, and S. Pollin, "Bandwidth analysis of RF-DC converters under multisine excitation," *IEEE Trans. Microw. Theory Techn.*, vol. 66, no. 2, pp. 791–802, Feb. 2018, doi: 10.1109/TMTT.2017.2757473.
- [19] Y.-W. Chong, W. Ismail, K. Ko, and C.-Y. Lee, "Energy harvesting for wearable devices: A review," *IEEE Sensors J.*, vol. 19, no. 20, pp. 9047–9062, Oct. 15, 2019, doi: 10.1109/JSEN.2019.2925638.
- [20] F. Aktas, C. Ceken, and Y. E. Erdemli, "IoT-based healthcare framework for biomedical applications," *J. Med. Biol. Eng.*, vol. 38, no. 6, pp. 966–979, 2018, doi: 10.1007/s40846-017-0349-7.
- [21] S. Mandal, L. Turicchia, and R. Sarpeshkar, "A low-power, battery-free tag for body sensor networks," *IEEE Pervasive Comput.*, vol. 9, no. 1, pp. 71–77, Jan./Mar. 2010, doi: 10.1109/MPRV.2010.1.
- [22] F. Benassi, G. Paolini, D. Masotti, and A. Costanzo, "A wearable flexible energy-autonomous filtenna for ethanol detection at 2.45 GHz," *IEEE Trans. Microw. Theory Techn.*, vol. 69, no. 9, doi: 10.1109/TMTT.2021.3074155.
- [23] S. K. Behera and N. C. Karmakar, "Wearable chipless radio-frequency identification tags for biomedical applications: A review," *IEEE Antennas Propag. Mag.*, vol. 62, no. 3, pp. 94–104, Jun. 2020, doi: 10.1109/MAP.2020.2983978.
- [24] S. Preradovic and N. C. Karmakar, "Chipless RFID: Bar code of the future," *IEEE Microw. Mag.*, vol. 11, no. 7, pp. 87–97, Dec. 2010, doi: 10.1109/MMM.2010.938571.
- [25] L. Corchia, G. Monti, E. D. Benedetto, P. Arpaia, and L. Tarricone, "Fully-textile, wearable chipless tags for identification and tracking applications," *Sensors*, vol. 20, no. 2, p. 429, 2020, doi: 10.3390/s20020429.
- [26] S. K. Behera and N. C. Karmakar, "Chipless RFID printing technologies: A state of the art," *IEEE Microw. Mag.*, vol. 22, no. 6, pp. 64–81, Jun. 2021, doi: 10.1109/MMM.2021.3064099.
- [27] A. Vena, E. Perret and S. Tedjini, "A fully printable chipless RFID tag with detuning correction technique," *IEEE Microw. Compon. Lett.*, vol. 22, no. 4, pp. 209–211, Apr. 2012, doi: 10.1109/LMWC.2012.2188785.
- [28] M. Bhattacharjee, F. Nikbakhtnasrabadi, and R. Dahiya, "Printed chipless antenna as flexible temperature sensor," *IEEE Internet Things J.*, vol. 8, no. 6, pp. 5101–5110, Mar. 15, 2021, doi: 10.1109/JIOT.2021.3051467.
- [29] J. Aliasgari, M. Forouzandeh, and N. Karmakar, "Chipless RFID readers for frequency-coded tags: Time-domain or frequency-domain?" *IEEE J. Radio Frequency Identification*, vol. 4, no. 2, pp. 146–158, Jun. 2020, doi: 10.1109/JRFID.2020.2982822.
- [30] M. Pöppel, A. Parr, C. Mandel, R. Jakoby, and M. Vossiek, "Potential and practical limits of time-domain reflectometry chipless RFID," *IEEE Trans. Microw. Theory Techn.*, vol. 64, no. 9, pp. 2968–2976, Sep. 2016, doi: 10.1109/TMTT.2016.2593722.
- [31] L. Corchia, G. Monti, and L. Tarricone, "A fully-textile chipless tag," in *Proc. 48th European Microw. Conf. (EuMC)*, 2018, pp. 977–980, doi: 10.23919/EuMC.2018.8541420.
- [32] L. Corchia, G. Monti, and L. Tarricone, "Textile chipless tag based on frequency shift coding technique," in *Proc. 49th European Microw. Conf. (EuMC)*, 2019, pp. 500–503, doi: 10.23919/EuMC.2019.8910951.
- [33] L. Corchia, G. Monti, E. D. Benedetto and L. Tarricone, "A chipless humidity sensor for wearable applications," in *Proc. IEEE Int. Conf. RFID Technol. Appl. (RFID-TA)*, 2019, pp. 174–177, doi: 10.1109/RFID-TA.2019.8892048.
- [34] L. Corchia, G. Monti, E. De Benedetto, and L. Tarricone, "Low-cost chipless sensor tags for wearable user interfaces," *IEEE Sensors J.*, vol. 19, no. 21, pp. 10,046–10,053, Nov. 1, 2019, doi: 10.1109/JSEN.2019.2927823.
- [35] G. Monti, G. Porcino, and L. Tarricone, "Textile chipless tag for gesture recognition," *IEEE Sensors J.*, vol. 21, no. 16, pp. 18,279–18,286, Aug. 15, 2021, doi: 10.1109/JSEN.2021.3082954.
- [36] M. U. A. Khan, R. Raad, J. Foroughi, P. I. Theoharis, S. Liu, and J. Masud, "A silver-coated conductive fibre HC12 sewed chipless RFID tag on cotton fabric for wearable applications," in *Proc. IEEE 23rd Int. Multitopic Conf. (INMIC)*, 2020, pp. 1–5, doi: 10.1109/INMIC50486.2020.9318155.
- [37] A. Vena *et al.*, "Design and realization of stretchable sewn chipless RFID tags and sensors for wearable applications," in *Proc. IEEE Int. Conf. RFID (RFID)*, 2013, pp. 176–183, doi: 10.1109/RFID.2013.6548152.
- [38] T. Le, R. A. Bahr, M. M. Tentzeris, B. Song, and C. Wong, "A novel chipless RFID-based stretchable and wearable hand gesture sensor," in *Proc. European Microw. Conf. (EuMC)*, 2015, pp. 371–374.
- [39] J. G. D. Hester and M. M. Tentzeris, "Inkjet-printed flexible mm-wave van-atta reflectarrays: A solution for ultralong-range dense multitag and multisensing chipless RFID implementations for IoT smart skins," *IEEE Trans. Microw. Theory Techn.*, vol. 64, no. 12, pp. 4763–4773, Dec. 2016, doi: 10.1109/TMTT.2016.2623790.
- [40] L. Corchia, G. Monti, and L. Tarricone, "Durability of wearable antennas based on non-woven conductive fabrics: Experimental study on resistance to washing and ironing," *Int. J. Antennas Propag.*, vol. 2018, p. 8, Oct. 14, 2018.
- [41] G. Monti, L. Corchia, and L. Tarricone, "Fabrication techniques for wearable antennas," in *Proc. 42th European Radar Conf. (EuRAD)*, Nuremberg, Oct. 9–11, 2013, pp. 435–438.
- [42] L. Corchia, G. Monti, and L. Tarricone, "A frequency signature RFID chipless tag for wearable applications," *Sensors*, vol. 19, no. 3, p. 494, 2019, doi: 10.3390/s19030494.





IMAGE LICENSED BY INGRAM PUBLISHING

Internet of Things Networks

*Prerna Dhull, Andrea P. Guevara, Maral Ansari,
Sofie Pollin, Negin Shariati, and Dominique Schreurs*

Prerna Dhull (prerna.dhull@student.uts.edu.au) is with the RF and Communication Technologies Lab, University of Technology Sydney, Sydney, New South Wales, 2007, Australia, and Waves: Core Research and Engineering, Department of Electrical Engineering, KU Leuven, Leuven, 3000, Belgium. Andrea P. Guevara (andrea.guevara@esat.kuleuven.be) is with Waves: Core Research and Engineering, Department of Electrical Engineering, KU Leuven, Leuven, 3000, Belgium. Maral Ansari (maral.ansari@uts.edu.au) is with the Global Big Data Technologies Center, University of Technology Sydney, Sydney, New South Wales, 2007, Australia. Sofie Pollin (sofie.pollin@kuleuven.be) is with Waves: Core Research and Engineering, Department of Electrical Engineering, KU Leuven, Leuven, 3000, Belgium. Negin Shariati (negin.shariati@uts.edu.au) is with the RF and Communication Technologies Lab, University of Technology Sydney, Sydney, New South Wales, 2007, Australia.

Dominique Schreurs (dominique.schreurs@kuleuven.be) is with Waves: Core Research and Engineering, Department of Electrical Engineering, KU Leuven, Leuven, 3000, Belgium.

Digital Object Identifier 10.1109/MMM.2021.3130710

Date of current version: 3 February 2022

The number of sensors deployed in the world is expected to explode in the near future. At this moment, nearly 30 billion Internet of Things (IoT) devices are connected, and the number is expected to double in the next four years. While not all of these are battery powered, as technology becomes smaller and mobility becomes more important to consumers, soon a larger portion will be. This forecast predicts that the number of machine-to-machine devices will have the largest increase, representing nearly 50% of all devices in 2023 [1], [2]. These devices are typically small and therefore ideal candidates to be wirelessly powered. Typical examples are health-care monitoring, smart homes, and industrial applications.

Since IoT devices are embedded in wireless sensor networks and communicate with base stations (BSs), the logical step is to have a BS transmit both power and information wirelessly to the appliances via the same RF signal, as demonstrated in Figure 1, while the sensor node performs information detection and energy harvesting operations across the same RF signal. This approach has been termed *simultaneous wireless information and power transfer (SWIPT)*, from *wireless information transfer (WIT)* and *wireless power transfer (WPT)*. In WIT, a signal is utilized only for information transmission, whereas in WPT, the signal is employed only to deliver power to a node. SWIPT provides a bridge between these two technologies by exploiting the same signal for providing information and power to IoT devices. In this article, we focus on downlink WIT only. An IoT sensor node would typically send sensed data to a BS, using backscattering or another approach, representing uplink WIT. Further, as seen in Figure 1, there has to be a power management unit between the information receiver and power storage unit, which consumes very low energy levels [3]. However, in this article, this is considered part of the power storage system so as to keep the receiver architecture representation simple.

From a WPT perspective, it would be beneficial to transmit the RF signal only to the IoT nodes that need power, avoiding wasting energy on the rest of them. The solution to this can be beamforming. Beamforming, or spatial filtering, is a technique used in arrays for directional

signal transmission (or reception). Beamforming achieves this property by coherently combining the fields radiated by array elements to direct their radiated energy in particular directions. These multiple beams are created at a BS to communicate with different IoT nodes simultaneously [4].

In a wireless communication system, antenna characteristics that have high directivity and a wide beamwidth can be used for long-distance and multiuser coverage. BS antennas for WPT with such performance can broadcast and deliver wireless power to a large number of widely distributed IoT users. However, omnidirectional antenna transmission, which radiates in all directions, increases interference. In such situations, the use of narrow directional beams enhances the signal-to-interference-noise ratio by sending the signal toward a specific user and achieves higher data rates by reducing multipath effects and interference [5]–[7], as evident in Figure 2. In Table 1, some of the pros and cons of using beamforming are summarized. On balance, beamforming not only enhances WIT performance but also WPT performance, and this makes it a suitable candidate for SWIPT systems.

Compared to conventional transmission design, the implementation of beamforming techniques requires additional signal processing at the transmitter. Further, beamforming utilizes large antenna arrays for steering the narrow beams to enlarge the coverage area, which results in high-cost and high-power-consumption systems. Besides, employing such large arrays makes the systems bulky and less efficient than traditional ones. However, with the recent advances in hybrid antenna arrays, employing a combination of analog and digital beamforming techniques serves as a cost- and energy-efficient alternative. Therefore, today's beamforming can serve as a potential solution for SWIPT, and it is expected to improve WPT as well as WIT.

In addition to signal covering capabilities, it is essential to take into account the IoT node architecture. Prior to SWIPT, receiver structures were studied separately either for wireless communication purposes only or energy harvesting purposes only, whereas now these operations need to be performed on the same signal at the IoT node side. Therefore, the problem of integrating these two processes in an efficient manner arises [8]. Initially, in 2013, two

types of receiver setups were introduced, as detailed in Figure 3. The first was a separated information–energy receiver architecture, where the signal was divided between two streams, one for information decoding and the other for energy harvesting. Various signal splitting techniques could be considered, such as time switching (TS) and power splitting (PS). The second setup was

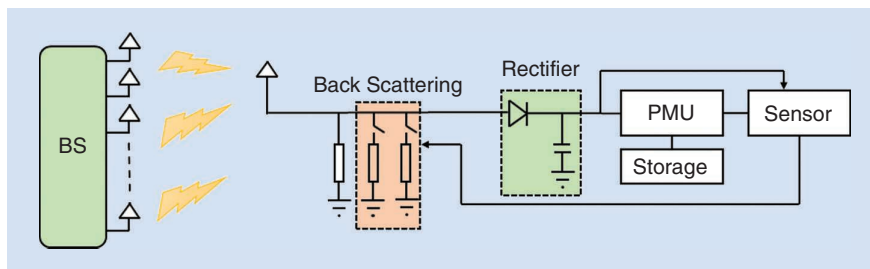


Figure 1. A BS transmitting to a sensor node consisting of a rectifier, power management unit (PMU), storage unit for power extraction, and backscattering for an information transfer from the received signal.

an integrated information–energy receiver, where signal splitting was performed only after passing the whole signal through the rectifying circuit (i.e., no RF mixer was required at the receiver [9]).

For both SWIPT architectures, there is a tradeoff between the achievable information rate and amount of harvested power, as both metrics cannot be simultaneously maximized [9]. Further, the use of an energy harvester (rectifying circuitry consisting of diodes) at the receiver introduces nonlinearity into a SWIPT system, and this nonlinearity significantly affects the power conversion efficiency (PCE) at the output [10]. Due to this nonlinearity, the output power is not only a function of the received signal power but also the received signal shape. For example, a waveform having a higher peak-to-average-power ratio (PAPR) with the same average input power is able to turn on the diode earlier, resulting in increased PCE at the output.

However, these high-PAPR waveforms deteriorate the WIT performance because of saturation of the nonlinear amplifier at the transmitter. From a SWIPT system perspective, the performance of both the WIT and the WPT is important, and it is therefore necessary to maximize the rate–energy tradeoff at the receiver. Thus, for a complete SWIPT system, we need to codesign not only the transmitter and receiver hardware but also the transmitted waveform for a particular type of IoT node architecture to enhance performance. Based on the preceding discussion, this article reviews two questions related to BSs: How can a BS utilize beamforming for sending power to specific IoT devices while avoiding wasting energy in irrelevant zones? How can signal transmission by a BS be optimized for a particular IoT receiver architecture so that the strongly energy-constrained IoT node can receive information and power efficiently?

Beamforming at a BS

A BS can achieve beamforming in multiple ways. Digital beamforming, including multiple-input, multiple-output (MIMO) signal processing, is the most flexible approach to control the power direction. However, conventional, fully digital beamforming with one dedicated RF chain for the transmit antenna is too costly in terms of power consumption, as it is necessary to have a separate power amplifier for each RF chain. In addition, all the antennas must be perfectly synchronized to avoid signal distortion during uplink

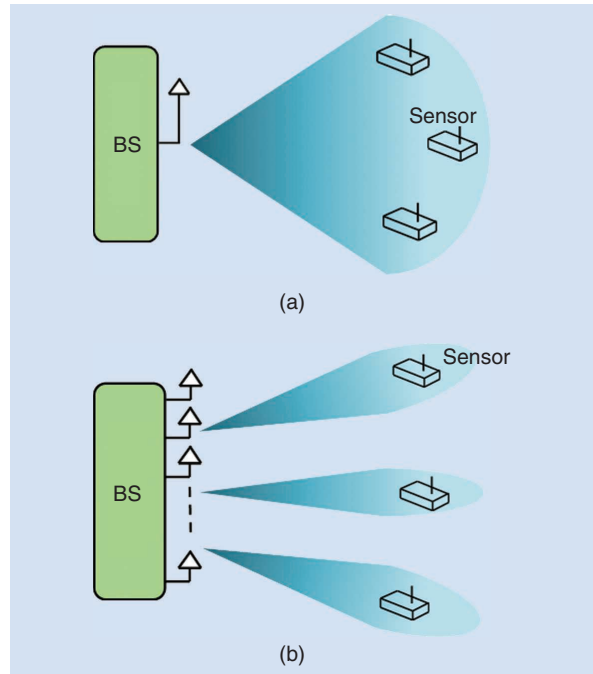


Figure 2. BS coverage using (a) a single antenna compared to adopting (b) a beamforming antenna array.

TABLE 1. The beamforming deployment in wireless networks.

Advantages	Disadvantages
<ul style="list-style-type: none"> • Increased capacity • Reduced interference • Increased coverage area • Improved transmission efficiency 	<ul style="list-style-type: none"> • Higher complexity • Higher cost • Larger sizes

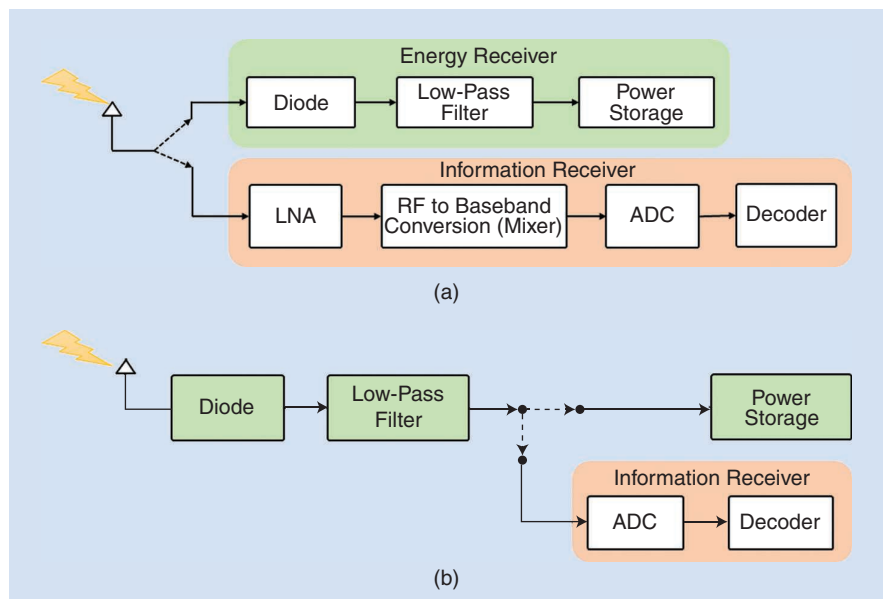


Figure 3. SWIPT architectures: (a) a separated information–energy receiver and (b) an integrated information–energy receiver [9]. LNA: low-noise amplifier; ADC: analog-to-digital converter.

It would be beneficial to transmit the RF signal only to the IoT nodes that need power, avoiding wasting energy on the rest of them.

and downlink data transmission. A cost- and energy-efficient solution is analog multiple-beam antenna arrays. Most such antennas can be phased to synthesize a broad coverage beam, but the energy transmitter needs a very large number of antennas and adaptive beamforming to flexibly control the power direction. However, hybrid beamforming is able to achieve the same optimal performance as fully digital beamforming as long as the number of RF chains at the transmitter is no less than twice the number of subbands or twice the number of channel paths [11]. In the following, we first review approaches for analog beamforming that are applicable for SWIPT. Due to the steep increase in IoT nodes, BSs are evolving toward a massive number of antennas, adopting digital beamforming or, as mentioned, a hybrid digital/analog approach. An experimental study mimicking 120 users is presented in the “Digital Beamforming” section.

Analog Beamforming

There are different types of analog beamforming that can be used in wireless applications. These include circuit-type [12] and quasi-optical beamforming networks (BFNs) [13],

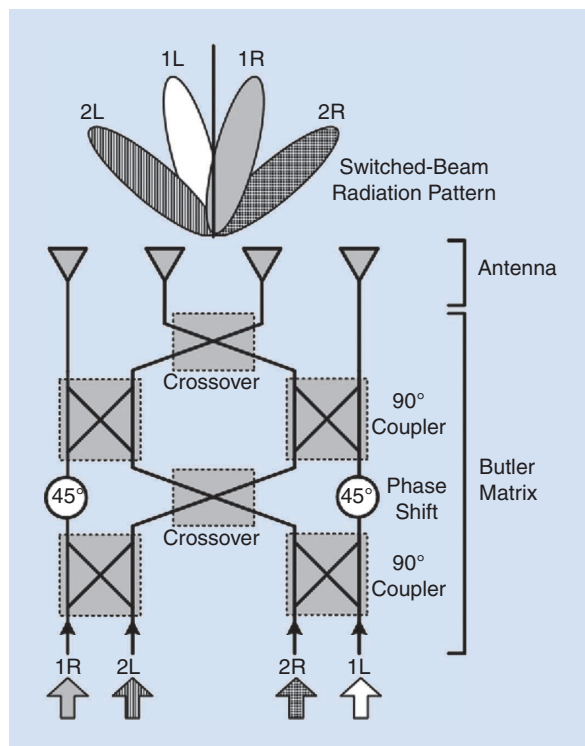


Figure 4. The conventional 4×4 Butler matrix [18].

the latter of which are more desirable for higher-frequency communication systems. In this article, circuit-type BFNs are presented that have greater significance for SWIPT. A BFN is a physical layer element of an array system that combines signals with the amplitudes and phases required to produce a desired angular distribution of the emitted radiation (i.e., one or more beams pointing in prescribed directions). Energy delivered to a particular input port of a BFN is thus associated with a specific beam radiated by the antenna elements connected to the BFN’s output ports [4]. In the following, the two most-used circuit-type BFNs are introduced.

Butler Matrix

The Butler matrix was first described by Butler and Lowe in [14]. It offers a set of orthogonal beams, with the beam directions dependent on the frequency. An $M \times N$ Butler matrix consists of M number of inputs that independently feed N number of outputs with progressive phase delays. Inputs and outputs are well matched and isolated, and the network is theoretically lossless [15]. There is no beam spacing loss, due to the nature of orthogonal beams [16], [17]. The outputs of the Butler matrix can be connected to an antenna array to produce the required amplitude and phase for the antenna elements to enable beam switching capabilities.

Consider a Butler matrix a microwave network with four input and four output ports, as illustrated in Figure 4. The network consists of several microwave components, including couplers, phase shifters, and crossovers. It has the special characteristic that if a signal is applied to input i ($i = 1, 2, 3, 4$), then the outputs all have equal amplitude, and output j ($j = 1, 2, 3, 4$) has phase $360(j - 1)(i - 1) / n$ degrees, which means that feeding element i radiates a beam at the $\sin^{-1}[\lambda i - 1 / sn]$ azimuth, where s is the spacing of the columns. To produce more-focused and narrower beams as required for SWIPT, high-gain antenna arrays are necessary. The array gain is the increase in the average signal-to-noise-ratio (SNR) obtained by combining multiple antenna elements rather than using a single one. To increase the gain of the array, the Butler matrix outputs i must increase. The amplitude of these outputs should have unequal powers to achieve lower sidelobes because of nonuniform illumination. A prototype Butler matrix design covering the preceding requirements is presented in [19]. The reported multibeam antenna can create four beams in the azimuth plane. The measured radiation patterns show that the beams cover a spatial range of roughly 90° . The design architecture and final prototype are provided in Figure 5. Recently, a compact 4×4 Butler matrix for IoT applications was presented in [20]. The structure operates from 2.35 to 2.55 GHz, which covers the industrial, scientific, and medical bandwidth (BW). Small dimensions of 31.3×22.9 mm make this design useful for IoT applications.

Nolen Matrix

The Nolen matrix was first proposed by John C. Nolen [21]. In Figure 6, there is a schematic diagram of an M -entry Nolen matrix. A Nolen matrix is a lossless variant of a Blass matrix in which all the directional couplers below the diagonal have been removed. Consequently, all the matched loads at the end of the feeder lines have been removed. In a Blass matrix, any signal above the diagonal will necessarily be dissipated in the matched loads. To eliminate these losses, no signal should go beyond the diagonal of the directional coupler matrix. This can be obtained along the diagonal, with directional couplers that have coupling values of 0 dB, which is the functional schematic of the Nolen matrix. In summary, the Nolen matrix may be considered an asymptotic singular case of a Blass matrix for which the design constraint is on the values of the directional couplers. Nolen matrices can be used for WPT beamforming applications. A symmetrical 3×3 uniplanar Nolen matrix is introduced in [22], where the design reduces the number of phase shifters and does not require outside phase compensation lines. The design architecture and final prototype of the 3×3 Nolen matrix feeding network are in Figure 7.

In conclusion, employing analog beamformers is an energy-efficient and low-cost solution for realizing a high-directivity linear array with a narrow beamwidth in one principal plane. These are one form of the cost-effective implementation of beamforming on a printed circuit board substrate, while benefiting from a compact size. In [24], the authors introduce practical application examples of such beamformers for broadcasting wireless power to multiple IoT devices that are remotely located. The array broadcasts wireless power to multiple IoT targets at different elevations. Analog beamformers can be used to enhance the end-to-end power transfer efficiency from the transmitter to the receiver. Conventional systems achieved this by using bulky structures, such as parabolic reflectors, where the antenna needs to be mechanically adjusted to focus the signal toward the receiver.

Digital Beamforming

In wireless IoT networks, BSs have to communicate with and send power to a high number of nodes. For this reason, BSs are evolving toward massive MIMO architectures, meaning that a large number of antennas is deployed. Those antennas can be allocated in a centralized or distributed manner [25], [26]. In communications, the power leakage in space can lead to interference when users are active in those areas. Therefore, different digital beamforming techniques, such as maximum-ratio transmission/maximum-ratio combining (MRT/MRC) [27], zero forcing (ZF) [28], regularized ZF (RZF) [29], and the minimum mean-square error (MMSE) [30], are used to nullify unwanted areas. The differences among these beamforming methods are summarized in Table 2.

Few experimental studies analyze the impact of power leakage in massive MIMO systems. In [31], two off-the-shelf receivers measure the leakage power in a centralized massive MIMO system. The difference between them is whether the wireless channel knowledge is present at the receiver or not. This work presents the measured harvested output voltage as a function of the linear distance (up to 1 m) between the target user and leakage receiver. Although the number of samples is limited, this work provides initial

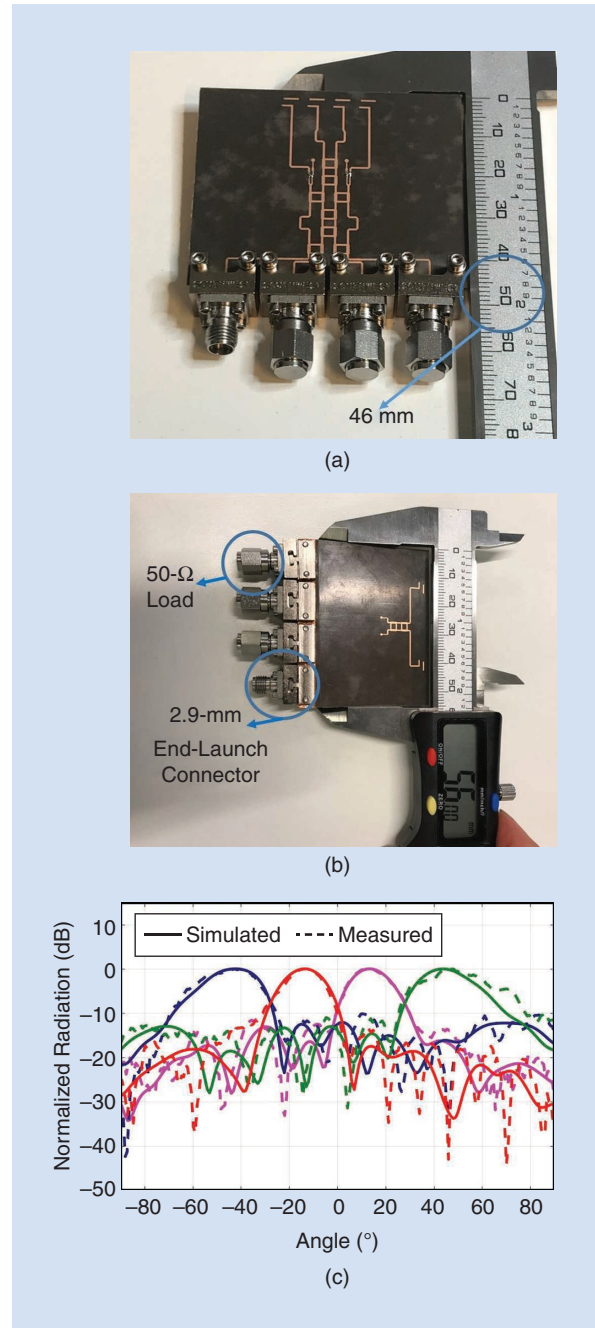


Figure 5. The fabricated four-beam antenna array using conventional 4×6 Butler matrix [19]. (a) The top view. (b) The bottom view. (c) The simulated and measured beams.

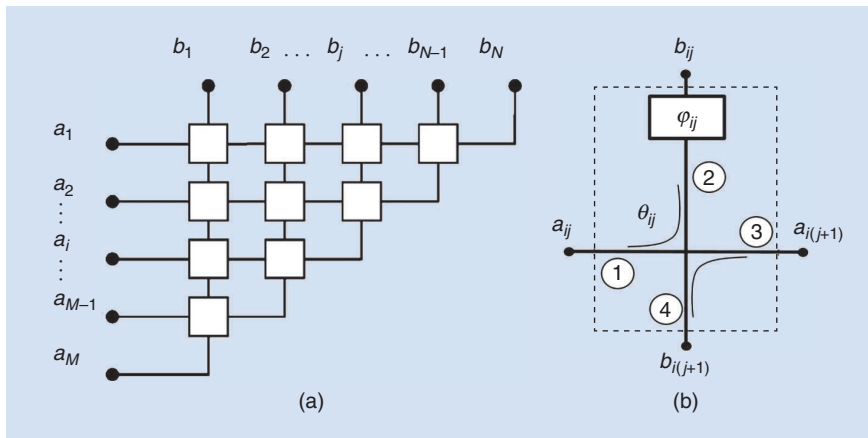


Figure 6. (a) M -entry Nolen matrices. (b) Details of each node [23].

experimental insight into the potential use of massive MIMO and digital beamforming for power transfer. A more extensive measurement campaign was conducted at KU Leuven [26], [32], [33]. An automated massive MIMO experiment analyzed three antenna configurations and the corresponding leakage power impact in an indoor scenario. The power leakage was approximated based on the wireless channel knowledge collected for 120 locations.

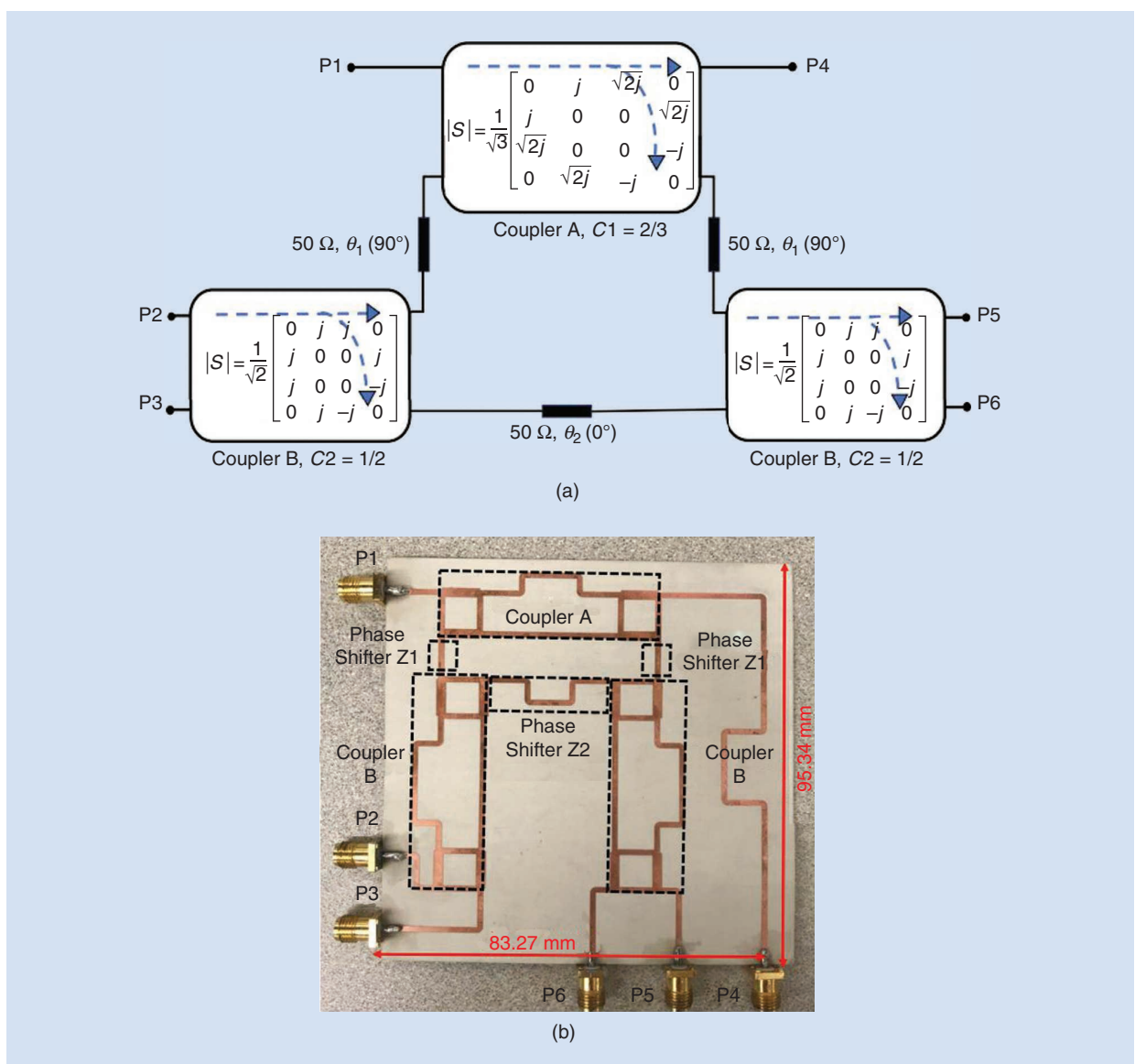


Figure 7. A 3×3 Nolen matrix with lumped-element couplers and phase shifters. (a) A simulated layout. (b) The fabricated device [22].

Experimental Setup

The KU Leuven massive MIMO testbed used for this measurement campaign consists of two elements: a 64-patch-antenna BS (Figure 8) and two Universal Software Radio Peripherals (USRPs), by which each USRP is associated with two pieces of user equipment (UE). The modular patch antennas enable different configurations. In this case, we evaluate the following three antenna array topologies:

- *Uniform rectangular array (URA)*: The 64-patch antennas are deployed in a rectangular array of 8×8 [see Figure 8(a)].
- *Uniform linear array (ULA)*: The 64-patch antennas are lined up next to one another in a horizontal array of 1×64 [see Figure 8(b)].
- *Distributed ULA (D-ULA)*: The 64-patch antennas are distributed around the analyzed area in eight ULA arrays of 1×8 each [see Figure 8(c)].

Each UE device controls two independent uplink data streams associated with two dipole antennas. The uplink channel is estimated with these data streams. The four dipole antenna elements are connected to four positioning systems that can freely move in a grid of 1.3×1.3 m. All the positioners synchronously move 20 cm horizontally and 30 cm vertically, then stop for 10 s. The wireless channels between the four dipole antennas (at the UE devices) and

Beamforming is significantly helpful in reducing the interference among users while focusing power on only the desired entity.

the 64-patch antennas (at the BS) are collected throughout this period. During postprocessing, the wireless channel of each position is treated as an independent virtual user. In this way, we can create a massive MIMO scenario with 120 users deployed on the ground [34], [35].

Experimental Results

Figure 9 gives the heat map with contours for the experimental setup for a different number of active antennas at the BS. The target user is located in the center of each subfigure. The digital beamforming MRT is applied toward the target user. Those figures represent the estimated leakage in the studied area as the normalized received signal over 0 dB. It is clear that the strongest yellow peak is visible for the target user, and the power distribution follows a beam for the URA and ULA scenarios. It is interesting to see that with MRT beamforming, the amplitude of the weakest signal can be up to 30 dB lower than the

TABLE 2. The beamforming techniques for wireless networks.

Precoding/Combining Vector	Advantages	Disadvantages
MRT/MRC [27]	<ul style="list-style-type: none"> • Lower computational complexity • Maximizes the power directed toward the desired user/sensor 	<ul style="list-style-type: none"> • Does not actively suppress leakage • Provides the lowest spectral efficiency and capacity for a massive MIMO system
ZF [28]	<ul style="list-style-type: none"> • Actively suppresses leakage 	<ul style="list-style-type: none"> • Tradeoff between leakage suppression and power directed toward the desired user/sensor • Does not work in systems with a lower SNR
RZF [29]	<ul style="list-style-type: none"> • Actively suppresses interference plus noise 	<ul style="list-style-type: none"> • Requires an estimation of the system SNR
MMSE [30]	<ul style="list-style-type: none"> • Provides optimal system performance by suppressing intra- and intercell interference and noise 	<ul style="list-style-type: none"> • Computationally costly • Requires knowledge of the channels of all users that are served and not served by the BS

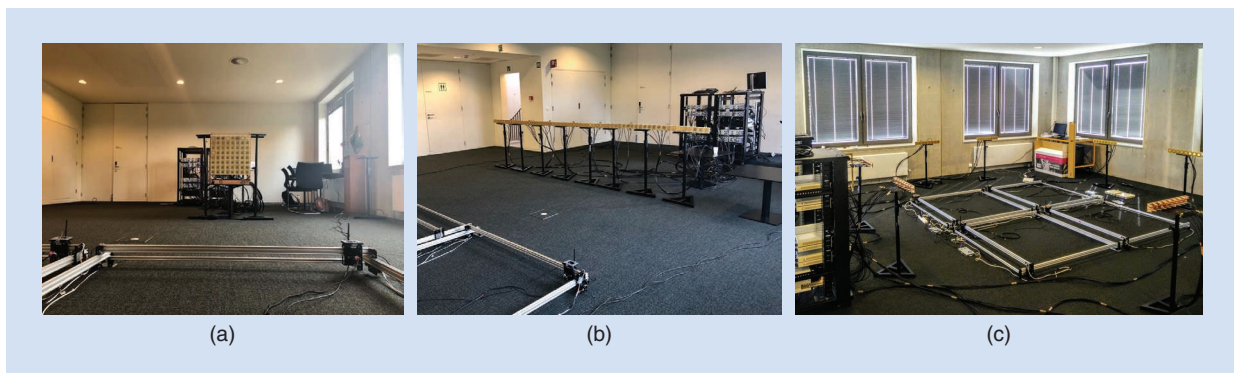


Figure 8. The KU Leuven massive MIMO antenna configurations. (a) The URA. (b) The ULA. (c) The D-ULA.

peak amplitude of the strongest signal. However, these dark blue spots mainly occur in the ULA scenario. For the D-ULA topology, the spot beams are noticeable, especially for the scenario with 64 distributed antenna elements.

From the performed experiments, it can be observed that beamforming is significantly helpful in reducing the interference among users while focusing power on only the desired entity. Therefore, beamforming can be

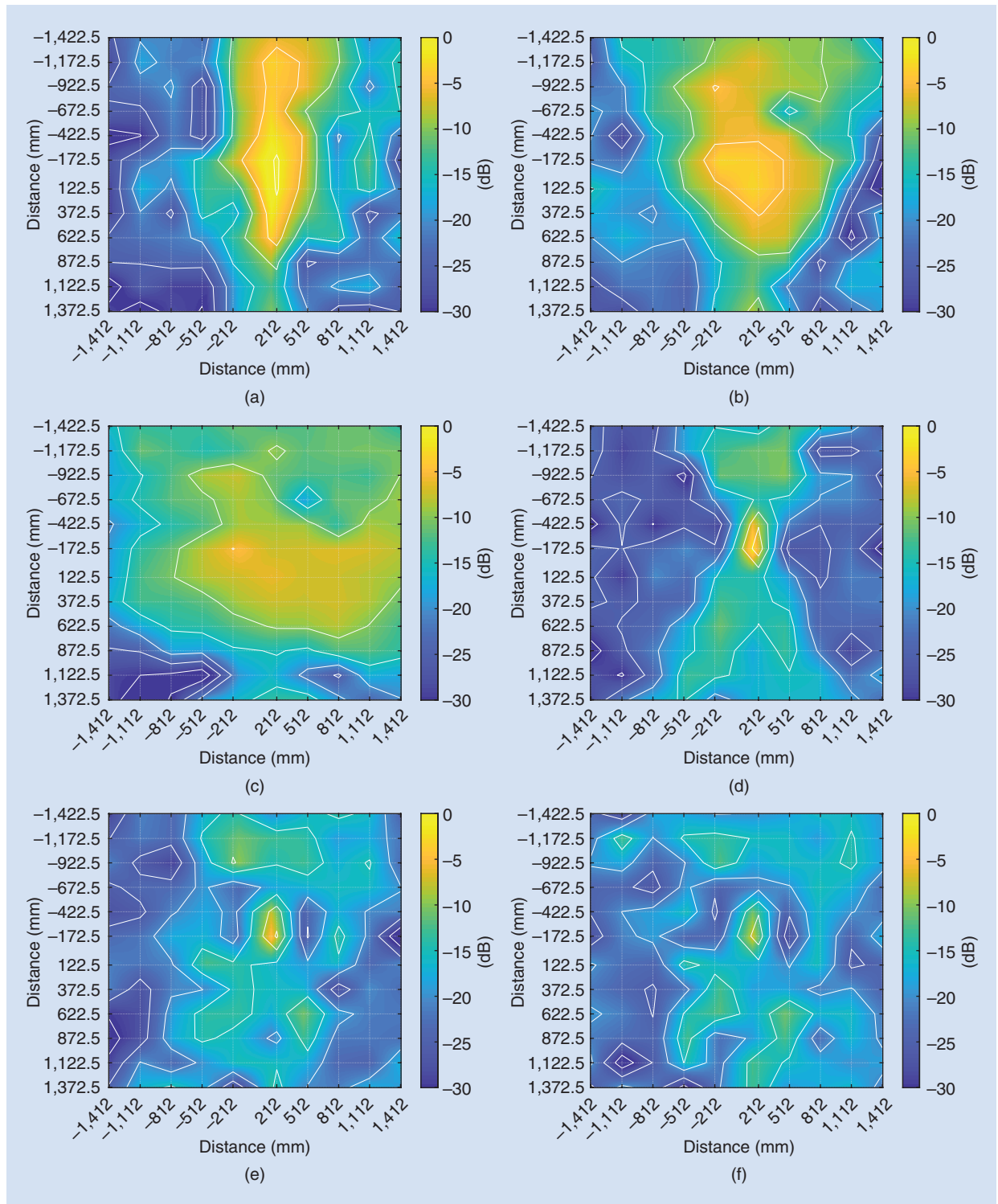


Figure 9. Contouring normalized over 0 dB, which is the maximum value received by the target user in each antenna configuration, regardless of the number of active antennas. (a) A URA with 64 antennas. (b) A URA with 32 antennas. (c) A URA with 16 antennas. (d) A ULA with 64 antennas. (e) A ULA with 32 antennas. (f) A ULA with 16 antennas. (Continued)

utilized for careful power management in SWIPT systems where information and power delivery are of critical importance.

SWIPT Signal Design at a BS

For an overall energy-efficient SWIPT system, effective delivery of the RF signal power to the UE is important, and it is also necessary to maximize the amount of harvested energy at the receiver while providing a sufficient data rate. It has recently been observed that different signal waveforms result in various energy efficiencies at the receiver. Therefore, the area of SWIPT signal design with the corresponding modified receiver architectures also needs to be explored to enhance the end-to-end SWIPT performance. In this article, various SWIPT waveforms to enhance system performance are discussed along with an explanation of how the corresponding receiver architecture needs to be redesigned. The focus is, however, on the general receiver architecture, whereas the required SWIPT receiver implementation details can be

found in [36], where near- and far-field SWIPT technologies are discussed.

As mentioned, in SWIPT systems, it is not possible to maximize the information transfer rate and amount of harvested energy simultaneously, and a tradeoff exists between these two objectives. For a long time, high-PAPR signals have been used to enhance WPT system performance, and this has been achieved in multiple ways. One approach to designing a higher-PAPR signal with the same average input power is to concentrate the signal power within a shorter duration instead of covering the complete duty cycle [37], and it has been shown that to obtain an output voltage of 1.6 V, only -5.1 decibel milliwatts (dBm) of input power are required for a pulsed signal instead of -3.44 dBm for a continuous waveform.

Another way to increase the PAPR of the input signal at the receiver is to use a multitone signal instead of a single-tone one [10]. Since the diode (or diodes) in the receiver node is nonlinear, the multiple tones present in the received signal undergo intermodulation,

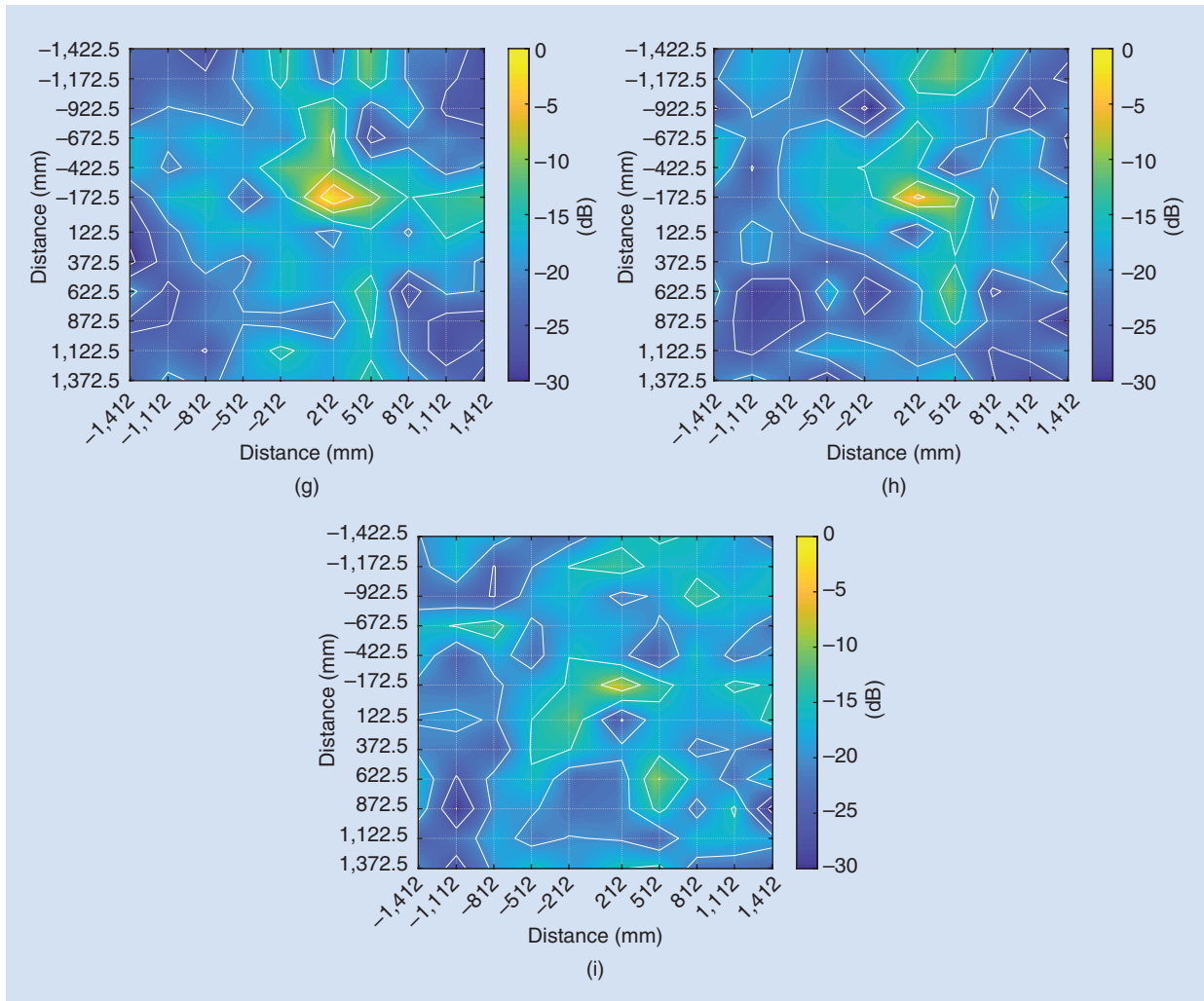


Figure 9. (Continued) (g) A D-ULA with 64 antennas. (h) A D-ULA with 32 antennas. (i) A D-ULA with 16 antennas.

It is necessary to consider a practical SWIPT scenario in which the transmitter and receiver power consumption is also considered.

resulting in multiple frequency components in the baseband, corresponding to a time domain voltage ripple in addition to the desired dc voltage, negatively impacting the PCE. Therefore, the several parameters affecting this ripple—such as number of tones, the number of tone separations, the number of tone phases, the input power range, the rectifier's low-pass filter's cutoff frequency, and the diodes—have to be carefully studied [38]–[41].

However, in a SWIPT system, where information transmission and power transfer are required, the additional ripple can actually be exploited from the information perspective. Consequently, the signal excitation design at the BS is a challenging task. In practice, the shape of the waveform transmitted by the BS may be altered before it reaches the receiver node, due to multipath effects in the wireless channel. This can be mitigated with precoding and pre-equalization techniques. The former was touched on in the “Digital Beamforming” section. Regarding the latter, a nondispersive wireless channel is assumed in this work for simplicity.

In a communication system, the actual modulated waveform varies through time, as opposed to the deterministic multitone signal used for WPT, since streams of symbols are sent between the BS and IoT node. This randomness often results in a lower PCE compared to the deterministic multisine waveform [42]. The modulated waveform is defined by several parameters, such as the type of waveform, modulation scheme, modulation order, symbol rate, and input distribution, which can affect the energy harvesting and communication performance. The values of the parameters can be chosen to reach a tradeoff and favor either WPT or communication if one aspect is more critical for a practical application. In the following, we discuss modulated waveforms for SWIPT, making a distinction between the two-node receiver configurations under consideration, as presented in Figure 3.

Separated Node Architecture

First, we focus on the node architecture in which the received RF signal is divided into two streams: one for the information signal and the other for the power signal, corresponding to Figure 3(a). This is usually performed with the help of a power divider with a certain power ratio for the energy harvesting performance at the receiver output. The inclusion of a separated node architecture at the receiver offers the advantage of using existing transmission schemes, such as orthogonal frequency-division multiplexing

(OFDM), which is a combination of multiple subcarriers. This requires only slight modifications in the transmitted signal and receiver architecture. The reason for this is the use of existing communication system information detection methods, as signal splitting is performed in the RF domain for the two separate paths and only an additional energy harvester is required at the receiver. However, this is attained at the cost of higher power consumption at the receiver due to the presence of mixers/fast Fourier transforms (FFTs).

One way to achieve separate signals for information and energy transfer is to segregate these OFDM subcarriers into two sets, as in Figure 10(a), by using well-designed bandpass filters (BPFs) and therefore eliminating the need for PS and TS at the receiver [43]. It is possible to harvest 18 mW for 4 b/s/Hz from the transmitted signal power of 1 W using this OFDM subcarrier splitting technique. However, here, the required BPFs need to be really sharp to support an OFDM signal having smaller subcarrier frequencies. This increases the computational complexity at the receiver because of the increased discrete Fourier transform length [44], consequently increasing the power consumption at the receiver. Therefore, it is necessary to monitor the signal processing power consumption at the receiver to check the feasibility of this scheme.

An alternative, tailored to the PS configuration, is to superimpose an additional multisine on the OFDM waveform, as illustrated in Figure 10(b), to further enhance the PAPR [45]. For a 20-dB SNR, information and power performance of 1 b/s/Hz and around a 1.8- μ A current can be attained for the combination of OFDM and a 16-tone deterministic multitone. Although the only modification needed in this receiver architecture is the incorporation of the cancellation of this multisine waveform, the drawback is that the receiver's analog-to-digital converter (ADC) may suffer from saturation when the power signal level is relatively higher than the information signal.

Another way to capitalize on the high-PAPR OFDM signal for energy harvesting is to exploit its redundant cyclic prefix (CP), as demonstrated in Figure 10(c). In this approach, a high-PAPR rectangular pulse for power transfer can be superimposed on the CP of the OFDM information signal [46]. Because the CP is discarded for information decoding, no modification is required in the information receiver, and 1.4 V can be harvested in a -15-dB SNR environment. However, the proper functioning of this signal requires the optimization of the rectangular pulsewidth to minimize interference with the information component of the signal. Another approach for using the redundant CP for power transfer is proposed in [47]. There, instead of transmitting a separate power signal across the OFDM signal, some portion of the information component is utilized for energy harvesting in addition to the CP, and the length of this information component for energy harvesting is optimized according to the energy requirement at the receiver.

In [48], directly superimposing a dc signal across the OFDM signal to make an OFDM–dc signal is proposed. In such a case, the power can be directly transferred in dc in addition to the OFDM information signal. The design is able to have 2 mW of power and a symbol error rate (SER) of 10^{-1} for a 10-dB SNR with 2 b/channel of the quadrature phase-shift keying (QPSK) OFDM–dc signal. This technique offers the advantage of eliminating nonlinear rectifying components (which saturate the PCE in rectifier-based schemes) at the receiver, and a low-pass filter is sufficient for power conversion. However, the drawback is that the approach requires a complete redesign of the transmitter and receiver architectures.

Instead of dividing the received signal stream into two signal streams using PS and TS, dividing the symbol constellation points to enhance the SER performance of the system is introduced in [49]. There, hybrid constellation shaping is utilized to map constellation points such that symbols closer to the origin will be recognized as information symbols, and symbols farther from the origin, having larger amounts of energy, will be considered energy symbols. It is assumed that the receiver has prior knowledge of the constellation points' functions. This approach has been shown to increase the SER performance compared to the earlier PS-based scheme. Another symbol designing scheme was introduced in [50], where asymmetric QPSK

Generally, most of the research challenges for enhancing PCE in WPT systems revolve around the problem of reducing the ripple present in the output voltage.

with constellation points inclined more toward the zero-phase value is shown to have an improved rate–energy tradeoff compared to the general QPSK performance.

The performance of the transmission designs discussed in the preceding is summarized and compared in Table 3 in terms of advantages, disadvantages, achievable information transfer rates, and harvested energy under different received power levels and SNR scenarios. Note that a separated information–energy receiver architecture offers the benefit of transmitting information by using an OFDM signal, as the portion of the signal being utilized for power delivery can be separated from the information signal with the help of distinguishing the information and power frequency bands. After the separation of the information and power signals, information processing can be performed as usual. However, this would not be efficient in a practical SWIPT system, as the power required for OFDM signal processing is substantial. Therefore, it is necessary to

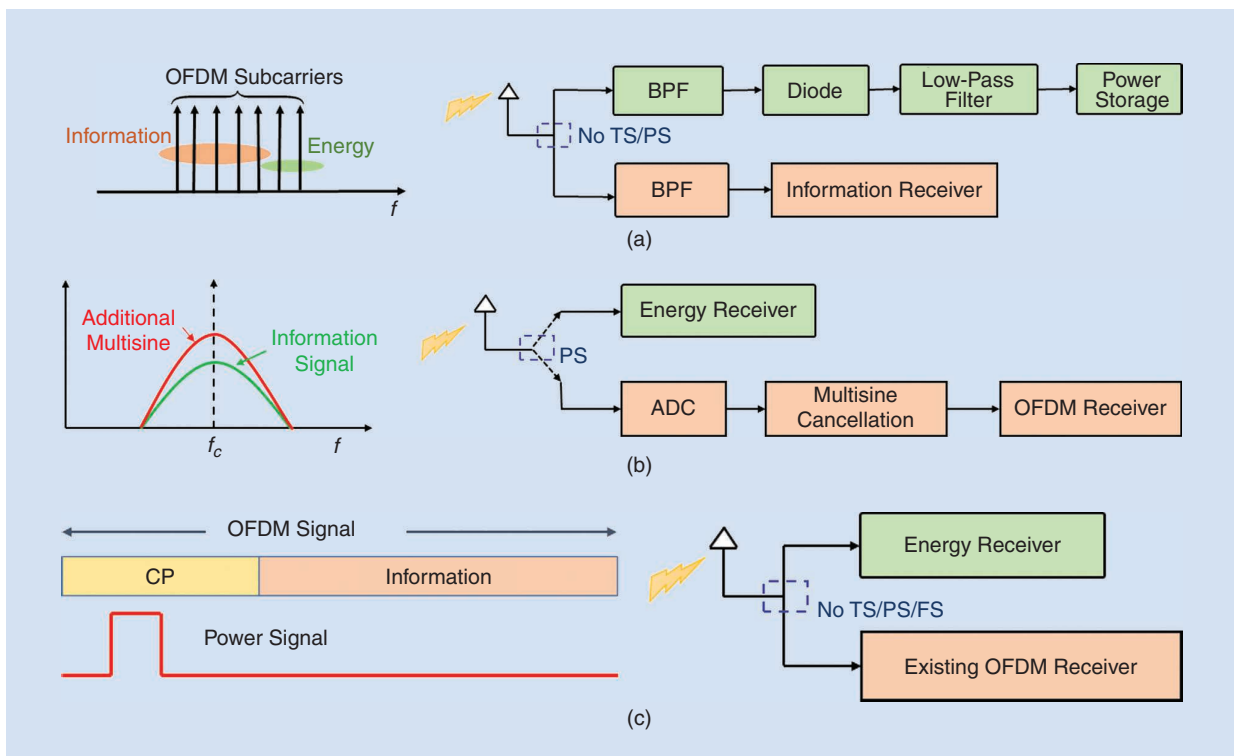


Figure 10. Waveforms and the corresponding receiver architecture for the separated information–power configuration. (a) The OFDM frequency spectrum and corresponding receiver architecture. (b) The frequency spectra of the multisine superimposed on the OFDM information signal and corresponding receiver architecture. (c) The CP–OFDM information symbol superimposed on the rectangular pulse power signal. BPF: bandpass filter.

consider a practical SWIPT scenario in which the transmitter and receiver power consumption is also considered. In this direction, the idea of using an integrated information–energy receiver architecture to reduce receiver power consumption is discussed in the next section.

Integrated Node Architecture

The previously discussed methods are tailored to the separated receiver architecture, in which it is assumed that the receiver has two signal streams, namely, one for information and one for energy. In the case of an integrated architecture [Figure 3(b)], the received signal is first passed through the rectifier, and the resulting baseband signal is divided between two streams, one for energy and the other for information, using a voltage divider. Since this architecture offers the advantage of eliminating the RF mixer as well as its driving local oscillator, the overall receiver’s power consumption reduces by a significant factor. However, new modulation approaches need to be explored for such a receiver design.

The simplest modulation technique for an integrated receiver was introduced in 2013 [9]. It adopted single-tone energy modulation, where information symbols were encoded using different energy levels, which is also referred to as *energy modulation*. However, it does not take advantage of multitone signals for increased power performance. To consider these high-PAPR multitone signals for an integrated node architecture, new techniques for embedding information across these signals and for further decoding at the receiver need to be developed.

One way of utilizing high-PAPR multitone signals for SWIPT systems is to design the multitone waveform with different PAPR levels for each symbol [51]. As represented

in Figure 11, multiple PAPR levels are produced by varying the number of tones and the tone spacing. A data rate of 0.5 Mb/s with a 10^{-2} bit error rate (BER) and dc output that is 3.5 times higher than a single-tone carrier can be achieved for a 30-dB SNR. However, in [51], the signal BW keeps changing for each symbol, putting additional constraints on the input matching network for large modulation orders. Therefore, PAPR-based information transfer using a fixed-BW multitone signal is proposed in [52], where the tone spacing is changed for each transmitted symbol. This approach has been shown to perform better than varying the BW of the multitone signal under low-SNR transmission conditions.

These high-PAPR-based modulation techniques can be combined with single-tone based approaches to widen the operating region to make the overall SWIPT system more efficient. For example, multitone waveforms outperform single-tone ones only in the case of a low-power region, as the diode enters the saturation region at a comparatively higher input power [53]. Therefore, an adaptive receiver structure was presented in [54], with a switching option between information paths for single- and multitone methods according to the received input power levels.

Furthermore, in [55], a transmission approach is developed from a transmitter perspective. Here, instead of focusing on RF–dc efficiency at the receiver, the dc–RF efficiency at the transmitter is improved. Hence, a low-PAPR signal is designed by superimposing a high-power, unmodulated, continuous-wave power signal on the modulated signal, as demonstrated in Figure 12. In this way, interference between the information and energy signals is minimized by allocating power to the narrowband and information to the wider band. This idea might be feasible

TABLE 3. The transmission designs for a separated receiver architecture.

Transmission Approach	Advantages	Drawbacks	Information Rate and Energy
OFDM frequency spectrum splitting [43]	<ul style="list-style-type: none"> No PS or TS needed 	<ul style="list-style-type: none"> Well-designed BPF needed Linear energy harvester model considered 	4 b/s/Hz and 18 mW for SNR = 50 dB
Multisine superimposed on OFDM [45]	<ul style="list-style-type: none"> Higher PAPR 	<ul style="list-style-type: none"> Saturation of ADC may occur 	1.8 μ A for 1 b/s/Hz for SNR = 20 dB
Rectangular pulse superimposed on CP–OFDM [46]	<ul style="list-style-type: none"> No modification in information detection 	<ul style="list-style-type: none"> Interference introduced according to the width of the rectangular pulse 	1.4 V (maximum) at received input power of –15 dBm
Partial use of information component of OFDM [47]	<ul style="list-style-type: none"> No modification in information detection 	<ul style="list-style-type: none"> Optimization needed for minimum usage of information part for sufficient harvested energy 	~38% PCE for 2 b/subcarrier channel for SNR = 20 dB
OFDM–dc signal [48]	<ul style="list-style-type: none"> Rectifying components, such as diodes, are not required Low-pass filter is sufficient to extract the dc 	<ul style="list-style-type: none"> Complete redesign of transmitter and receiver 	2 mW and SER = 10^{-1} with 2 b/channel at SNR = 10 dB

in practical scenarios where the power signal generally needs to have much higher power than the information signal does (i.e., 0 dBm for power and -100 dBm for information).

Generally, most of the research challenges for enhancing PCE in WPT systems revolve around the problem of reducing the ripple present in the output voltage. However, having some amount of ripple may lead to the successful decoding of information by using the same rectifier hardware, resulting in a trade-off between WIT and WPT. One such technique utilizing these ripples is to embed information in the amplitude, known as *M-ary amplitude-shift keying (ASK)*, where the amplitude level of the single tone is changed according to the symbol pattern, with each symbol carrying some minimum energy level [56]. Using this modulation method, a 0.13-V voltage and low BER of 10^{-4} can be achieved for a received input power of -20 dBm. Additionally, this technique ensures minimal continuous power transmission to the receiver, as each symbol is carrying some amount of energy. However, this transmission approach uses only a single tone for generating amplitude variations, which degrades the PCE and does not make use of a high-PAPR multitone signal.

A modulation technique that does use a multitone signal is introduced in [57]. Instead of embedding information directly in the amplitudes of the tones, a model is proposed in which the information is embedded in the ratios of the amplitudes of the different tones rather than in the amplitudes themselves. Although having information in amplitude ratios offers the advantage of making the system independent of transmission distance while providing a 48% PCE for a received signal power of -10 dBm, this technique is suitable only for multitone operations with smaller numbers of tones, as the complete solution of the nonlinear equations is needed for proper information decoding, due to the rectifier's nonlinearity.

Nonetheless, amplitude variations in the multitone waveform have benefits in terms of the data rate (i.e., with the increase of the modulation order) for a SWIPT system, but these variations impose a limit on the achievable WPT, due to the presence of ripples in the output voltage that degrade the WPT performance [56], [57]. An ideal waveform for a SWIPT system would entail minimal variations in the envelope, with the stream of information symbols having a minuscule effect on the WPT. Consequently,

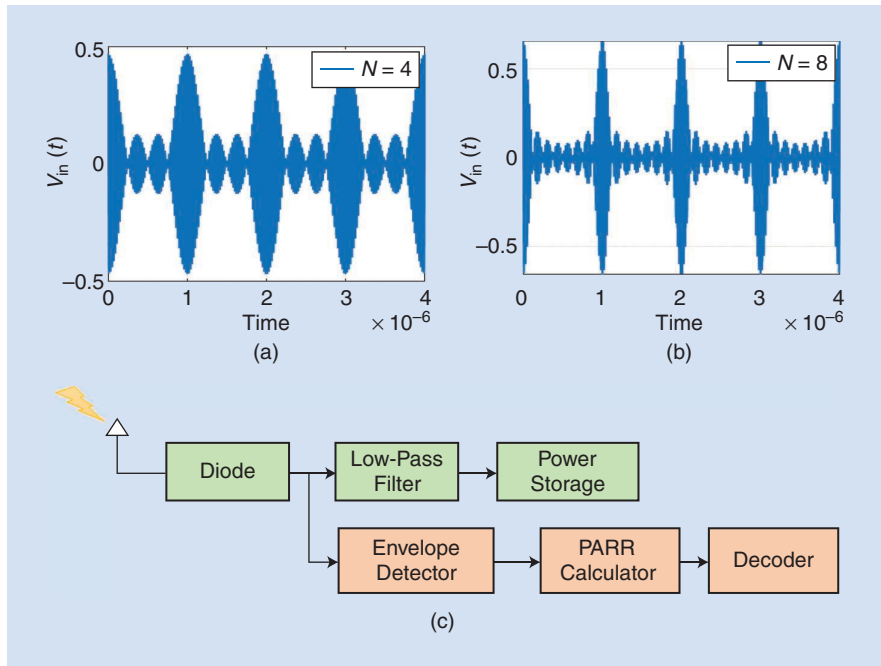


Figure 11. The PAPR-based waveform for (a) $N = 4$ and (b) $N = 8$ and (c) its receiver architecture.

multitone frequency-shift keying (FSK) is proposed to reduce the mutual impact of the WPT and WIT on each other [58]. The signal is designed in such a way that different information symbols correspond to various frequency-spaced multitones at the transmitter (Figure 13). Further, decoding at the receiver can be performed in two ways: either by using the FFT for identifying the strongest baseband signal or evaluating multitone PAPR levels with the changing frequency spacings to lower the power consumption at the receiver [59]. In this way, a 0.55-V output voltage can be attained, which is higher than the amplitude based biased-ASK waveform. However, the SER performance degrades to 10^{-2} compared to 10^{-4} for biased ASK.

To further increase the data transmission capacity of the integrated receiver architecture, a design using two half-wave rectifiers instead of one rectifier was introduced in

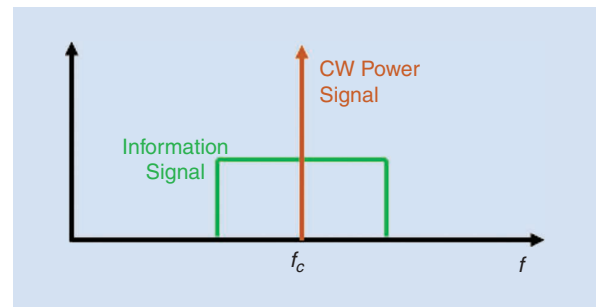


Figure 12. The frequency spectrum of an unmodulated power signal superimposed on a modulated information signal. CW: continuous waveform.

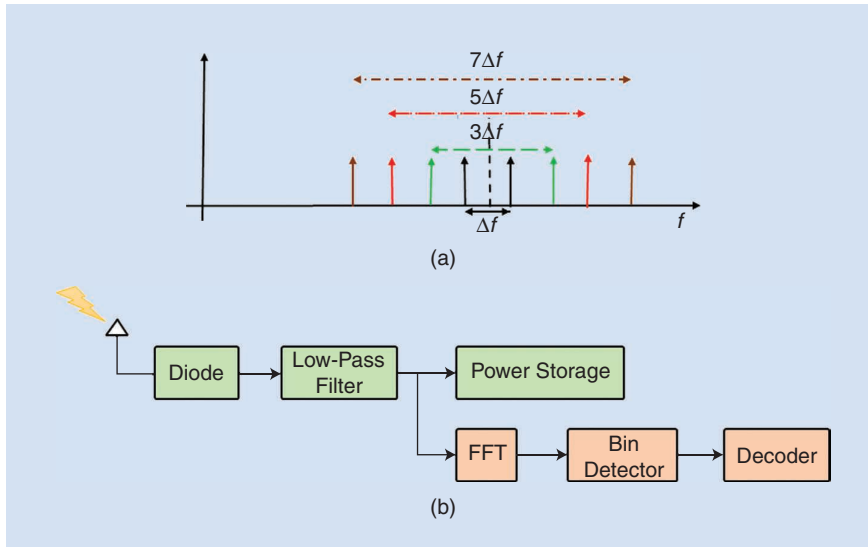


Figure 13. The (a) multitone FSK waveform and (b) receiver architecture [58].

[60]. Two half-wave rectifiers are utilized with two amplitudes, one positive and one negative, at the output. Different combinations of these two voltage levels, amplitude difference-shift keying (ADSK) and amplitude ratio-shift keying (ARSK), are realized to increase the available constellation range for the symbols. In short, the allowable modulation order is increased while keeping the same system noise margin, with the help of modification in the receiver architecture. However, the performance is analyzed without taking into consideration the ripples in the dc voltage, which is not a practical scenario while encoding information in the amplitudes.

The various advantages, disadvantages, and performance of the integrated information–energy receiver architecture-based transmission approaches are summarized in Table 4. It can be observed that in most of the transmission approaches and for both the receiver architectures, the PCE is enhanced by giving the transmitted signal a higher PAPR by means of a multitone signal. This is similar to the case of the separated information–energy receiver architecture, where a high-PAPR OFDM signal is used. Indeed, high-PAPR signals offer the advantage of increased power transfer performance.

However, they may saturate the nonlinear amplifier at the transmitter and subsequently degrade the information transfer performance [61]. Therefore, a complete transmitter–receiver system analysis is required to attain the actual PCE and information transfer performance of these SWIPT transmission schemes.

The discussed transmission waveforms and corresponding receiver architectures are still far from practical SWIPT systems. Some of the reasons are 1) OFDM signal waveforms utilizing a separated receiver architecture consume significant power for signal processing at the receiver; 2) the effect of WIT over WPT is still significant for the modulation methods used for an

TABLE 4. Transmission designs for integrated receiver architecture.

Transmission Approach	Advantages	Disadvantages	Information and Power
PAPR based [51]	<ul style="list-style-type: none"> High PAPR 	<ul style="list-style-type: none"> Performs well only for high SNR Input matching network for a large BW 	0.5 Mb/s and dc 3.5 times higher than the single-carrier input signal for a 30-dB SNR
PAPR based with fixed-signal BW [52]	<ul style="list-style-type: none"> Good performance for high and low SNR 	<ul style="list-style-type: none"> Nonuniform frequency spacings 	0.5 μ A and BER = 10^{-1} for –10-dB input power
Biased ASK [56]	<ul style="list-style-type: none"> Each symbol has some minimum energy 	<ul style="list-style-type: none"> Single tone is used 	10^{-4} BER and 0.13 V at –20-dBm received power for SNR = 18 dB
Amplitude ratio [57]	<ul style="list-style-type: none"> Independent of transmission distance 	<ul style="list-style-type: none"> Analysis only for multitone design with a smaller number of tones 	48% PCE for received power of –10 dBm
Multitone FSK [58]	<ul style="list-style-type: none"> Reduced envelope variations Reduced impact of large WPT on WIT 	<ul style="list-style-type: none"> Power-consuming FFT needed 	SER = 10^{-2} and 0.55 V for received power of 0 dBm
ADSK and ARSK [60]	<ul style="list-style-type: none"> Increased operational range 	<ul style="list-style-type: none"> Only dc power considered 	10^{-1} BER and 0.45 μ W at –10 dBm received power for SNR = 15 dB

integrated information–energy architecture, due to the presence of ripples at the output; 3) moving toward more practical SWIPT systems, the constellation range needs to be increased so that the transmission can support higher modulation orders for increasing information rates, and 4) end-to-end performance analysis, including the transmitter performance, for a particular waveform is required.

Conclusions and Future Outlook

This article discussed beamforming and optimal waveform design to achieve both information and power transfer across the same signal. Distributing antennas contributes to narrower beams, which increases spectral efficiency, resulting in a reduction of interference with neighboring users, which is advantageous from the communications perspective. Additionally, narrow beams avoid wasting power in nonessential areas, resulting in an energy management solution for SWIPT systems. Since it is clear that massive MIMO is evolving toward a widely distributed antenna environment to create cell-free systems, it is necessary to rethink antenna deployment and beam steering procedures, particularly when massive MIMO is to be used for communications and power transfer simultaneously.

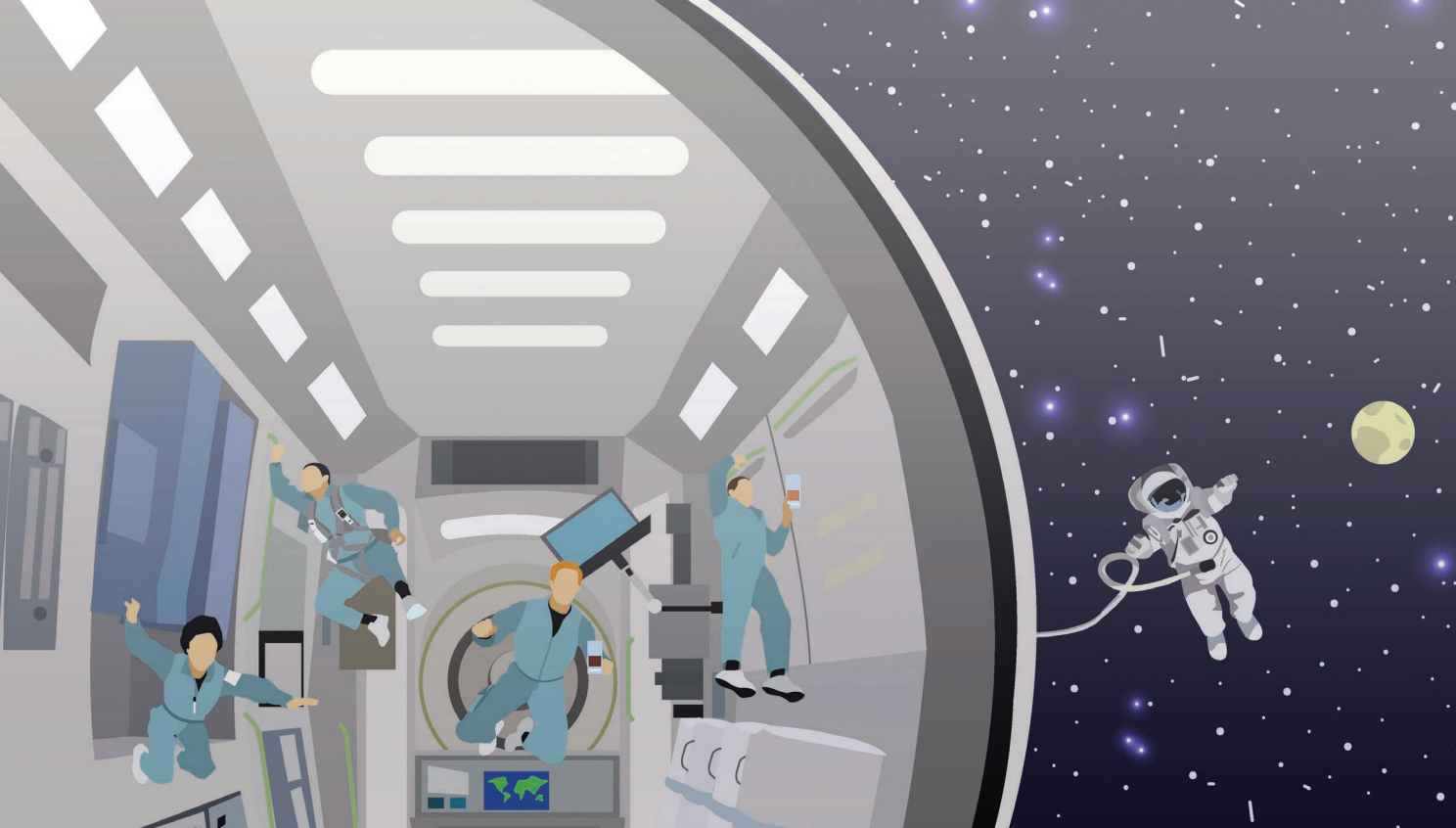
Further, various modulation techniques tailored to separated and integrated information–energy receiver architectures were discussed. This showed that a tradeoff exists between the information transfer rate and harvested power for both the considered receiver architectures. These modulation approaches should be further investigated, considering more practical and time-varying scenarios. For example, an IoT node may not need to receive information and power continuously. Therefore, it will be necessary to optimize these modulation protocols to account for the actual needs of each IoT device at a particular point in time. In fact, it may be possible that the data rate is a critical requirement for only a few types of UE, whereas charging is urgently needed for other UE devices. These respective needs for power and information are likely to vary through time. In conclusion, it may be expected that these studies will result in novel waveform standardization efforts, which is essential for the actual deployment of SWIPT in IoT networks.

References

- [1] "Cisco Annual Internet Report (2018–2023), Cisco, White Paper." <https://www.cisco.com/c/en/us/solutions/collateral/executive-perspectives/annual-internet-report/white-paper-c11-741490.html> (accessed Jun. 27, 2021).
- [2] I. Zhou *et al.*, "Internet of Things 2.0: Concepts, applications, and future directions," *IEEE Access*, vol. 9, pp. 70,961–71,012, May 2021, doi: 10.1109/ACCESS.2021.3078549.
- [3] Z. Popovic, "Far-field wireless power delivery and power management for low-power sensors," in *Proc. IEEE Wireless Power Transfer (WPT)*, 2013, pp. 1–4, doi: 10.1109/WPT.2013.6556867.
- [4] Y. J. Guo and R. W. Ziolkowski, *Advanced Antenna Array Engineering for 6G and Beyond Wireless Communications*. Hoboken, NJ, USA: Wiley, 2021.
- [5] Z. Xiang and M. Tao, "Robust beamforming for wireless information and power transmission," *IEEE Wireless Commun. Lett.*, vol. 1, no. 4, pp. 372–375, 2012, doi: 10.1109/WCL.2012.053112.120212.
- [6] J. Xu, L. Liu, and R. Zhang, "Multiuser MISO beamforming for simultaneous wireless information and power transfer," *IEEE Trans. Signal Process.*, vol. 62, no. 18, pp. 4798–4810, 2014, doi: 10.1109/TSP.2014.2340817.
- [7] R. Feng, M. Dai, and H. Wang, "Distributed beamforming in MISO SWIPT system," *IEEE Trans. Veh. Technol.*, vol. 66, no. 6, pp. 5440–5445, 2017, doi: 10.1109/TVT.2016.2616420.
- [8] R. Zhang and C. K. Ho, "MIMO broadcasting for simultaneous wireless information and power transfer," *IEEE Trans. Wireless Commun.*, vol. 12, no. 5, pp. 1989–2001, 2013, doi: 10.1109/TWC.2013.031813.120224.
- [9] X. Zhou, R. Zhang, and C. K. Ho, "Wireless information and power transfer: Architecture design and rate-energy tradeoff," *IEEE Trans. Commun.*, vol. 61, no. 11, pp. 4754–4767, Nov. 2013, doi: 10.1109/TCOMM.2013.13.120855.
- [10] A. S. Boaventura and N. B. Carvalho, "Maximizing DC power in energy harvesting circuits using multisine excitation," in *Proc. IEEE MTT-S Int. Microw. Symp.*, Jun. 2011, pp. 1–4, doi: 10.1109/MWSYM.2011.5972612.
- [11] L. Yang, Y. Zeng, and R. Zhang, "Wireless power transfer with hybrid beamforming: How many RF chains do we need?" *IEEE Trans. Wireless Commun.*, vol. 17, no. 10, pp. 6972–6984, 2018, doi: 10.1109/TWC.2018.2865313.
- [12] Y. J. Guo, M. Ansari, and N. J. G. Fonseca, "Circuit type multiple beamforming networks for antenna arrays in 5G and 6G terrestrial and non-terrestrial networks," *IEEE J. Microw.*, vol. 1, no. 3, pp. 704–722, 2021, doi: 10.1109/JMW.2021.3072873.
- [13] Y. J. Guo, M. Ansari, W. Z. Richard, and J. G. N. Fonseca, "Quasi-optical multi-beam antenna technologies for B5G and 6G mmWave and THz networks: A review," *IEEE Open J. Antennas Propag.*, vol. 2, pp. 807–830, Jun. 2021, doi: 10.1109/OJAP.2021.3093622.
- [14] J. Butler, "Beam-forming matrix simplifies design of electronically scanned antenna," *Electron. Design*, vol. 9, pp. 170–173, 1961.
- [15] H. Moody, "The systematic design of the butler matrix," *IEEE Trans. Antennas Propag.*, vol. 12, no. 6, pp. 786–788, 1964, doi: 10.1109/TAP.1964.1138319.
- [16] S. Stein, "On cross coupling in multiple-beam antennas," *IRE Trans. Antennas Propagation*, vol. 10, no. 5, pp. 548–557, 1962, doi: 10.1109/TAP.1962.1137917.
- [17] W. Kahn and H. Kurss, "The uniqueness of the lossless feed network for a multibeam array," *IRE Trans. Antennas Propag.*, vol. 10, no. 1, pp. 100–101, 1962, doi: 10.1109/TAP.1962.1137823.
- [18] C.-H. Tseng, C.-J. Chen, and T.-H. Chu, "A low-cost 60-GHz switched-beam patch antenna array with Butler matrix network," *IEEE Antennas Wireless Propag. Lett.*, vol. 7, pp. 432–435, Jul. 2008, doi: 10.1109/LAWP.2008.2001849.
- [19] M. Ansari, H. Zhu, N. Shariati, and Y. Guo, "Compact planar beamforming array with endfire radiating elements for 5G applications," *IEEE Trans. Antennas Propag.*, vol. 67, no. 11, pp. 6859–6869, Nov. 2019, doi: 10.1109/TAP.2019.2925179.
- [20] A. Bekasiewicz and S. Kozieł, "Compact 4×4 butler matrix with non-standard phase differences for IoT applications," *Electron. Lett.*, vol. 57, no. 10, pp. 387–389, 2021, doi: 10.1049/el12.12143.
- [21] J. Nolen, "Synthesis of multiple beam networks for arbitrary illuminations," Ph.D. Diss., Radio Division, Bendix Corp., Baltimore, MD, USA, Apr. 1965.
- [22] P. Li, H. Ren, and B. Arigong, "A symmetric beam-phased array fed by a Nolen matrix using 180° couplers," *IEEE Microw. Wireless Compon. Lett.*, vol. 30, no. 4, pp. 387–390, Apr. 2020, doi: 10.1109/LMWC.2020.2972728.
- [23] T. Djerafi, N. J. Fonseca, and K. Wu, "Broadband substrate integrated waveguide 4×4 Nolen matrix based on coupler delay compensation," *IEEE Trans. Microw. Theory Techn.*, vol. 59, no. 7, pp. 1740–1745, May 2011, doi: 10.1109/TMTT.2011.2142320.
- [24] W. Lin and R. W. Ziolkowski, "Theoretical analysis of beam-steerable, broadside-radiating Huygens dipole antenna arrays and experimental verification of an ultrathin prototype for wirelessly

- powered IoT applications," *IEEE Open J. Antennas Propag.*, vol. 2, pp. 954–967, Sep. 2021. doi: 10.1109/OJAP.2021.3111834.
- [25] C.-M. Chen, A. P. Guevara, and S. Pollin, "Scaling up distributed massive MIMO: Why and how," in *Proc. Asilomar Conf. Signals, Syst. Comput.*, 2017, pp. 271–276.
- [26] A. P. Guevara, S. D. Bast, and S. Pollin, "Massive MIMO: A measurement-based analysis of MR power distribution," in *Proc. IEEE Global Commun. Conf. (GLOBECOM)*, 2020, pp. 1–6, doi: 10.1109/GLOBECOM42002.2020.9322283.
- [27] T. Lo, "Maximum ratio transmission," *IEEE Trans. Commun.*, vol. 47, no. 10, pp. 1458–1461, 1999, doi: 10.1109/26.795811.
- [28] Q. H. Spencer, A. L. Swindlehurst, and M. Haardt, "Zero-forcing methods for downlink spatial multiplexing in multiuser MIMO channels," *IEEE Trans. Signal Process.*, vol. 52, no. 2, pp. 461–471, Feb. 2004, doi: 10.1109/TSP.2003.821107.
- [29] E. Björnson, J. Hoydis, and L. Sanguinetti, "Massive MIMO networks: Spectral, energy, and hardware efficiency," *Found. Trends Signal Process.*, vol. 11, no. 3–4, pp. 154–655, 2017, doi: 10.1561/20000000093.
- [30] X. Li, E. Björnson, E. G. Larsson, S. Zhou, and J. Wang, "Massive MIMO with multi-cell MMSE processing: Exploiting all pilots for interference suppression," *EURASIP J. Wireless Commun. Netw.*, vol. 2017, no. 1, p. 117, Jun. 2017, doi: 10.1186/s13638-017-0879-2.
- [31] S. Claessens, C.-M. Chen, D. Schreurs, and S. Pollin, "Massive MIMO for SWIPT: A measurement-based study of precoding," in *Proc. IEEE Int. Workshop on Signal Process. Adv. Wireless Commun. (SPAWC)*, 2018, pp. 1–5, doi: 10.1109/SPAWC.2018.8445772.
- [32] S. D. Bast, A. P. Guevara, and S. Pollin, "CSI-based positioning in massive MIMO systems using convolutional neural networks," in *Proc. IEEE Veh. Technol. Conf. (VTC2020-Spring)*, 2020, pp. 1–5, doi: 10.1109/VTC2020-Spring48590.2020.9129126.
- [33] A. P. Guevara, S. D. Bast, and S. Pollin, "Weave and conquer: A measurement-based analysis of dense antenna deployments," in *Proc. IEEE Int. Conf. Commun. (ICC)*, 2021, pp. 1–6, doi: 10.1109/ICC42927.2021.9500612.
- [34] A. P. Guevara, S. D. Bast, and S. Pollin, "MaMIMO user grouping strategies: How much does it matter?" in *Proc. Asilomar Conf. Signals, Syst., Comput.*, 2019, pp. 853–857.
- [35] A. P. Guevara and S. Pollin, "Densely deployed indoor massive MIMO experiment: From small cells to spectrum sharing to cooperation," *Sensors*, vol. 21, no. 13, p. 4346, 2021, doi: 10.3390/s21134346.
- [36] A. Costanzo, D. Masotti, G. Paolini, and D. Schreurs, "Evolution of SWIPT for the IoT world: Near- and far-field solutions for simultaneous wireless information and power transfer," *IEEE Microw. Mag.*, vol. 22, no. 12, pp. 48–59, 2021, doi: 10.1109/MMM.2021.3109554.
- [37] C. Lo, Y. Yang, C. Tsai, C. Lee, and C. Yang, "Novel wireless impulsive power transmission to enhance the conversion efficiency for low input power," in *Proc. IEEE MTT-S Int. Microw. Workshop Series. Innovative Wireless Power Transmission: Technologies, Syst., Appl.*, May 2011, pp. 55–58, doi: 10.1109/IMWS.2011.5877090.
- [38] N. Shariati, J. R. Scott, D. Schreurs, and K. Ghorbani, "Multitone excitation analysis in RF energy harvesters—Considerations and limitations," *IEEE Internet Things J.*, vol. 5, no. 4, pp. 2804–2816, 2018. doi: 10.1109/JIOT.2018.2828978.
- [39] N. Pan, D. Belo, M. Rajabi, D. Schreurs, N. B. Carvalho, and S. Pollin, "Bandwidth analysis of RF-DC converters under multisine excitation," *IEEE Trans. Microw. Theory Techn.*, vol. 66, no. 2, pp. 791–802, Feb. 2018, doi: 10.1109/TMTT.2017.2757473.
- [40] N. Shariati, W. S. Rowe, J. R. Scott, and K. Ghorbani, "Multi-service highly sensitive rectifier for enhanced RF energy scavenging," *Sci. Rep.*, vol. 5, no. 1, p. 9655, 2015, doi: 10.1038/srep09655.
- [41] R. Keshavarz and N. Shariati, "Highly sensitive and compact quad-band ambient RF energy harvester," *IEEE Trans. Ind. Electron.*, early access, 2021, doi: 10.1109/TIE.2021.3075888.
- [42] H. Sakaki, S. Yoshida, K. Nishikawa, and S. Kawasaki, "Analysis of rectifier operation with FSK modulated input signal," in *Proc. IEEE Wireless Power Transfer (WPT)*, May 2013, pp. 187–190, doi: 10.1109/WPT.2013.6556914.
- [43] W. Lu, Y. Gong, J. Wu, H. Peng, and J. Hua, "Simultaneous wireless information and power transfer based on joint subcarrier and power allocation in OFDM systems," *IEEE Access*, vol. 5, pp. 2763–2770, 2017. doi: 10.1109/ACCESS.2017.2671903.
- [44] M. Konstantinos, A. Adamis, and P. Constantinou, "Receiver architectures for OFDMA systems with subband carrier allocation," in *Proc. European Wireless Conf.*, 2008, pp. 1–7, doi: 10.1109/EW.2008.4623916.
- [45] B. Clerckx, "Waveform optimization for SWIPT with nonlinear energy harvester modeling," in *Proc. Int. ITG Workshop on Smart Antennas (WSA)*, Mar. 2016, pp. 1–5.
- [46] H. Kassab and J. Louveaux, "Simultaneous wireless information and power transfer using rectangular pulse and CP-OFDM," in *Proc. IEEE Int. Conf. Commun. (ICC)*, May 2019, pp. 1–6, doi: 10.1109/ICC.2019.8761080.
- [47] R. F. Buckley and R. W. Heath, "System and design for selective OFDM SWIPT transmission," *IEEE Trans. Green Commun. Netw.*, vol. 5, no. 1, pp. 335–347, 2021, doi: 10.1109/TGCN.2020.3047581.
- [48] M. N. Khormuji, B. M. Popović, and A. G. Perotti, "Enabling SWIPT via OFDM-DC," in *Proc. IEEE Wireless Commun. Netw. Conf. (WCNC)*, Apr. 2019, pp. 1–6, doi: 10.1109/WCNC.2019.8886079.
- [49] A. Rajaram, D. N. K. Jayakody, B. Chen, R. Dinis, and S. Affes, "Modulation-based simultaneous wireless information and power transfer," *IEEE Commun. Lett.*, vol. 24, no. 1, pp. 136–140, 2020, doi: 10.1109/LCOMM.2019.2946236.
- [50] E. Bayguzina and B. Clerckx, "Asymmetric modulation design for wireless information and power transfer with nonlinear energy harvesting," *IEEE Trans. Wireless Commun.*, vol. 18, no. 12, pp. 5529–5541, 2019, doi: 10.1109/TWC.2019.2937024.
- [51] D. I. Kim, J. H. Moon, and J. J. Park, "New SWIPT using PAPR: How it works," *IEEE Wireless Commun. Lett.*, vol. 5, no. 6, pp. 672–675, Dec. 2016, doi: 10.1109/LWC.2016.2614665.
- [52] I. Krikidis and C. Psomas, "Tone-index multisine modulation for SWIPT," *IEEE Signal Process. Lett.*, vol. 26, no. 8, pp. 1252–1256, Aug. 2019, doi: 10.1109/LSP.2019.2925586.
- [53] M. Rajabi, N. Pan, S. Pollin, and D. Schreurs, "Impact of multisine excitation design on rectifier performance," in *Proc. 46th European Microw. Conf. (EuMC)*, 2016, pp. 1151–1154, doi: 10.1109/EuMC.2016.7824552.
- [54] J. J. Park, J. H. Moon, K. Lee, and D. I. Kim, "Dual mode SWIPT: Waveform design and transceiver architecture with adaptive mode switching policy," in *Proc. IEEE Veh. Technol. Conf. (VTC Spring)*, Jun. 2018, pp. 1–5, doi: 10.1109/VTCSpring.2018.8417661.
- [55] K. W. Choi *et al.*, "Simultaneous wireless information and power transfer (SWIPT) for Internet of Things: Novel receiver design and experimental validation," *IEEE Internet Things J.*, vol. 7, no. 4, pp. 2996–3012, 2020, doi: 10.1109/JIOT.2020.2964302.
- [56] S. Claessens, N. Pan, M. Rajabi, D. Schreurs, and S. Pollin, "Enhanced biased ASK modulation performance for SWIPT with AWGN channel and dual-purpose hardware," *IEEE Trans. Microw. Theory Techn.*, vol. 66, no. 7, pp. 3478–3486, Jul. 2018, doi: 10.1109/TMTT.2018.2829515.
- [57] M. Rajabi, N. Pan, S. Claessens, S. Pollin, and D. Schreurs, "Modulation techniques for simultaneous wireless information and power transfer with an integrated rectifier–receiver," *IEEE Trans. Microw. Theory Techn.*, vol. 66, no. 5, pp. 2373–2385, May 2018, doi: 10.1109/TMTT.2018.2811491.
- [58] S. Claessens, N. Pan, D. Schreurs, and S. Pollin, "Multitone FSK modulation for SWIPT," *IEEE Trans. Microw. Theory Techn.*, vol. 67, no. 5, pp. 1665–1674, May 2019, doi: 10.1109/TMTT.2019.2908645.
- [59] T. Ikeuchi and Y. Kawahara, "Peak to average power ratio based signal detection for frequency shift multitone SWIPT system," *IEEE Access*, vol. 9, pp. 4158–4172, Dec. 2020. doi: 10.1109/ACCESS.2020.3048193.
- [60] D. Kim, H. Lee, K. Kim, and J. Lee, "Dual amplitude shift keying with double half-wave rectifier for SWIPT," *IEEE Wireless Commun. Lett.*, vol. 8, no. 4, pp. 1020–1023, Aug. 2019. doi: 10.1109/LWC.2019.2904482.
- [61] J. J. Park, J. H. Moon, H. H. Jang, and D. I. Kim, "Performance analysis of power amplifier nonlinearity on multi-tone SWIPT," *IEEE Wireless Commun. Lett.*, vol. 10, no. 4, pp. 765–769, 2021, doi: 10.1109/LWC.2020.3042852.





©SHUTTERSTOCK.COM/SKYPICIS STUDIO

Space Tags

Space agencies worldwide have a long-term vision of sending human missions to Mars [1]. The next favorable launch window occurs in 2033, and plans are ongoing to realize such endeavors. An essential part of this preparation is the search for new technologies to mitigate mission performance risks. A critical technological advancement is passive or batteryless wireless sensor technology [2], [3], as used in the Internet of Things (IoT) [4], which can be favorably used to continuously monitor the physiological conditions of crew members in the space habitat and structural health of spaceflight equipment.

IoT technologies and deployment have become more widespread and easily accessible in terrestrial environments, and there are already companies using satellites for IoT-based networking applications and wide-area networking [4]. Researchers are now starting to ask questions about how IoT technologies—such as, for example, passive wireless sensor technology—can be seamlessly integrated with existing space-related technologies to create new opportunities for future space exploration and travel [4].

State-of-the-art passive or batteryless wireless sensors have not been made suitable for space environment operation [2], [3]; the main reliability issues still

Jasmin Grosinger and Alicja Michalowska-Forsyth

Jasmin Grosinger (jasmin.grosinger@tugraz.at) is with the Institute of Microwave and Photonic Engineering, Graz University of Technology, Styria, 8010, Austria, and Alicja Michalowska-Forsyth (alicja.michalowska@tugraz.at) is with the Institute of Electronics, Graz University of Technology, Styria, 8010, Austria.

Digital Object Identifier 10.1109/MMM.2021.3130686

Date of current version: 3 February 2022

have to be addressed. These challenges include tight power constraints due to the batteryless operation of sensors, which is also a problem in terrestrial settings, and the harsh space flight environment, which has temperature extremes, vibrations, and—of particular interest in this work—ionizing radiation [3].

Passive wireless IoT sensors typically rely on microchips realized with a low-cost CMOS technology, which do not provide hardness for ionizing radiation (in contrast to other CMOS devices custom-built for radiation environments in terrestrial applications, e.g., nuclear instruments). From a semiconductor materials point of view, CMOS devices based on silicon (Si) material are not as radiation hard as, for example, gallium arsenide (GaAs) devices, for use in space environments. GaAs devices rely on a wide-bandgap material, resulting in resistance to radiation damage. However, CMOS is superior in some significant aspects (see “Comparing GaAs and Si Semiconductor Devices”). In fact, there is no alternative to CMOS in passive wireless sensors because they rely on ultra-low-power integrated circuits (ICs), which are only possible to realize with CMOS.

Thus, this article reviews the existing work on batteryless wireless sensors for their reliable ultra-low-power operation and evaluates perspectives for their radiation hardness. It focuses exclusively on passive wireless sensors exploiting a backscatter RF technology, in particular, the ultra-high frequency (UHF) RF identification (RFID) technology based on the ISO/IEC 18000-6 standard operating in a frequency range of 860–960 MHz, in contrast to previous work on backscatter tags in space operating at higher frequencies [5] and battery-assisted wireless IoT sensor systems in radiation environments [6].

Ultra-Low-Power Operation

One main reliability issue of passive wireless sensors in space is tight power constraints due to the batteryless operation of sensors, which is also an issue in terrestrial environments. Thus, in the following, the article presents a discussion of passive wireless sensors, particularly sensor transponders, and their reliable ultra-low-power operation in harsh RF propagation environments, as in space habitats.

One possibility to realize passive wireless sensors operating without batteries at ultra-low power is to use the passive backscatter RF technology, which exploits far-field wireless power transfer and communication by means of reflected power. Today, the backscatter RF technology is used for inventory procedures on the International Space Station (ISS) [7]. The backscatter RF technology is, in particular, interesting for space applications, as the backscatter RF reader acting as an interrogator is the location of

almost all of the complexity and power consumption of the system. The transponder (tag) requires no wires or power supply. In addition, tags can be added late in the design cycle or even after.

Surface acoustic wave (SAW) tags have been selected for the inventory application on the ISS because they can be reliably detected even when placed on, behind, or between items with high liquid and metal content of randomly packed crew bags [7]. In addition, SAW backscatter RF tags are inherently robust against ionizing radiation since they have no electronics onboard. However, SAW tags have significant limitations in contrast to modern backscatter RF tags equipped with state-of-the-art microchips based on low-cost CMOS technologies [8]. SAW tags provide only a limited tag data capacity due to using hard-coded ID numbers. Also, SAW systems follow no widespread standard.

In contrast, modern backscatter RF tags are based on a fully standardized communication protocol and can manage various tags through anticollision techniques [9]. In addition and contrast to SAW tags, modern tags operate in a very narrow frequency band, thus limiting electromagnetic compatibility concerns. Due to these benefits, in 2006, there were investigations into using chip-based backscatter RF tags for identifying goods in space habitats. However, the reading reliability results in the harsh RF propagation environment of space habitats did not warrant proceeding to an in-orbit test [7].

Backscatter RF Sensor Tags

Since the availability of inexpensive, ultra-low-power ICs in the early 1990s, considerable research and development have been invested in the area of backscatter RF systems for ID purposes, also known as *RFID systems* [10]. Since 2009, researchers have been working consistently toward reaching beyond the ID in RFID [11], [12], i.e., by integrating sensing capabilities in passive RFID tags to additionally monitor the tag environment (e.g., temperature, curvature, and liquid level). The existing literature shows sensor tags realized by integrating additional sensor circuitry that uses a sensor interface and external sensors as well as those realized without additional sensor circuitry, which is of particular interest in this work. The latter type of passive RFID sensor tag integrates passive transducers that change its RF parameters when the tag environment changes. These parameter changes additionally modulate the digitally modulated tag signal in the analog domain detectable at the reader.

Figure 1 shows examples of sensor tags with and without additional sensor circuitry. These backscatter RF sensor tags rely, in particular, on the UHF RFID technology. The UHF RFID magnetic field sensor tag with sensor circuitry consists of a custom-built dipole antenna, an NXP UCODE G2iM+ chip, and a reed

Comparing GaAs and Si Semiconductor Devices

Typical solid-state devices fabricated in a GaAs semiconductor material are light-emitting diodes, high-efficiency solar cells, and high-speed amplifiers. The GaAs devices are particularly favorable for space applications due to their excellent resistance to ionizing radiation. However, CMOS technologies based on a Si semiconductor material are superior in some significant aspects. Key parameters and characteristic features for Si and GaAs semiconductor materials are summarized in Table S1.

Temperature Range

The GaAs bandgap is wider than the Si material's bandgap, thus enabling applications in a broader temperature range. The operation of semiconductor devices relies on defining the conductivity by setting the local doping concentrations (e.g., the n+ regions in Figure S1). All of these doping centers will be ionized already at very low temperatures. However, as the temperature increases, the thermally generated carriers become dominant over carriers originating from ionized dopant atoms. This effect happens at lower temperatures in Si compared to GaAs (see Figure S2). Therefore, the GaAs material can also handle much higher power levels.

Speed

In a metal–semiconductor field-effect transistor (MESFET), a voltage applied to its gate controls the charge carrier density beneath, thus modulating the channel conductivity. GaAs MESFETs are always the n-channel type, meaning that the majority of charge carriers are electrons. GaAs transistor devices, where holes would be the majority carriers (i.e., the p-channel), are not of interest because the mobility of holes in GaAs is 20 times worse than its electron mobility. For the same reason, ultra-high-speed GaAs-based high electron mobility transistors (HEMTs) have electrons as majority charge carriers. The electron mobility in GaAs is five times greater than in Si. Therefore, the charge transit frequency is much higher, making GaAs devices more suitable for higher frequencies. The additional speed benefit comes from a significantly lower gate capacitance in MESFETs, related mainly to the depletion capacitance of the Schottky contact at the gate. In the case of Si CMOS technologies, the thin gate oxide insulator results in a large capacitance, limiting high-speed applications.

TABLE S1. A comparison of Si and GaAs semiconductor materials.

Key Parameters and Characteristic Features	Si	GaAs
Bandgap	Indirect	Direct
Energy bandgap (eV)	1.12	1.43
Intrinsic carrier concentration at 300 K (cm ⁻³)	1.45 ¹⁰	1.79 ⁶
Upper junction temperature (°C)	150	>250
Substrate resistivity at 300 K, undoped (Ωcm)	2.2 ⁵	3.9 ⁸
Radiation hardness, total ionizing dose	Poor due to traps associated with gate oxide	Very resistant (no gate oxide and only blocking the Schottky contact)
Minority carrier lifetime (s)	2.5 ⁻³	10 ⁻⁸
Electron mobility (cm ² /Vs)	1,500	8,500
Hole mobility (cm ² /Vs)	475	400
Devices	p- and n-channel MOSFETs	n-channel MESFET
Gate length (nm)	A few to 100	Few hundreds
Gate leakage current (A/μm ²)	1 ⁻¹⁵ ...1 ¹² (oxide insulator)	1 ⁻⁹ ...1 ⁻⁶ (Schottky barrier)
Gate capacitance (fF/μm ²)	>10	<1
Operating frequencies	Up to gigahertz	Up to tens of gigahertz
Power consumption in digital circuits	Ultra-low-power MOSFET	Power-inefficient MESFET
Wafer diameter (mm)	>300	<200
Wafer cost (before device process)	–	Ten times more

Continued

Comparing GaAs and Si Semiconductor Devices (Continued)

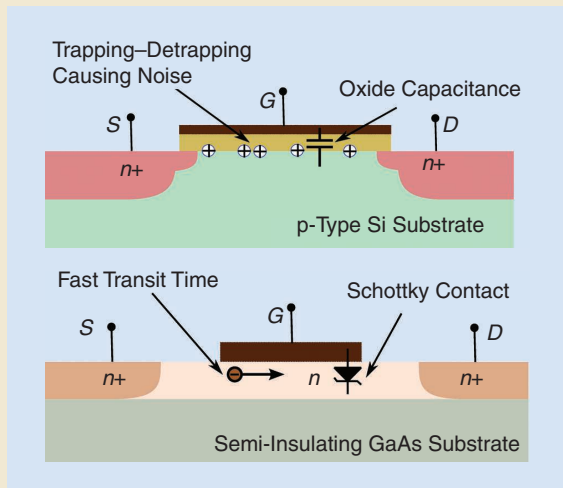


Figure S1. An Si-based n-channel MOSFET cross section (see top figure). During device operation, the ongoing charge trapping and detrapping appear in the device characteristics as low-frequency noise. The few-nanometer-thin insulating oxide at the gate introduces a considerable parasitic capacitance. Complementary p-channel MOSFETs are widely used, as their performance is only two to three times worse in Si (not illustrated). A GaAs-based n-channel MESFET cross section (see bottom figure). Electrons have high mobility, resulting in a short transit time and small parasitics. The blocking metal junction constitutes a Schottky diode, creating a considerable gate leakage current. S: source; G: gate; D: drain.

Low Noise and Radiation Hardness

The Schottky contact instead of the gate oxide results in GaAs MESFETs being more resistant to ionizing radiation [S1] (though at the cost of high leakage current). CMOS transistors suffer from oxide and interface charge trapping that causes low-frequency noise [S2]. The trap density increases after irradiation, degrading noise further and causing shifts in the device characteristics after total ionizing dose stress (with X- or gamma-rays) [S3]. In MESFETs and HEMTs, the noise is generally lower than in Si MOSFETs due to the absence of the gate oxides.

Advancements in GaAs-based monolithic microwave integrated circuits (MMICs) can be observed in response to the benefits mentioned (i.e., the broad temperature range, high speed, and low noise). These processes can integrate MESFETs, HEMTs, and passive devices. More details on GaAs technologies can be found in [S3] and [S4]. There are, however, significant limitations in building ICs featuring high complexity and ultra-low power, as is

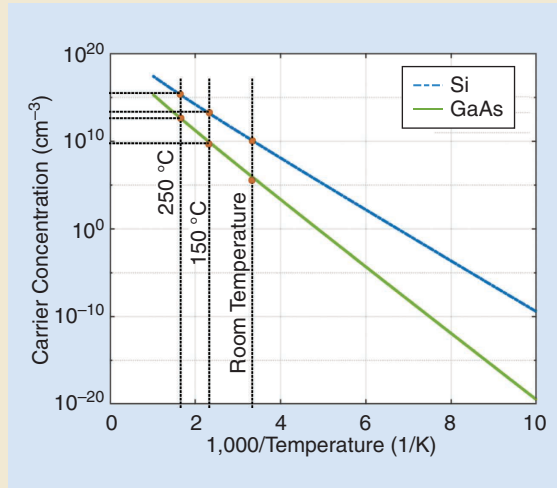


Figure S2. An Arrhenius plot of GaAs and Si materials (thermally generated charge carriers versus temperature). The critical doping levels at the characteristic temperatures are indicated, i.e., room temperature, the upper temperature for Si devices (150 °C), and the upper temperature for GaAs devices (250 °C). Assuming a doping level of 10^{15} , the conductivity of GaAs can still be doping controlled, even at 250 °C.

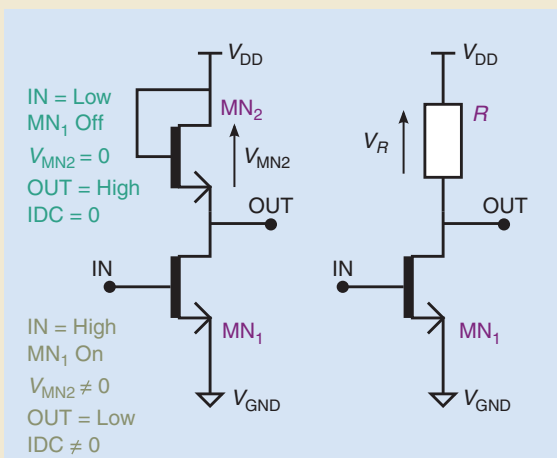


Figure S3. In MESFET inverters, typical for the GaAs monolithic microwave IC process, the current flows through the main branch whenever the output state is low, resulting in poor power efficiency. GND: ground; M: transistor; IDC: direct current (between V_{DD} and V_{GND}).

possible in Si CMOS ICs. Without complementary transistors—the p- and n-types, like in CMOS—GaAs circuits are very power inefficient. It is impossible to build a logic gate like the Si CMOS inverter with a near-zero. As illustrated in Figure S3, a logic gate

Continued

Comparing GaAs and Si Semiconductor Devices (Continued)

based on MESFETs has a resistor or diode load on the high side instead of the p-channel transistor in CMOS [S5], [S6]. Thus, with the output state low, inevitably, there is a nonzero through the logic branch. Without the possibility of CMOS integration, GaAs material is still power inefficient. It does not enable low-power and high-complexity digital circuits and large-density memories. For this reason, in low-cost and ultra-low-power wireless sensors, including passive RFID devices, Si CMOS-compatible processes are the only attractive option.

References

[S1] C. Barnes and L. Selva, "Radiation effects in MMIC devices," in *GaAs MMIC Reliability Assurance Guideline for Space*

Applications, R. Kayali, S. Ponchak, and G. Shaw, Eds. Pasadena, CA, USA: JPL Publication, 1996, pp. 203–243.

[S2] S. Sze, Y. Li, and K. Ng, *Physics of Semiconductor Devices*. Hoboken, NJ, USA: Wiley, 2021.

[S3] R. Leon, *Radio Frequency Technologies in Space Applications*. Pasadena, CA, USA: JPL Publication, 2010.

[S4] C. Chang and F. Kai, *GaAs High-Speed Devices: Physics, Technology, and Circuit Applications*. Hoboken, NJ, USA: Wiley, 1994.

[S5] A. Bentini, B. Pasciuto, W. Ciccognani, E. Limiti, A. Nanni, and P. Romanini, "Design and realization of GaAs digital circuit for mixed signal MMIC implementation in AESA applications," *Int. J. Microw. Sci. Technol.*, vol. 2011, pp. 1–11, 2011, doi: 10.1155/2011/387137.

[S6] C. Ramella et al., "Low power GaAs digital and analog functionalities for microwave signal conditioning in AESA systems," in *Proc. Int. Workshop on Integrated Nonlinear Microw. Millimetre-Wave Circuits (INMMiC)*, 2020, pp. 1–3, doi: 10.1109/INMMiC46721.2020.9160147.

switch to monitor the open or close status of a valve with a magnet attached to it [13]. The one without additional sensor circuitry uses the antenna as a sensing device and consists of a custom-built dipole antenna and an NXP UCODE 7 chip to monitor a water canister's full or empty status [14], [15].

Today, backscatter RF tags are widely referred to as *UHF RFID tags* and mainly used in logistics and maintenance for ID purposes [12], [17]. Backscatter RF tags consisting of an antenna and a chip communicate wirelessly with an interrogator that reads the tag ID number. While the reader transmits the RF power and data toward the passive tags, each tag transmits its ID number to the reader using a modulated backscatter signal [18], which is realized by modulating the reflected signal (or, rather, the backscattered reader signal) at the chip input by controlling the respective impedances of the tag antenna Z_{ant} and those of the tag chip Z_{abs} and Z_{ref} (see Figure 2). A cost-effective and ultra-low-power approach to integrating a passive transducer into an RFID tag uses the tag antenna as the sensing device. One significant benefit of

antenna-based sensing is that the sensor tag can still rely on off-the-shelf RFID tag chips and does not need an additional sensor device as, for example, a reed or bimetal switch, as shown in Figure 1.

Figure 2 shows the concept of an antenna-based UHF RFID sensor tag [19]. The antenna impedance

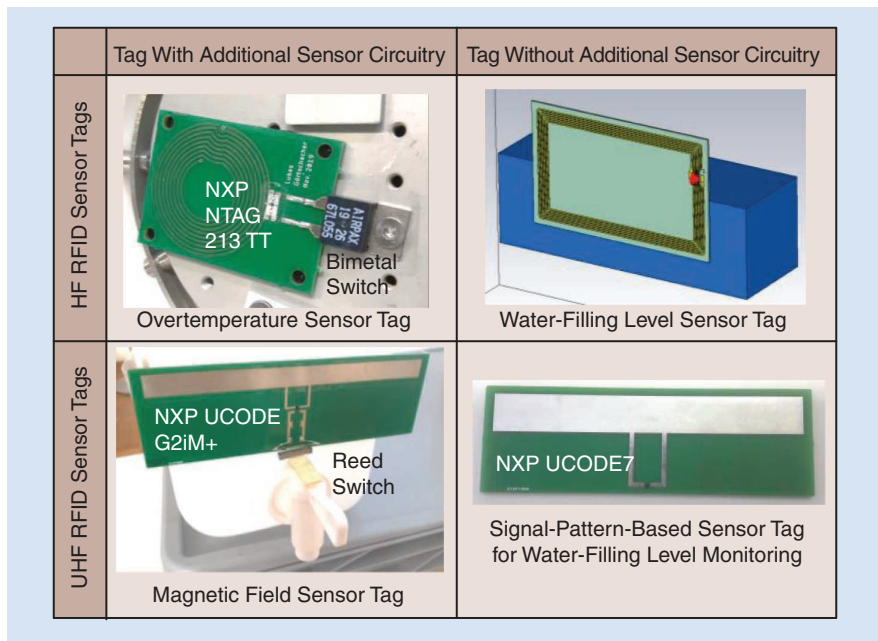


Figure 1. An overview of current RFID sensor tags. For completeness, the image also shows sensor tags based on the HF RFID technology using load modulation in near-field inductive coupling links [10]. The overtemperature sensor tag with additional sensor circuitry consists of a custom-built ferrite-backed coil antenna, an NXP NTAG 213 TT, and a bimetal switch to monitor the overtemperature of automotive battery packs. The shown electromagnetic simulation model of an HF RFID sensor tag without additional sensor circuitry consists of a sensing coil antenna and an HF RFID tag chip [16] to monitor water-filling levels in a canister.

Z_{ant} , chip impedance in the absorbing mode Z_{abs} , and chip impedance in the reflecting mode Z_{ref} characterize the tag antenna and chip. In state-of-the-art UHF RFID tags, the tag modulates the amplitude of the backscattered tag signal, communicating its ID using on-off keying modulation, switching between the chip impedances Z_{abs} and Z_{ref} . The reflected tag signal at the chip input relates to the reflection coefficient in the absorbing mode S_{abs} (representing a logical “zero”) and that in the reflecting mode S_{ref} (representing a logical “one”), defined by the respective antenna and chip impedances.

The reflection coefficients S_{abs} and S_{ref} can be plotted in a tag signal response diagram to analyze the tag performance, as shown in Figures 3 (see the state-of-the-art modulation) and 4. The tag performance parameters, i.e., the power transmission coefficient τ and modulation efficiency η , can be calculated based on the reflection coefficients S_{abs} and S_{ref} . In the case of antenna-based sensing, as illustrated in Figure 2, the antenna impedance $Z_{ant}(\psi)$ changes with sensing state ψ , leading to a change of the scattering parameters $S_{abs}(\psi)$ and $S_{ref}(\psi)$ as well as performance parameters $\tau(\psi)$ and $\eta(\psi)$.

Sensor Tag Prototypes

Table 1 lists chronologically by publication date the antenna-based sensor tag prototypes presented in the literature. The prototypes use different analog

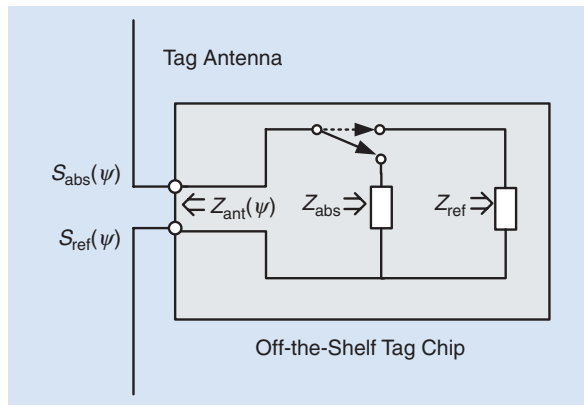


Figure 2. The antenna-based UHF RFID sensor tag changes its parameters with sensing state ψ , additionally modulating the digitally modulated tag signal in the analog domain detectable at the reader. The tag performance parameters τ and η can be calculated based on the tag reflection coefficients S_{abs} and S_{ref} . The power transmission coefficient $\tau = 1 - |S_{abs}|^2$ is a quality measure of the wireless power transfer toward the passive tag chip [18]: $\tau \in [0, 1]$ ($\tau = 1$ for ideally amplitude-modulated backscatter signals). The modulation efficiency $\eta = \alpha |S_{abs} - S_{ref}|^2$ is a measure of the modulation quality of the reflected tag signal [20]: $\eta \in [0, 1]$ and $\alpha = 0.25$, assuming a duty cycle of 50% [20] ($\eta = 0.25$ for ideally amplitude-modulated backscatter signals).

modulation concepts to enable antenna-based sensing and high sensor system performance. The UHF RFID sensor system performance is affected by two significant factors. On the one hand, the system performance degrades due to a nonsufficiently high wireless power transfer toward the batteryless tag chip, i.e., τ gets smaller than one. On the other hand, it degrades due to a system setup dependence of the detected sensor data and, thus, on the wireless channel. Table 1 lists the presented prototypes, their sensing parameters, the exploited analog modulation concept, and its effect on the system performance.

As indicated in Table 1, the initial prototypes from 2009 use amplitude modulation to communicate the sensor states. However, this modulation type often leads to variations in the wireless power transfer toward the passive tag chip and, thus, severe impairments in system performance. Therefore, in 2013, researchers started to control these variations in wireless power transfer by introducing constraints into the antenna design of the sensor tag [27], ensuring a sufficiently high τ .

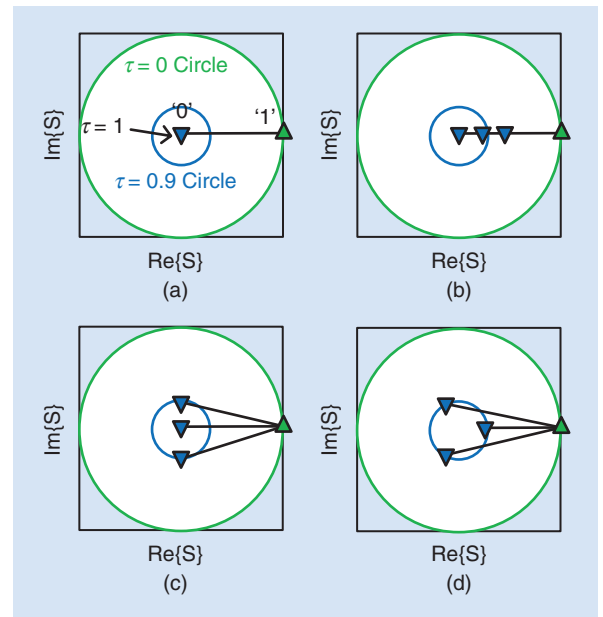


Figure 3. The tag response diagrams of (a) a state-of-the-art tag [14] and different sensor tags: (b) amplitude, (c) phase, and (d) amplitude and phase modulations. The state-of-the-art tag modulates the amplitude of the backscattered tag signal or, rather, tag reflection coefficient S , communicating its ID by switching between the chip impedances Z_{abs} and Z_{ref} . Concerning the sensor tags, the figure shows, in a simplified way, the different analog modulation concepts used for sensor tags (i.e., amplitude, phase, and amplitude and phase) in the case of monitoring three discrete sensor states. A power transfer coefficient of $\tau \geq 0.9$ is assumed to be sufficiently high in this case. The more τ deviates from one or the closer τ gets to zero, the smaller the wireless power transfer becomes.

However, further research presented in 2014 and 2015 shows that pure phase modulation [28] or a combination of amplitude and phase modulation [19] achieves a considerably better system performance than pure amplitude modulation, as both modulation concepts inherently guarantee a high wireless power transfer. In 2016, researchers started to exploit off-the-shelf RFID tag chips that offer self-tuning capabilities [30], [31], ultimately also ensuring a constant wireless power transfer in the case of pure amplitude modulation. Figure 3 shows in a simplified way the different analog modulation concepts (amplitude, phase, and amplitude and phase) and their impacts on wireless power transfer.

In addition to the need to provide a sufficiently high wireless power transfer, another issue associated with most of the system prototypes presented so far is that they do not offer setup independence. Each time the reader-to-tag distance or wireless channel changes, the systems need to be recalibrated; this is inconvenient in practical applications. In 2009, an analog identifier [21] solved the issue early on for amplitude-modulated systems (see Table 1). However, systems that exploit phase modulation and self-tuning capabilities of tag chips (in the nonlinear regime [30]) still suffer from this. The use of multiport tags solves the problem regarding phase-modulated sensor tags [32], but with an increased cost and size of the tags.

Finally, in 2018, a novel UHF RFID sensor system prototype was presented based on a combination of amplitude- and phase-modulated sensor tag signals.

The system relies on tag signal patterns to communicate the sensor state, i.e., a specific tag signal pattern relates to a set of discrete sensor states, enabling, e.g., binary sensing, as illustrated in Figure 4. This differs from the previously mentioned systems in which one specific tag signal is related to one discrete sensor state. As a result, the system offers both constantly high wireless power transfer and setup independence [14], [15].

The sensor system in Figure 4 monitors the water-filling level, i.e., if the canister is full or empty, providing a sufficiently high wireless power transfer toward the tag chip, $\tau(\psi) \geq 0.9 \forall \psi$, by an optimized antenna design and setup independence using a tag signal pattern for sensing. Figure 4(a) shows the electromagnetic simulation model of the sensing scenario [14]. The sensor tag antenna is attached vertically on a plastic sheet modeling the water canister. The tag chip is attached to the antenna port. The water-filling levels change from $\psi_{\text{start}} = 0$ mm to $\psi_{\text{mid}} = 50$ mm and $\psi_{\text{stop}} = 100$ mm in 10-mm steps. The operating frequency is 915 MHz. Figure 4(b) shows a schematic of the simulated tag response diagram versus sensor state $\psi \in [\psi_{\text{start}}, \psi_{\text{stop}}]$ [14]. The corresponding tag reflection coefficients in the reflecting mode $S_{\text{ref}}(\psi)$ lie on the $\tau = 0$ circle, inherently leading to a high modulation efficiency.

Figure 4(c) shows a schematic of the measured signal constellation diagram of the sensor tag prototype at the reader receiver baseband [14]. The signal pattern used for sensing shows a very distinctive pattern for water-filling levels between $\psi_{\text{start}} = 0$ mm and $\psi_{\text{mid}} = 50$ mm,

TABLE 1. A summary of passive antenna-based RFID sensor tag prototypes (listed chronologically by publication date).

Year	References	Sensing Parameters	Analog Modulation	High Wireless Power Transfer	Setup Independence
2009	[11]	Temperature, filling level, displacement, and anemia	Amplitude	No	No
2009	[21] and [22]	Filling level, displacement, strain, humidity, gas, and restenosis	Amplitude	No	Yes (analog identifier)
2010	[23] and [24]	Temperature, filling level, strain, and humidity	Amplitude	No	No
2011	[25]	Temperature	Amplitude	No	No
2011	[26]	Strain and crack	Amplitude	No	No
2013	[27]	Filling level	Amplitude	Yes	Yes (analog identifier)
2014	[19]	Filling level and curvature	Amplitude and phase	Yes	No
2015	[28]	Humidity	Phase	Yes	No
2016	[29]	Corrosion	Amplitude	No	Yes (analog identifier)
2016	[30]	Filling level	Amplitude	Yes (self-tuning chip)	No
2018	[31]	Temperature	Amplitude	Yes (self-tuning chip)	No
2018	[14] and [15]	Filling level	Amplitude and phase	Yes	Yes

This literature review does not include articles on chipless tags and tag grids (i.e., including reference tags and multiport/multichip tags). The table lists the representative publications of each research group.

making it possible to detect whether the water canister will soon be empty by detecting this unique pattern at the reader receiver. The two shown tag signal patterns are related to two different reader-to-tag distances. The two patterns are scaled and rotated to each other, following the fact that the backscattered tag signal decreases with an increasing reader-to-tag distance and experiences a different phase shift due to the change in distance. Although the tag signals experience variations, the distinctive tag signal pattern can still be detected, making frequent sensor system calibrations unnecessary.

Harsh RF Propagation Environment

Space habitats are full of randomly packed items, which may frequently include high liquid and metal contents [7]. In addition, both crew members and equipment move while they are being monitored. Due to these facts, space habitats provide a harsh RF operation environment for passive wireless sensors [2], [3] and, in particular, UHF RFID sensor systems. This might cause a high attenuation of the wireless signal, eventually leading to a forward-link limitation of the backscatter system and system outages [18].

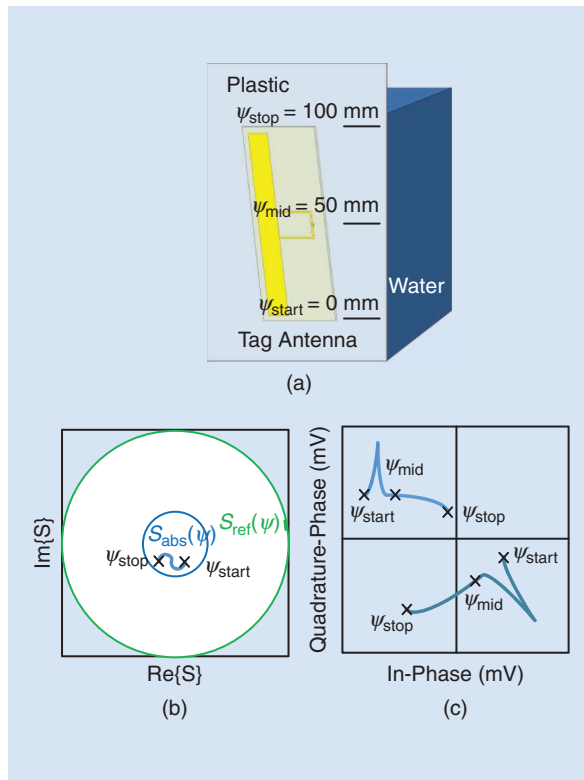


Figure 4. A schematic of the prototype system for signal-pattern-based sensing [14], illustrating the (a) electromagnetic simulation model, (b) tag response diagram (see Figure 3), and (c) signal constellation diagram of the detected tag signal at the reader receiver baseband.

Also, the propagation environment leads to multipath propagation, eventually causing a distorted sensor signal detection.

A further analysis of signal-pattern-based sensor systems shows, to a certain extent, the system's ability to operate robustly under these severe conditions. Figure 5(a) shows the simulated signal constellation

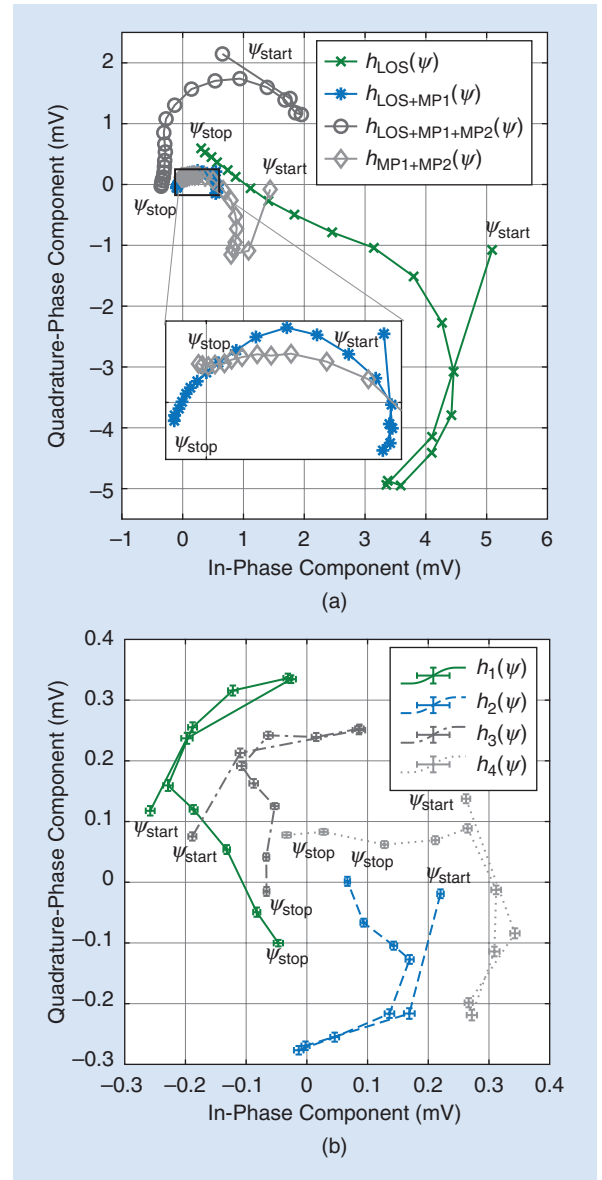


Figure 5. The simulated and measured signal constellation diagrams of signal-pattern-based sensor tag signals at the reader receiver baseband [14]. (a) Four exemplary tag signal patterns related to different variations of the multipath propagation environment [33], i.e., $h_{\text{LOS}}(\psi)$; $h_{\text{LOS}+\text{MP1}}(\psi)$, including the NLOS path due to ground reflection; $h_{\text{LOS}+\text{MP1}+\text{MP2}}(\psi)$, including both NLOS paths; and $h_{\text{MP1}+\text{MP2}}(\psi)$, accounting for a blocked LOS component. (b) An Impinj Speedway R420 reader was used in the measurement campaign operating at 867.5 MHz [15].

diagram of signal-pattern-based sensor tag signals [14] at the receiver baseband in a multipath environment corresponding to the environment presented in [33]. The wireless channel is described by a deterministic multi-ray model, assuming one line-of-sight (LOS) path and two non-LOS (NLOS) paths, arising from ground and wall reflections. The reader receiver can correctly detect the tag signal patterns in a varying multipath propagation environment.

Figure 5(b) shows the measured signal constellation diagram of signal-pattern-based sensor tag signals presented in [15]. The measurements were conducted in a student laboratory, which represents a moderate multipath environment. The four exemplary tag signal patterns relate to four variations of the multipath environment, allowing a correct detection of the sensing state.

In a space habitat, it might happen that the reader–tag–reader communication channel is not stable versus the whole sensing cycle (i.e., from ψ_{start} to ψ_{stop}). If there are abrupt changes of the wireless channel within one sensing cycle, the signal pattern will split up into artifacts. The reader receiver can still detect these artifacts using the different tag IDs and reassemble them, resulting in the correct sensor state detection.

Summing up the discussion on passive wireless sensors in space and their reliable ultra-low-power operation, the recent development of modern backscatter RF tags might warrant proceeding to revisit the use of these devices in space habitats. Modern backscatter RF tags, i.e., UHF RFID tags, provide a fully standardized communication protocol and anticollision techniques. In addition, the performance of tag chip front ends has been improved constantly, in terms of tag sensitivity, from -10 dBm [34] to -20 dBm [18], relieving the system's power budget considerably. Last but not least, the addition of passive sensing capabilities to backscatter RF tags brings additional functionality without impacting the power budget at all. Finally, researchers are constantly working on improving the reliable operation of sensors tags [35]. However, further investigations must be done to prove reading reliability in harsh space habitat environments.

Radiation Hardness

One of the other main reliability issues of passive wireless sensors in space is radiation hardness for ionizing radiation. Thus, in the following, the article presents a discussion of modern backscatter UHF RFID tags based on CMOS chips and evaluates perspectives for their radiation hardness. The effects of ionizing radiation have to be investigated for the UHF RFID chip and its ICs, as the ionizing radiation in space affects the

A further analysis of signal-pattern-based sensor systems shows, to a certain extent, the system's ability to operate robustly under these severe conditions.

functionality of semiconductor devices (see "Ionizing Radiation Effects in Semiconductor Devices").

Passive Tag Chips

Figure 6 illustrates the block diagram of an exemplary differential RF front end of a custom-built UHF RFID tag chip in a 40-nm CMOS technology [18], [36]. The RF terminals RF_1 and RF_2 of the front end are directly connected to the tag antenna. Two pairs of antiparallel diodes form an electrostatic discharge (ESD) protection, which shields the chip front end from overvoltages at high levels of chip input power. An RF charge pump, also known as an *RF-to-dc power converter*, rectifies the RF signal received at the antenna, multiplies it, and converts it into a dc voltage V_{dc} for the chip power supply. A dc limiter regulates V_{dc} to prevent overvoltages from affecting the chip circuitry [18].

The modulator of the tag chip is composed of typical shunt transistors to switch the RF input to a low impedance state, i.e., Z_{Ref} , modulating the reflected tag signal for backscatter communication (see Figure 2). In addition to ESD protection, a dedicated RF limiter is used to regulate the RF input voltage at the chip [37]. The chip uses an envelope detector to demodulate the amplitude-modulated signal transmitted by the reader [10]. The modulator control signal Data_{TX} and the demodulator output signal Data_{RX} are connected to a digital control circuit, which handles the communication protocol and access to nonvolatile memory. The tag ID is typically contained in only a few hundred bits stored in a nonvolatile on-chip electrically erasable programmable read-only memory (EEPROM), characterized by excellent retention of the stored data for a long time and without the necessity of a power supply.

In the following, it is worth focusing on the RF charge pump, as only its careful design can guarantee good power efficiency of the entire system. A full-wave rectifier realizes the energy conversion function in a single stage of the RF charge pump. This rectifier, shown in Figure 7(a), is also known as the *Schenkel rectifier*. An alternative differential approach is a diode bridge, known as the *Graetz bridge*, illustrated in Figure 7(b). Several rectifier stages are stuck in series to achieve a voltage multiplication with the RF charge pump. For this purpose, the multistage Dickson topology is widely used in CMOS applications [38]. The number of stages must be optimized, as too many can

reduce efficiency, linked to the parasitics added by each stage [39]. The number of available stages also determines the detection sensitivity, interpreted as the minimum input RF signal power level required for backscatter communication.

One of the critical rectifier design aspects is the diode component (see D1 and D2 in Figure 7(a)). A standard p-n junction diode has a significant voltage drop, resulting in considerable power losses. A Schottky diode with a much lower built-in voltage is better suited from this perspective; however, it is not always an available option in CMOS processes. Further, Schottky diodes often suffer from a higher reverse leakage current. A MOSFET

adaptation might be beneficial; the difficulty is that a diode-connected MOSFET needs a specific threshold voltage to conduct the rectifier current. Thus, various threshold voltage compensation techniques have been proposed [39], [40].

One of the most straightforward solutions is shown in Figure 7(c), where the gate terminals of the n- and p-channel MOSFETs are directly connected to the output terminals [41]. There is a disadvantage of this approach: if the single-stage charge pump output voltage reaches a specific high-enough dc value, the diode transistors are overbiased, resulting in significant reverse currents that degrade the power conversion

Ionizing Radiation Effects in Semiconductor Devices

When the energy of incident electromagnetic radiation is near or greater than the material bandgap energy, the material atoms can ionize, resulting in induced free electron-hole pairs. (The possible interaction mechanisms include the photoelectric and Compton effects.) This phenomenon is of great significance for electronic components. Ionizing radiation can penetrate a certain distance. Therefore, such a cloud of free charge carriers can appear in both the conductive and insulating layers in semiconductor devices. Electrons and holes will drift in the electric field in opposite directions and, if not recombined, collect at nearby electrodes. In the case of X-ray photon radiation, this effect does not influence the operation of most semiconductor devices, in stark contrast to the later-discussed energetic particles.

The problem appears when ionization happens in the device-insulating parts, where the charge carrier

mobility is orders of magnitude lower. For example, trapped charges in the oxide and Si oxide interface notably degrade the functionality of MOSFETs (Figure S4). The exposure of MOSFET transistors to ionizing radiation leads to shifting of the drain current-gate voltage ($I_D - V_G$) characteristics to lower voltages, as illustrated in Figure S5 [S7], due to parasitic electric fields associated with the oxide-trapped charge. Further, the interface traps cause the degradation of the subthreshold characteristics, i.e., increased leakage current, reduced mobility, and higher noise.

Ionizing radiation is not only X- and gamma-ray photons; it can also be particles with mass (e.g., alpha or beta radiation). In the case of charged particles, the interaction mechanism is via Coulomb forces. Many atoms can be ionized along the particle's trajectory, resulting in several phenomena referred to as single-event effects [S8]. A local high density

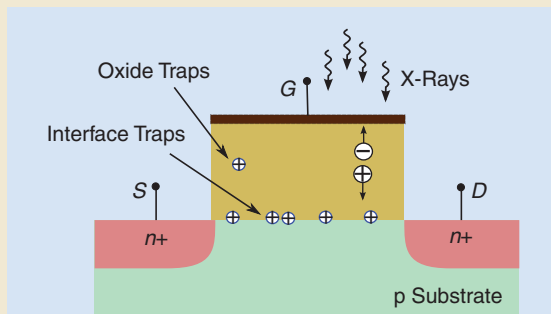


Figure S4. The radiation-induced traps in the MOSFET gate oxide and at its interface are generated when X-ray or other kinds of ionizing radiation interacts in the insulating layers of the device. The accumulation of traps over exposure time leads to a device parameter drift.

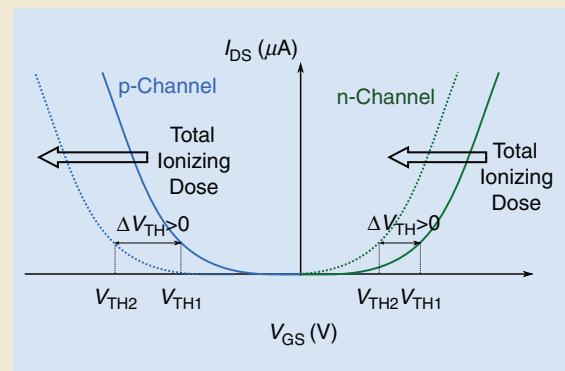


Figure S5. The shift of MOSFET $I_D - V_G$ characteristics as a result of a radiation-induced oxide-trapped charge: the p-channel $|V_{TH}|$ increases, and the n-channel $|V_{TH}|$ decreases.

efficiency. Introducing a precharge voltage based on a simple regulation stabilizes the gate bias voltage of the rectifying transistors, as illustrated in Figure 7(d) [42]. A more detailed discussion of the rectifier topologies and other design aspects of passive RFID tag subsystems can be found in [43]. Since the power efficiency of the RFID system highly depends on the charge pump design, it will be essential to consider design challenges related to radiation effects.

Radiation Hardness Challenges

The effects caused by ionizing radiation can have severe consequences for the operation of ICs, including the

discussed passive RFID tag chip circuits and subsystems. So far, there are no reports on the passive RFID chip performance under ionizing radiation. Therefore, the perspectives of radiation-hard RFID ICs are discussed considering, on the one hand, an analysis of existing passive RFID building blocks and their technology requirements and, on the other hand, an understanding of the radiation effects in CMOS circuits, their respective technologies, and mitigation strategies. These considerations include the degradation of device characteristics due to both total ionizing dose (TID) accumulated over a particular exposure time as well as failures related to single-event effects

Ionizing Radiation Effects in Semiconductor Devices (Continued)

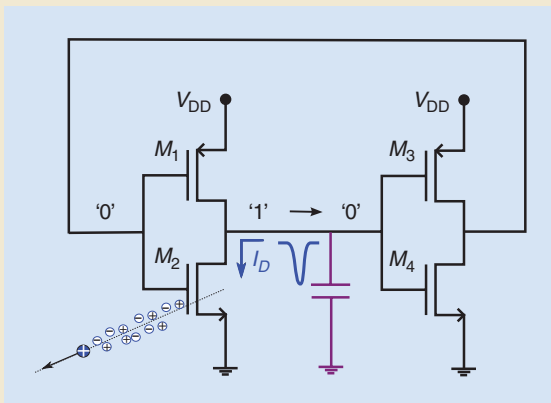


Figure S6. The transient current due to a single charged particle causes an SRAM bit flip. The tiny node capacitance discharges immediately if the particle passes near the transistor, and sufficiently large charges are induced via Coulomb forces and collected at the drain terminal. Such a transient event can become a problem anywhere in an analog or digital circuit.

of charge carriers changes the electric field and can be particularly dangerous for high-voltage devices. It might lead to a single-event gate rupture in power MOSFETs or destructive single-event burnout in MOSFET bulk diodes or p-i-n diodes [S9].

Further short transient currents near the collecting node can trigger a single-event latch-up in parasitic p-n-p-n structures or manifest at the circuit level as a single-event transient, i.e., a false signal, or even as a single-event upset (SEU), i.e., a memory bit state change. An SEU can happen either in static random-access memory (SRAM) as a result of a fast transient current discharging the node capacitance, illustrated in

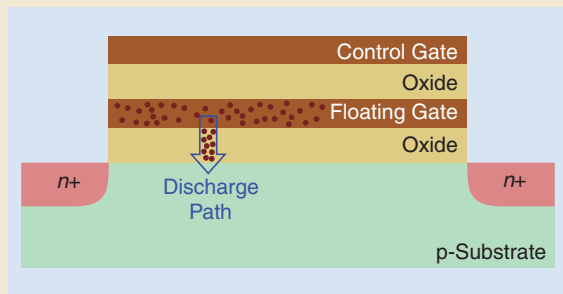


Figure S7. The effect shown is related to a single energetic charged particle that ionizes insulator atoms in a very short time, inducing a very high density of electron-hole pairs. As a consequence, this effect can lead to memory loss in a floating gate transistor-based nonvolatile memory.

Figure S6, or due to a leaky pipe in the oxide of a floating gate transistor bit [S10], illustrated in Figure S7. A shielding against ionizing radiation is not always practical. If the shield does not entirely absorb the radiation, a further interaction produces secondary radiation, increasing significantly the dose absorbed by the shielded component.

References

- [S7] J. Schwank *et al.*, "Radiation effects in MOS oxides," *IEEE Trans. Nucl. Sci.*, vol. 55, no. 4, pp. 1833–1853, 2008, doi: 10.1109/TNS.2008.2001040.
- [S8] V. Bezhenova and A. Michalowska-Forsyth, "Effects of ionizing radiation on integrated circuits," *e i Elektrotechnik und Inform. technik*, vol. 133, no. 1, pp. 39–42, 2016, doi: 10.1007/s00502-015-0380-8.
- [S9] J. Lutz, H. Schlangenotto, U. Scheuermann, and R. De Doncker, *Semiconductor Power Devices: Physics, Characteristics, Reliability*. Springer Science & Business Media, 2011.
- [S10] G. Cellerea and A. Paccagnella, "Subpicosecond conduction through thin SiO₂ layers triggered by heavy ions," *J. Appl. Phys.*, vol. 99, no. 7, 2006, doi: 10.1063/1.2181313.

(SEEs) associated with an individual high-energy charged particle.

For example, the RF charge pump is a critical block in the RF front end of RFID tag chips, and a change of its characteristics might result in the degradation of power conversion efficiency. Specifically, in the case of the diode rectifier shown in Figure 7(a) and (b), this situation can be related to radiation-induced degradation of the ideality factor and increased saturation current. Similarly, the performance of a MOSFET-based rectifier, as shown in Figure 7(c), is expected to change because of radiation-induced threshold voltage shifts and an increased off-state current (see “Ionizing Radiation Effects in Semiconductor Devices”). Another concern at the front-end level is the input impedance of the tag chip. The chip absorbing and the tag antenna impedances must be power matched for maximizing wireless power transfer [18]. A shift of the threshold voltages upon irradiation changes the MOS capacitance in its capacitance–voltage characteristics, possibly leading to an unintended impedance mismatch. Consequently, the front-end input impedance would need to be examined after ionizing radiation stress in a given application.

Typically, radiation-induced parameter drifts in CMOS processes are characterized based on dc measurements of MOSFET drain current–gate voltage ($I_D - V_G$) factors, which include the voltage threshold, off-state current, on-state current, and transconductance. However, in the case of RFID tags, the RF parameters of the circuit components are also critical. There are several

sources in the literature reporting on that. In [44], the scattering parameters of MOSFET devices fabricated in a 45-nm Si-on-insulator (SOI) technology are characterized after X-ray irradiation to a 0.5-Mrad TID. In addition to an increased leakage current and reduced relative threshold voltage (i.e., an increase of the absolute value in the MOSFET p-channel and decrease in the MOSFET n-channel), the small-signal current gain (i.e., the S_{21} parameter) has been characterized up to the gigahertz frequency range. The small-signal current gain is degrading with irradiation, reducing the cutoff frequency f_T of the devices. The RF circuit parameters are highly dependent on both S_{21} and f_T [45].

In [46], the RF performance change of bulk n-channel MOSFETs in a 120-nm Si germanium (SiGe) bipolar CMOS process is reported after irradiation with protons with a 1-Mrad TID. Similarly, the characterization extends to the gigahertz range, and, after exposure, a degradation in the cutoff frequency is observed. However, the proportional degradation is much smaller for this process, specific device geometry, and given experimental conditions. Further literature research points to similar findings with regard to the small-signal current gain and cutoff frequency, e.g., studies of floating-body 130-nm SOI MOSFETs under X-ray irradiation [47] or 65-nm SOI CMOS under proton irradiation [48].

These literature examples discuss the RF performance in SOI and SiGe CMOS processes, but similar studies for Si bulk CMOS have not been identified. Therefore, the reported RF performance degradation

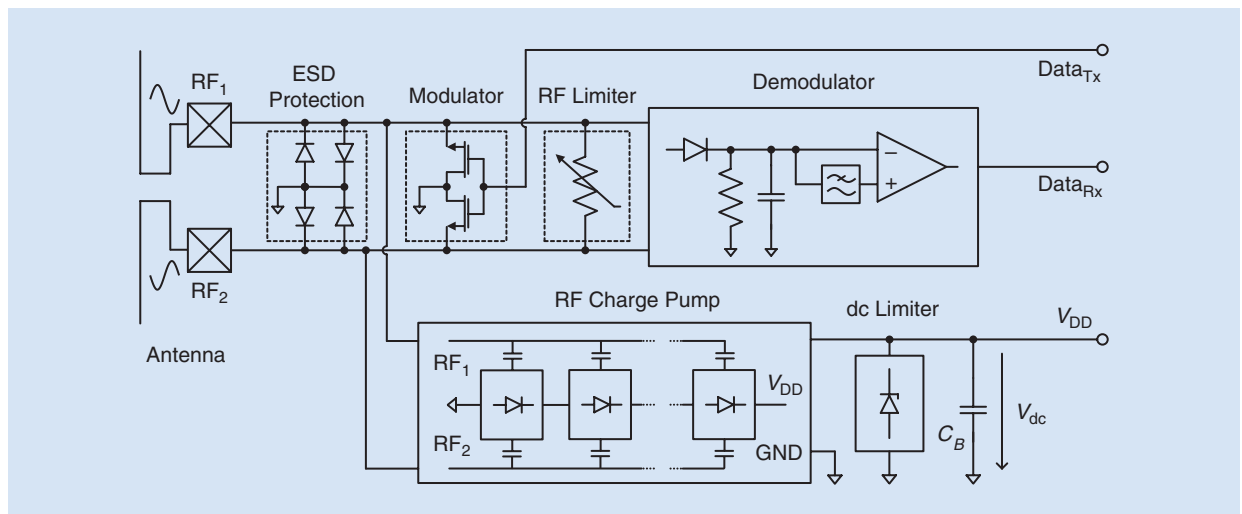


Figure 6. A block diagram of an exemplary differential front end of a UHF RFID tag chip [18], [36]. The RF charge pump rectifies the signal impinging at the antenna and provides a dc voltage at its output that is used as a voltage supply for the connected internal chip circuitry at node V_{DD} . The capacitor C_B decouples the RF part of the chip from the internal chip circuitry. Moreover, C_B presents one part of the buffer capacitance that buffers energy to supply the chip circuitry during modulation. The RF limiter and ESD protection are typically implemented as a combined circuit to protect the circuit from overvoltages at the chip input [18]. ESD: electrostatic discharge; GND: ground.

will not accurately correspond to the typical passive RF tag chip fabricated with bulk CMOS. However, the few examples point out the importance of frequency characterization against the TID in the context of passive RF tags after ionizing radiation stress. This is also essential for developing passive RFID space tags in SOI CMOS at millimeter-wave frequencies [49], which are outside the scope of this article.

Perspectives for the Mitigation of Radiation Effects

Both dc and RF parameter drifts can be approached at several levels of the IC concept to mitigate the side effects of the ionizing environment, i.e., at the process, layout (or physical), and architecture levels. The process-level mitigation can mean modifying the CMOS process, for example, to improve the gate oxide quality. However, technology selection also applies here. Already, considering a particular technology node alone, there are differences in the standard IC fabrication processes. For example, two IC components are made by different foundries but still have nearly identical performance parameters. This is often the case for some standard catalog off-the-shelf components. However, the two ICs can vary in their responses to ionizing radiation, showing different levels of intrinsic robustness.

Further, there are specific differences in radiation effects between the bulk CMOS and SOI technologies. In particular, the latter, where the bulk of each MOSFET device is isolated from the substrate and other devices, are robust against a single-event latch-up (SEL). As another benefit, independent of single events, SOI technologies are also characterized by a lower loss in RF signal transmission and lesser crosstalk in digital circuits. However, when exposed to the TID, the body oxide in SOI devices accumulates the radiation-induced traps, just as the gate oxide, or shallow trench oxide [50], manifesting in the shift of its characteristics after the TID.

So far, most of the attention has been devoted to the analog front end. However, the digital part and memory block, both included in an RFID tag chip, also need to be considered. Another SEE that must be discussed here is the single-event upset (SEU) (see “Ionizing Radiation Effects in Semiconductor Devices”). In the processing memory, like flip-flops, such an event would be considered a soft failure. A far more critical location is the EEPROM, where, next to other configuration parameters, the tag ID is stored. The EEPROM in many passive RFID tags is based on a floating gate non-volatile memory [51], [52]. In the case of a single event passing through the floating gate-adjacent oxide, the radiation-induced highly concentrated electron-hole pairs might create a leaky pipe, which is a leakage path

The effects caused by ionizing radiation can have severe consequences for the operation of ICs, including the discussed passive RFID tag chip circuits and subsystems.

for the stored charge (see “Ionizing Radiation Effects in Semiconductor Devices”).

Other types of EEPROM nonvolatile memories eliminate that risk, i.e., those based on charge-trapping mechanisms, where the stored charge is distributed in an insulating layer, like Si-oxide-nitride-Si (SONOS) [53], NROM [54], or a sidewall spacer [55]. Whether floating

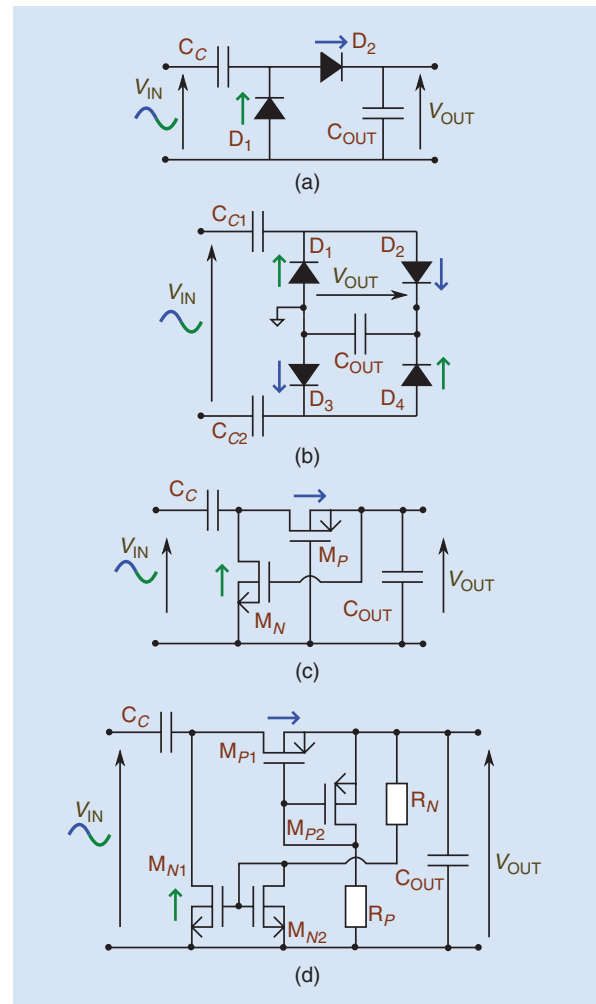


Figure 7. The schematics of (a) a full-wave rectifier as a single stage of the RF–dc charge pump, (b) a differential Graetz bridge rectifier, (c) a MOSFET-based rectifier with precharge gate voltage [41], and (d) a MOSFET-based rectifier with stabilized precharge gate voltage [42]. C: capacitance; D: diode; M: transistor; R: resistance.

Both dc and RF parameter drift can be approached at several levels of the IC concept to mitigate the side effects of the ionizing environment, i.e., at the process, layout, and architecture levels.

gate or charge trapping based, the TID effects also need to be addressed in any nonvolatile memory (see “Ionizing Radiation Effects in Semiconductor Devices”). In the case of the sidewall spacer, promising results are obtained [55] in addition to demonstrating an approach to monitor the device degradation over a lifetime by using memory sections with different values of the bit-cell programming time. Naturally, the selection of the EEPROM type is typically limited to a single component that a specific CMOS process offers. Despite these design constraints, it is crucial to recognize the differences between different EEPROM schemes and, above all, the risks in the context of space radiation reliability.

Process-level mitigation also includes considerations of the technology node. The performance of MOSFET devices after exposure to the TID can be found in the literature for various CMOS technologies, for example, in 130-nm and 65-nm bulk CMOS [56] or 28-nm

bulk CMOS [57]. Generally, smaller CMOS technology nodes are characterized by a thinner layer of gate Si dioxide. This property is beneficial since it is easier for the radiation-induced charge to escape the insulating layers via tunneling mechanisms. Consequently, the scaled-down processes tend to be more robust to the effects of the TID. This observation is beneficial for passive RFID chips since they follow the scaling trend because of cost benefits due to a decreased chip size [37].

Further, lower supply voltages in scaled technology nodes mean better robustness against SELs. However, the same low-power supply level combined with reduced node capacitances results in an increased sensitivity to single-event transients (SETs) and SEUs in flip-flops, or a static random-access memory (SRAM) cell. Also, with the reduced physical size, the circuit nodes are closer to each other, and a charge cloud originating from a single event can easily be collected in a shared manner among several nodes. The consequence could be, for example, a multiple-bit SEU. An intended spatial separation in circuit layout can significantly reduce the probability of multiple-bit upsets.

Radiation hardening by layout or layout-level techniques to mitigate radiation effects improves the immunity against SELs. These include applying safe spacing between n- and p-channel MOSFETs and the placement of appropriate guard rings. Furthermore, there are ways to reduce TID effects at the physical level. The most efficient one is the enclosed layout transistor (ELT) [58]. This layout approach eliminates the shallow trench isolation (STI) edge that connects the drain and source on both sides of the gate in a rectangular transistor, as illustrated in Figure 8(a). The STI is a thick, thermally grown oxide, typically of poor quality. Therefore, radiation-induced traps will form easily, leading to increased leakage current, particularly in an n-channel transistor, and variations in the threshold voltage [50]. ELT transistors, as shown in Figure 8(b), without the STI along the gate edge (from the drain to source implants), have significantly lower radiation degradation. Importantly, in such a nonstandard gate geometry, one has to take good care of modeling the transistor for simulation purposes [59]. Usually, it is done by calculating the equivalent dimensions of a standard squared-gate transistor.

Process nodes below 65 nm are very conservative in the layout design rules due to complex photolithography. However, engineers can further exploit device layout techniques for radiation hardening where applicable. In passive RFID tag ICs, the forward diode of the rectifier can be improved by realizing it as a dynamic-threshold MOS diode (DTMOS), initially proposed as a solution for ultra-low-power circuits thanks to its low threshold. The low-threshold feature is achieved

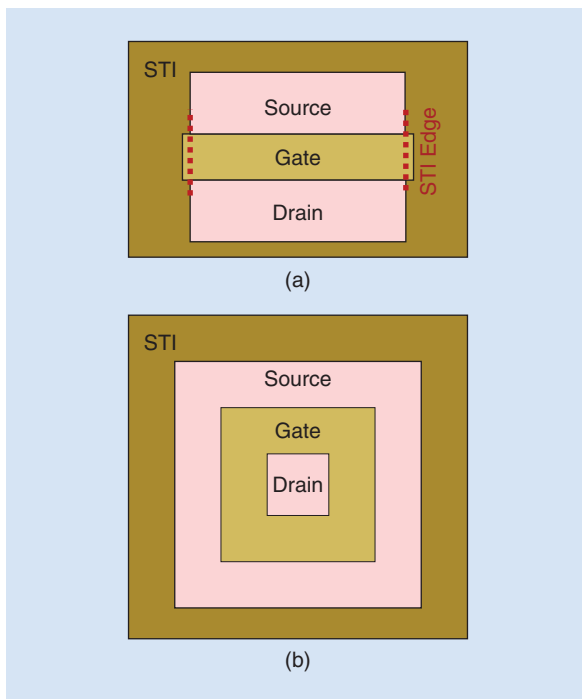


Figure 8. (a) A conventional rectangular MOSFET layout with a parasitic STI edge between the drain and source. (b) A radiation-hardened MOSFET in an enclosed layout.

by using a conventional MOSFET and tying the bulk and gate together, which results in a lowered surface potential under the gate. As a result, the built-in voltage of the drain-bulk diode will be much lower than in a conventional p-n diode.

This technique has already been implemented in RFID tag ICs [60]. However, the prototype includes only a standard rectangular transistor, where the radiation-susceptible STI edge is present between the drain and source. A radiation-hard approach can be adopted for ionizing environments, i.e., the same technique used in a forward diode for bandgap reference circuits. The DTMOS is then placed in an enclosed layout [61].

Architecture-level hardening of an IC improves the robustness against SETs and SEUs, e.g., by the SRAM as a dual interlocked storage cell [62], triple modular redundancy [63], differential charge cancellation [64], temporal filtering [65], or guard gate [66], and robustness against the TID, such as by adaptive compensation [67], chopper stabilization and autozero for radiation-induced mismatch [68], or negative gate-source voltage [69]. For a radiation-hardening-by-design approach, the block and circuit concepts have to be considered individually in each application since there are considerable tradeoffs that have to be faced, i.e., the power consumption, circuit die area, complexity influencing system level, clocked versus continuous mode approach, and so on.

The ultra-low-power capability of state-of-the-art passive RFID tags is enabled thanks to voltage-threshold compensation techniques in the rectifiers used in the RF charge pump. For the same reason, this part of the circuit is susceptible to shifts in the threshold voltage. In terms of radiation effects, if the p- and n-channel transistor pairs in the rectifier from Figure 7(d) are matched and degrade simultaneously, this block architecture can be considered an adaptive compensation mitigation approach. If the threshold voltage of the p-channel MOSFET MP1 increases with irradiation, it needs a larger gate bias to meet the same operating point as when unstressed. Simultaneously, the threshold voltage of the p-channel MOSFET MP2 generating the precharge-voltage also increases with irradiation, providing the required higher gate-to-source voltage of transistor MP1.

Finally, there are hardening considerations beyond the IC architecture, i.e., the operating conditions. Defining the periods of operation and power-down phases can significantly impact the degradation rate or risk of failure. For example, every time the Hubble Space Telescope flies over the South Atlantic Anomaly, a region with unusually high radiation levels in the Van Allen radiation belts, it interrupts the data acquisition to reduce the risk of single-event-related damage or data loss. Similarly, whenever the instrument is not in use,

In this work, some technologies and design techniques have been highlighted that engineers could exploit to harden the existing passive tag solutions against ionizing radiation.

a power down is also beneficial against the TID. The effects of radiation damage in MOSFETs are known to be bias voltage dependent [70]. With a positive electric field at the gate to the source, one observes the worst-case damage. Therefore, the benefit of powering down is of particular significance for reducing the damage of n-channel MOSFETs. This is highly relevant for passive RFID chips that are only biased while interrogated. From the reliability perspective, this RFID-specific activity pattern is also beneficial against bias-temperature instability and hot carrier degradation, where the applied electric fields (gate and drain-source voltages) act as stress factors.

Concluding Remarks

At present, no modern backscatter RFID sensor tags are in use in space, as the main issues for reliable operation have not yet been solved. However, a review of the existing prototypes shows evidence that these issues, i.e., tight power constraints due to the battery-less operation and the harsh space flight environment caused by ionizing radiation, can be overcome in the future. In particular, signal-pattern-based sensor tag systems show promising results in wireless power transfer, setup independence, and robustness in moderate and static multipath environments. Also, the trend of using scaled CMOS technologies for RFID tag chips and their passive operation promises radiation hardness to a certain extent.

Future work will focus to further improve the reliable operation of sensor tags and their radiation hardness to make space tags a reality. Concerning ultra-low-power operation, future work will focus on creating time-efficient design tools to realize application-specific sensor systems and their respective sensor antennas, and the robustness of sensor systems in specific RF propagation environments. Concerning radiation hardness, researchers will focus on investigating the tag chip and, in particular, its RF-dc converter to ensure a maximum wireless power transfer after irradiation. Engineers will identify the specific space environment (which depends on not only the orbit but also the shielding and material composition of the space habitat) and intrinsic robustness of the chosen CMOS process, finally implementing mitigation

strategies at the physical layout level, circuit concept, or system level.

In this work, some technologies and design techniques have been highlighted that engineers could exploit to harden the existing passive tag solutions against ionizing radiation. Ultimately, space tags will be an essential technological advancement to mitigate the mission performance risks of human missions to Mars and beyond by passively monitoring the physiological conditions of crew members and structural health of spaceflight equipment.

Acknowledgment

The authors would like to thank Prof. Peter Hadley from the Institute of Solid State Physics of Graz University of Technology for sharing his expertise on solid-state devices and semiconductor materials.

References

- [1] "NASA's journey to Mars," National Aeronautics and Space Administration, Washington, DC, USA, Oct. 2018. <https://www.nasa.gov/content/nasas-journey-to-mars>
- [2] W. Wilson and G. Atkinson, "Wireless sensors for space applications," *Sensors Transducers J.*, vol. 13, pp. 1–9, Dec. 2011.
- [3] W. Wilson and G. Atkinson, "Passive wireless sensor applications for NASA's extreme aeronautical environments," *IEEE Sensors J.*, vol. 14, no. 11, pp. 3745–3753, 2014, doi: 10.1109/JSEN.2014.2322959.
- [4] J. Kua, C. Arora, S. Loke, N. Fernando, and C. Ranaweera, "Internet of Things in space: A review of opportunities and challenges from satellite-aided computing to digitally-enhanced space living," Sep. 2021, arXiv:2109.05971.
- [5] R. Correia, N. Borges Carvalho, and S. Kawasaki, "Continuously power delivering for passive backscatter wireless sensor networks," *IEEE Trans. Microw. Theory Techn.*, vol. 64, no. 11, pp. 3723–3731, 2016, doi: 10.1109/TMTT.2016.2603985.
- [6] Q. Huang, J. Jiang, and Y. Deng, "Comparative evaluation of six wireless sensor devices in a high ionizing radiation environment," *IET Wireless Sensor Syst.*, vol. 10, no. 6, pp. 276–282, 2020, doi: 10.1049/iet-wss.2020.0035.
- [7] P. Brown *et al.*, "2E-3 Asset tracking on the international space station using global SAW tag RFID technology," in *Proc. IEEE Ultrasonics Symp.*, 2007, pp. 72–75, doi: 10.1109/ULTSYM.2007.31.
- [8] S. Manzari, S. Caizzone, C. Rubini, and G. Marrocco, "Feasibility of wireless temperature sensing by passive UHF-RFID tags in ground satellite test beds," in *Proc. IEEE Int. Conf. Wireless Space Extreme Environ. (WiSEE)*, 2014, pp. 1–6, doi: 10.1109/WiSEE.2014.6973074.
- [9] R. J. Barton, "Some fundamental limits on SAW RFID tag information capacity and collision resolution," in *Proc. IEEE Int. Conf. Wireless Space Extreme Environ.*, 2013, pp. 1–7.
- [10] K. Finkeneller, *RFID Handbook: Fundamentals and Applications in Contactless Smart Cards and Identification*. Chichester, U.K.: Wiley, 2003.
- [11] R. Bhattacharyya, C. Floerkemeier, and S. Sarma, "Low-cost, ubiquitous RFID-tag-antenna-based sensing," *Proc. IEEE*, vol. 98, no. 9, pp. 1593–1600, Sep. 2010, doi: 10.1109/JPROC.2010.2051790.
- [12] J. Grosinger, W. Pachler, and W. Bösch, "Tag size matters: Miniaturized RFID tags to connect smart objects to the Internet," *IEEE Microw. Mag.*, vol. 19, no. 6, pp. 101–111, 2018, doi: 10.1109/MMM.2018.2844029.
- [13] R. Fischbacher, L. Görtschacher, F. Amtmann, P. Priller, W. Bösch, and J. Grosinger, "Localization of UHF RFID magnetic field sensor tags," in *Proc. IEEE Radio Wireless Conf.*, Jan. 2020, pp. 169–172, doi: 10.1109/RWS45077.2020.9050026.
- [14] L. Görtschacher and J. Grosinger, "UHF RFID sensor system using tag signal patterns: Prototype system," *IEEE Antennas Wireless*

- Propag. Lett.*, vol. 18, no. 10, pp. 2209–2213, Sep. 2019, doi: 10.1109/LAWP.2019.2940336.
- [15] L. Görtschacher and J. Grosinger, "Localization of signal pattern based UHF RFID sensor tags," *IEEE Microw. Compon. Lett.*, vol. 29, no. 11, pp. 753–756, Sep. 2019, doi: 10.1109/LMWC.2019.2940082.
- [16] J. Grosinger, B. Deutschmann, L. Zöschner, M. Gadringer, and F. Amtmann, "HF RFID tag chip impedance measurements," *IEEE Trans. Instrum. Meas.*, early access, 2021, pp. 1–11, doi: 10.1109/TIM.2021.3130664.
- [17] G. Saxl, L. Görtschacher, T. Ussmueller, and J. Grosinger, "Software-defined RFID readers: Wireless reader testbeds exploiting software-defined radios for enhancements in UHF RFID systems," *IEEE Microw. Mag.*, vol. 22, no. 3, pp. 46–56, 2021, doi: 10.1109/MMM.2020.3042408.
- [18] J. Grosinger, L. Zöschner, L. Görtschacher, and W. Bösch, "Backscatter RFID systems," in *Antennas, Antenna Arrays and Microwave Devices, (Compendium on Electromagnetic Analysis. From Electrostatics to Photonics: Fundamentals and Applications for Physicists and Engineers)*, vol. 3, I. Tsukerman, Ed. Singapore: World Scientific Publishing, Aug. 2020, pp. 299–320.
- [19] J. Grosinger, L. Görtschacher, and W. Bösch, "Passive RFID sensor tag concept and prototype exploiting a full control of amplitude and phase of the tag signal," *IEEE Trans. Microw. Theory Techn.*, vol. 64, no. 12, pp. 4752–4762, Dec. 2016, doi: 10.1109/TMTT.2016.2623610.
- [20] P. Nikitin and K. Rao, "Antennas and propagation in UHF RFID systems," in *Proc. IEEE Int. Conf. RFID*, Apr. 2008, pp. 277–288, doi: 10.1109/RFID.2008.4519368.
- [21] G. Marrocco, "Pervasive electromagnetics: Sensing paradigms by passive RFID technology," *IEEE Wireless Commun.*, vol. 17, no. 6, pp. 10–17, Dec. 2010, doi: 10.1109/MWC.2010.5675773.
- [22] C. Occhiuzzi and G. Marrocco, "Precision and accuracy in UHF RFID power measurements for passive sensing," *IEEE Sensors J.*, vol. 16, no. 9, pp. 3091–3098, May 2016, doi: 10.1109/JSEN.2016.2526678.
- [23] J. Virtanen, L. Ukkonen, T. Bjoerninen, A. Elsherbeni, and L. Sydäenheimo, "Inkjet-printed humidity sensor for passive UHF RFID systems," *IEEE Trans. Instrum. Meas.*, vol. 60, no. 8, pp. 2768–2777, Aug. 2011, doi: 10.1109/TIM.2011.2130070.
- [24] X. Chen, L. Ukkonen, and T. Bjoerninen, "Passive e-textile UHF RFID-based wireless strain sensors with integrated references," *IEEE Sensors J.*, vol. 16, no. 22, pp. 7835–7836, Nov. 2016, doi: 10.1109/JSEN.2016.2608659.
- [25] S. Capdevila, L. Jofre, J. Romeu, and J. C. Bolomey, "Passive RFID based sensing," in *Proc. IEEE Int. Conf. RFID-Technol. Appl.*, Sep. 2011, pp. 507–512, doi: 10.1109/RFID-TA.2011.6068592.
- [26] X. Yi, C. Cho, J. Cooper, Y. Wang, M. Tentzeris, and R. Leon, "Passive wireless antenna sensor for strain and crack sensing – Electromagnetic modeling, simulation, and testing," *Smart Mater. Struct.*, vol. 22, no. 8, Aug. 2013, doi: 10.1088/0964-1726/22/8/085009.
- [27] C. Occhiuzzi and G. Marrocco, "Constrained-design of passive UHF RFID sensor antennas," *IEEE Trans. Antennas Propag.*, vol. 61, no. 6, pp. 2972–2980, Jun. 2013, doi: 10.1109/TAP.2013.2250473.
- [28] M. Caccami, S. Manzari, and G. Marrocco, "Phase-oriented sensing by means of loaded UHF RFID tags," *IEEE Trans. Antennas Propag.*, vol. 63, no. 10, pp. 4512–4520, Oct. 2015, doi: 10.1109/TAP.2015.2465891.
- [29] J. Zhang and G. Tian, "UHF RFID tag antenna-based sensing for corrosion detection characterization using principal component analysis," *IEEE Trans. Antennas Propag.*, vol. 64, no. 10, pp. 4405–4414, Oct. 2016, doi: 10.1109/TAP.2016.2596898.
- [30] M. Caccami and G. Marrocco, "Electromagnetic modeling of self-tuning RFID sensor antennas in linear and nonlinear regimes," *IEEE Trans. Antennas Propag.*, vol. 66, no. 6, pp. 2779–2787, Jun. 2018, doi: 10.1109/TAP.2018.2820322.
- [31] K. Zannas, H. El Matbouly, Y. Duroc, and S. Tedjini, "Self-tuning RFID tag: A new approach for temperature sensing," *IEEE Trans. Microw. Theory Techn.*, vol. 66, no. 12, pp. 5885–5893, Dec. 2018, doi: 10.1109/TMTT.2018.2878568.
- [32] S. Caizzone, E. Giampaolo, and G. Marrocco, "Setup-independent phase-based sensing by UHF RFID," *IEEE Antennas Wireless Propag. Lett.*, vol. 16, pp. 2408–2411, Jun. 2017, doi: 10.1109/LAWP.2017.2721432.

- [33] P. Nikitin, R. Martinez, S. Ramamurthy, H. Leland, G. Spiess, and K. Rao, "Phase based spatial identification of UHF RFID tags," in *Proc. IEEE Int. Conf. RFID (IEEE RFID 2010)*, Apr. 2010, pp. 102–109, doi: 10.1109/RFID.2010.5467253.
- [34] L. Mayer and A. Scholtz, "Sensitivity and impedance measurements on UHF RFID transponder chips," in *Proc. 2nd Int. EURASIP Workshop on RFID Technol.*, Jul. 2008, pp. 1–10.
- [35] X. Zhang, H. Li, and H. Chung, "Setup-independent UHF RFID sensing technique using multidimensional differential measurement," *IEEE Internet Things J.*, vol. 8, no. 13, pp. 10,509–10,517, 2021, doi: 10.1109/JIOT.2020.3048248.
- [36] L. Zöschner, P. Herkess, J. Grosinger, U. Muehlmann, D. Amschl, and W. Bösch, "Passive differential UHF RFID front-ends in a 40 nm CMOS technology," in *Proc. 47th European Microw. Conf. (EuMC)*, Oct. 2017, pp. 105–108, doi: 10.23919/EuMC.2017.8230810.
- [37] L. Zöschner *et al.*, "HF/UHF dual band RFID transponders for an information-driven public transportation system," *e i Elektrotechnik und Inform.stechnik*, vol. 133, no. 3, pp. 163–175, Jun. 2016, doi: 10.1007/s00502-016-0405-y.
- [38] J. Dickson, "On-chip high-voltage generation in MNOS integrated circuits using an improved voltage multiplier technique," *IEEE J. Solid-State Circuits*, vol. 11, no. 3, pp. 374–378, 1976, doi: 10.1109/JSSC.1976.1050739.
- [39] D. Shetty, C. Steffan, G. Holweg, W. Bösch, and J. Grosinger, "Submicrowatt CMOS rectifier for a fully passive wake-up receiver," *IEEE Trans. Microw. Theory Techn.*, vol. 69, no. 11, 2021, pp. 1–8, doi: 10.1109/TMTT.2021.3098694.
- [40] L. Zöschner, P. Herkess, J. Grosinger, U. Muehlmann, D. Amschl, and W. Bösch, "A differential threshold voltage compensated RF-DC power converter for RFID tag ICs," in *Proc. Integr. Nonlinear Microw. Millimetre-Wave Circuits Workshop (INMMiC)*, Apr. 2017, pp. 1–3, doi: 10.1109/INMMiC.2017.7927297.
- [41] K. Kotani and T. Ito, "High efficiency CMOS rectifier circuit with self-Vth-cancellation and power regulation functions for UHF RFIDs," in *Proc. IEEE Asian Solid-State Circuits Conf.*, 2007, pp. 119–122, doi: 10.1109/ASSCC.2007.4425746.
- [42] H. Nakamoto *et al.*, "A passive UHF RF identification CMOS tag IC using ferroelectric RAM in 0.35- μm technology," *IEEE J. Solid-State Circuits*, vol. 42, no. 1, pp. 101–110, 2007, doi: 10.1109/JSSC.2006.886523.
- [43] T. Soyata, L. Copeland, and W. Heinzelman, "RF energy harvesting for embedded systems: A survey of tradeoffs and methodology," *IEEE Circuits Syst. Mag.*, vol. 16, no. 1, pp. 22–57, 2016, doi: 10.1109/MCAS.2015.2510198.
- [44] S. Jagannathan *et al.*, "Sensitivity of high-frequency RF circuits to total ionizing dose degradation," *IEEE Trans. Nucl. Sci.*, vol. 60, no. 6, pp. 4498–4504, 2013, doi: 10.1109/TNS.2013.2283457.
- [45] C. Motchenbacher and J. Connelly, *Low-Noise Electronic System Design*. Hoboken, NJ, USA: Wiley, 1993.
- [46] S. Venkataraman *et al.*, "Impact of proton irradiation on the RF performance of 0.12 μm CMOS technology," in *Proc. IEEE Int. Reliability Phys. Symp.*, 2005, pp. 356–359.
- [47] H. Ge *et al.*, "Comparing the TID-induced RF performance degradation of floating body and body contacted 130 nm SOI NMOS transistors," *Microelectron. Reliab.*, vol. 104, p. 113547, Jan. 2020, doi: 10.1016/j.microrel.2019.113547.
- [48] A. Madan, S. Phillips, J. Cressler, P. Marshall, Q. Liang, and G. Freeman, "Impact of proton irradiation on the RF performance of 65 nm SOI CMOS technology," *IEEE Trans. Nucl. Sci.*, vol. 56, no. 4, pp. 1914–1919, 2009, doi: 10.1109/TNS.2009.2014064.
- [49] A. Harutyunyan, "Analog frontend for ultra low power 60-GHz RFID tag for back-scattering communication," in *Proc. Smart Systech 2018: European Conf. Smart Objects, Syst. Technol.*, 2018, pp. 1–7.
- [50] F. Faccio *et al.*, "Total ionizing dose effects in shallow trench isolation oxides," *Microelectron. Reliab.*, vol. 48, no. 7, pp. 1000–1007, 2008, doi: 10.1016/j.microrel.2008.04.004.
- [51] C. Lu, Y. Li, J. Ou, H. Wu, and H. Tan, "A low power EEPROM for passive RFID tag IC," in *Proc. IEEE Int. Conf. RFID Technol. Appl. (RFID-TA)*, 2016, pp. 49–54, doi: 10.1109/RFID-TA.2016.7750732.
- [52] K. Lee, J. Chun, and K. Kwon, "A low power CMOS compatible embedded EEPROM for passive RFID tag," *Microelectron. J.*, vol. 41, no. 10, pp. 662–668, 2010, doi: 10.1016/j.mejo.2010.06.006.
- [53] M. White, D. Adams, and J. Bu, "On the go with SONOS," *IEEE Circuits Devices Mag.*, vol. 16, no. 4, pp. 22–31, 2000, doi: 10.1109/101.857747.
- [54] B. Eitan, P. Pavan, I. Bloom, E. Aloni, A. Frommer, and D. Finzi, "NROM: A novel localized trapping, 2-bit nonvolatile memory cell," *IEEE Electron Device Lett.*, vol. 21, no. 11, pp. 543–545, 2000, doi: 10.1109/55.877205.
- [55] T. Vincenzi, G. Schatzberger, and A. Michalowska-Forsyth, "Program time effects on total ionizing dose tolerance of sidewall spacer memory bit cell," in *Proc. Austrochip Workshop on Microelectron. (Austrochip)*, 2019, pp. 55–58, doi: 10.1109/Austrochip.2019.00021.
- [56] F. Faccio, S. Michelis, D. Cornale, A. Paccagnella, and S. Gerardin, "Radiation-induced short channel (RISCE) and narrow channel (RINCE) effects in 65 and 130 nm MOSFETs," *IEEE Trans. Nucl. Sci.*, vol. 62, no. 6, pp. 2933–2940, 2015, doi: 10.1109/TNS.2015.2492778.
- [57] C. Zhang *et al.*, "Characterization of gigarad total ionizing dose and annealing effects on 28-nm bulk MOSFETs," *IEEE Trans. Nucl. Sci.*, vol. 64, no. 10, pp. 2639–2647, 2017, doi: 10.1109/TNS.2017.2746719.
- [58] W. Snoeys *et al.*, "Layout techniques to enhance the radiation tolerance of standard CMOS technologies demonstrated on a pixel detector readout chip," *Nucl. Instrum. Methods Phys. Res. A, Accelerators, Spectrometers, Detectors Associated Equipment*, vol. 439, nos. 2–3, pp. 349–360, 2000, doi: 10.1016/S0168-9002(99)00899-2.
- [59] V. Bezhenova and A. Michalowska-Forsyth, "Modeling of annular gate MOS transistors," in *Proc. 18th European Conf. Radiation Its Effects Components Syst. (RADECS)*, 2018, pp. 1–4, doi: 10.1109/RADECS45761.2018.9328697.
- [60] S. S. Chouhan and K. Halonen, "The design and implementation of DTMOS biased all PMOS rectifier for RF energy harvesting," in *Proc. IEEE 12th Int. New Circuits Syst. Conf. (NEWCAS)*, pp. 444–447, 2014, doi: 10.1109/NEWCAS.2014.6934078.
- [61] V. Gromov, A. Annema, R. Kluit, J. Visschers, and P. Timmer, "A radiation hard bandgap reference circuit in a standard 0.13 μm CMOS technology," *IEEE Trans. Nucl. Sci.*, vol. 54, no. 6, pp. 2727–2733, 2007, doi: 10.1109/TNS.2007.910170.
- [62] T. Calin, M. Nicolaidis, and R. Velazco, "Upset hardened memory design for submicron CMOS technology," *IEEE Trans. Nucl. Sci.*, vol. 43, no. 6, pp. 2874–2878, 1996, doi: 10.1109/23.556880.
- [63] K. Morgan, D. McMurtrey, B. Pratt, and M. Wirthlin, "A comparison of TMR with alternative fault-tolerant design techniques for FPGAs," *IEEE Trans. Nucl. Sci.*, vol. 54, no. 6, pp. 2065–2072, 2007, doi: 10.1109/TNS.2007.910871.
- [64] B. Olson, W. Holman, L. Massengill, B. Bhuvu, and P. Fleming, "Single-event effect mitigation in switched-capacitor comparator designs," *IEEE Trans. Nucl. Sci.*, vol. 55, no. 6, pp. 3440–3446, 2008, doi: 10.1109/TNS.2008.2006895.
- [65] D. Mavis and P. Eaton, "Soft error rate mitigation techniques for modern microcircuits," in *Proc. IEEE Int. Reliability Phys. Symp.*, 2002, pp. 216–225, doi: 10.1109/RELPHY.2002.996639.
- [66] M. Baze *et al.*, "Propagating SET characterization technique for digital CMOS libraries," *IEEE Trans. Nucl. Sci.*, vol. 53, no. 6, pp. 3472–3478, 2006, doi: 10.1109/TNS.2006.884969.
- [67] J. De Vos, V. Kilchytska, D. Flandre, and D. Bol, "Compensation of total ionizing dose effects in ULV SoCs through adaptive voltage scaling," in *Proc. SOI-3D-Subthreshold Microelectron. Technol. Unified Conf. (S3S)*, 2014, pp. 1–2.
- [68] C. Enz and G. Temes, "Circuit techniques for reducing the effects of op-amp imperfections: Autozeroing, correlated double sampling, and chopper stabilization," *Proc. IEEE*, vol. 84, no. 11, pp. 1584–1614, 1996, doi: 10.1109/5.542410.
- [69] D. Pan, H. Li, and B. Wilamowski, "A radiation-hard phase-locked loop," in *Proc. IEEE Int. Symp. Ind. Electron.*, 2003, vol. 2, pp. 901–906, doi: 10.1109/ISIE.2003.1267941.
- [70] G. Borghello *et al.*, "Effects of bias and temperature on the dose-rate sensitivity of 65-nm CMOS transistors," *IEEE Trans. Nucl. Sci.*, vol. 68, no. 5, pp. 573–580, 2021, doi: 10.1109/TNS.2021.3062622.



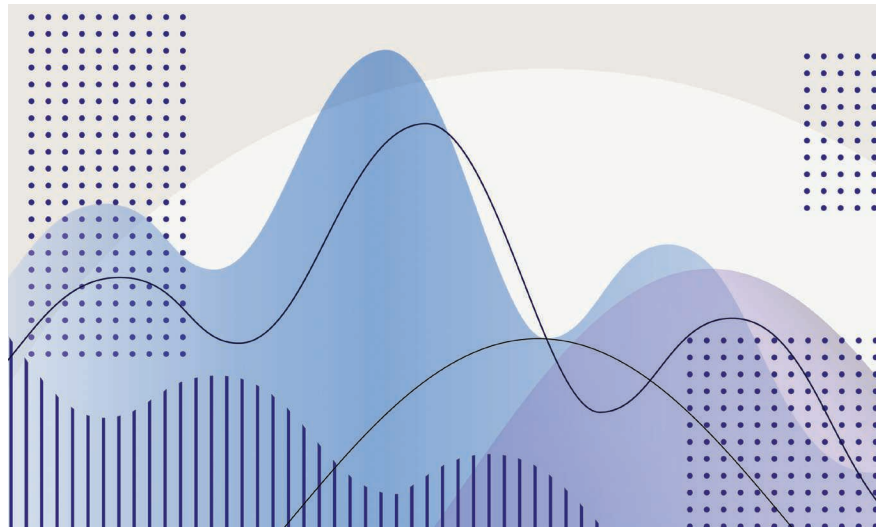


High-Efficiency Power
Amplifier for 13.56 MHz

Class DE Switch- Mode Power Amplifier Using GaN Power HEMTs

Zikang Tong, Zhechi Ye, and Juan Rivas-Davila

High-efficiency power amplifiers (PAs) are critical for various applications that require high power density, portability, and effortless thermal management. Historically, these types of PAs, operating in the tens-of-megahertz range in the industrial, scientific, and medical bands, were equipped for transmitters for fixed radiocommunication services, RF heating, and plasma ignition [1], [2]. Today, applications have expanded to wireless power transmission for biomedical devices and charging for



©SHUTTERSTOCK.COM/ LIUBOVART

Zikang Tong (ztong@stanford.edu), Zhechi Ye (yez15@stanford.edu), and Juan Rivas-Davila (jmrivas@stanford.edu) are with Stanford University, Stanford, California, 94305, USA.

Digital Object Identifier 10.1109/MMM.2021.3132111

Date of current version: 3 February 2022

consumer electronics and smart vehicles [3]. In this article, we present the first-place design for the Student Design Competition (SDC) High-Efficiency Power Amplifier for 13.56 MHz in the 2021 IEEE Microwave Theory and Techniques Society International Microwave Symposium (IMS) in Atlanta, Georgia. The competition required participants to develop a PA for the following specifications:

- deliver between 10 and 11 W of RF power at 13.56 MHz into a 50- Ω load
- operate from a 12-V dc supply
- operate from a 10-dBm ($2 V_{pk-pk}$) constant-amplitude sine input
- achieve an input standing-wave ratio of $< 2:1$ relative to 50 Ω
- achieve < -40 -dBc harmonic peaks up to 100 MHz
- and achieve nonharmonic spurs < -70 dBc between 10 kHz to 100 MHz.

With these specifications satisfied, the winning design achieved the highest efficiency, defined as

$$\eta = \frac{\text{RF Power at 13.56 MHz}}{\text{Total dc Input Power}}. \quad (1)$$

Our design can be described by the diagram in Figure 1. The system contains a switch-mode PA block that converts dc power from the 12-V supply to a 13.56-MHz RF signal. A matching network/filter stage interfaces between the PA block and the 50- Ω load to ensure proper RF power delivery between 10 to 11 W with minimal harmonic content. Additionally, the system contains three auxiliary stages to convert the input RF signal into a pulsewidth modulation (PWM) to drive the transistor gates in the amplifier. For maximum efficiency, careful consideration must be given to the topology selection, gate-drive design, and passive

The system contains a switch-mode PA block that converts dc power from the 12-V supply to a 13.56-MHz RF signal.

component design, particularly the magnetics. We showcase the results for the amplifier based on the design, with measurements to confirm the satisfaction of the competition rules.

High-Efficiency PA Design

Topology Selection

The first and most important design choice for high-efficiency PAs is the amplifier circuit topology. There are three families of PA circuits categorized by their modes of operation: linear mode, where the semiconductor operates mostly in the linear portion of its I - V curve; critical mode, where the switch operation can extend up to saturation and cutoff; and nonlinear mode (also known as *switch mode*), where current through the device ceases during a part of the periodic cycle [4]. Accordingly, amplifiers operating under switch mode achieve the highest efficiencies. The common topologies for switch-mode PAs include class-D, -E, and -F circuits. Although all three circuits have 100% theoretical efficiency, the parasitic drain-source capacitance of the switching device hinders the performance at high frequencies (HFs) as it generates switching loss. The exception is the class-E amplifier, which operates under zero-voltage switching (ZVS), a condition where the drain-source voltage of the transistor reaches zero before it turns on, thus eliminating the transistor's switching loss [5]. This behavior has greatly

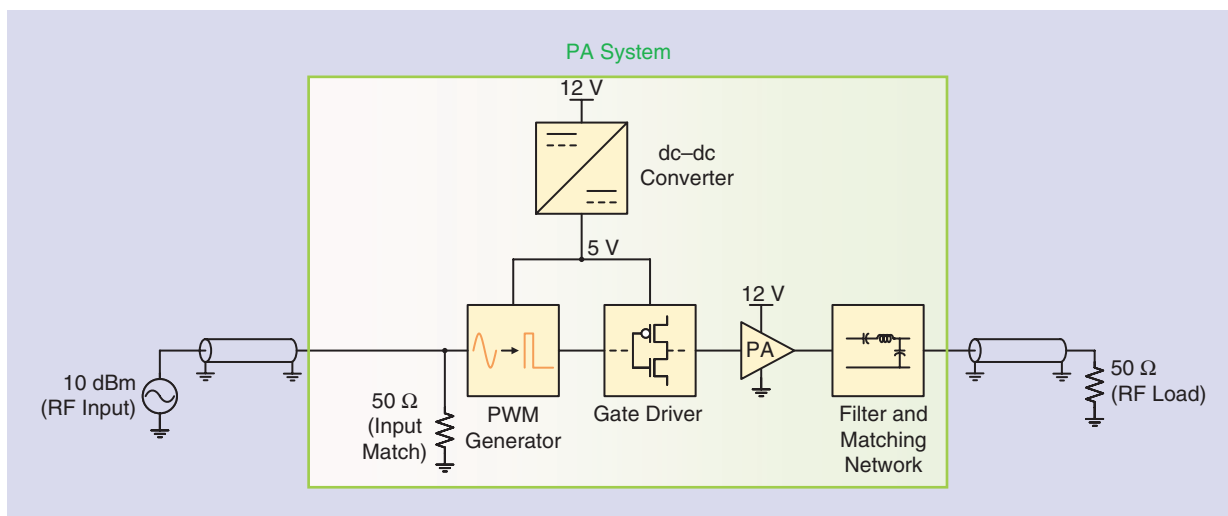


Figure 1. The PA system used to meet the targeted specifications. PWM: pulsewidth modulation.

GaN devices can be preferable over traditional silicon devices due to their lower on-resistance for equivalent parasitic output capacitance.

popularized the class-E topology as it allows high efficiency at HF operating ranges. However, hybrid topologies, such as the class-DE and the class-EF₂ circuits, have been extensively studied as well [6], [7]. Figure 2 shows a schematic of the various common amplifier topologies capable of achieving ZVS.

As a metric of comparison, the transistor-utilization factor of a switch-mode amplifier is defined as the ratio of the output power to the total product of a switch's peak voltage and root-mean-square current. The amplifiers with a higher transistor-utilization factor generally have higher drain efficiencies. When considering only conduction loss from the switches, the drain efficiency (η_D) can be approximated using (2), where V_{pk} is the peak voltage across the switch, R_{on} is its on-resistance, N is the number of switches, and c_{pmr} is the transistor-utilization factor [8]:

$$\eta_D = 1 - \frac{P_{out}R_{on}}{c_{pmr}^2 V_{pk}^2 N}. \quad (2)$$

Table 1 compares the performance of the various ZVS amplifier topologies. For this competition, we selected a class-DE topology because it has the highest transistor-utilization factor, resulting in the best efficiency compared to the other available topologies.

Class-DE Amplifier Design

For the class-DE circuit schematized in Figure 2(a), we selected the GS61004B gallium nitride (GaN) transistor from GaN Systems Inc. (Canada) as the switching device. GaN devices can be preferable over traditional silicon (Si) devices due to their lower on-resistance for equivalent parasitic output capacitance. The design of a class-DE amplifier is explained in detail by Hamill in [6]. According to this paper, the output power P_{out} of

a class-DE amplifier is a function of the switch duty-cycle D , the switch's parallel capacitance C_p , input dc voltage V_{in} , and switching frequency f_{sw} :

$$P_{out} = 2f_{sw}C_pV_{in}^2 \frac{1 + \cos(\pi - 2\pi D)}{1 - \cos(\pi - 2\pi D)}. \quad (3)$$

From the design specifications, V_{in} and f_{sw} are fixed to 12 V and 13.56 MHz, respectively. To minimize the conduction loss through the devices, D should be maximized (where the maximum value is 0.5) and C_p should be minimized. Due to the parasitic output capacitance of the GaN transistors, the minimum C_p value is roughly 300 pF, resulting in a switch duty cycle of approximately 0.4 for the PA to deliver 11 W of RF power [9]. To achieve ZVS and zero-derivative voltage switching, which minimizes the conduction loss through the system, the load impedance at the fundamental frequency must be a specific value determined by (4):

$$Z_L = \frac{\sin^2(\pi - 2\pi D)}{4\pi^2 f_{sw} C_p} + j \frac{\pi(1 - 2D) - \sin(\pi - 2\pi D) \cos(\pi - 2\pi D)}{4\pi^2 f_{sw} C_p}. \quad (4)$$

The derivation for this equation is discussed by Hamill in [6]. Based on Figure 2(a), at the fundamental frequency, C_{dc} is a large, dc-blocking capacitor behaving as a short, and L_s , in series with C_s , also form a short. Therefore, the equivalent load impedance at the fundamental frequency is $R_L \parallel j2\pi f_{sw} L_{res}$. By equating this impedance with the desired load impedance presented in (4), we obtain the values for R_L and L_{res} using (5) and (6), respectively:

$$R_L = \text{Re}\{Z_L\} \left[1 + \left(\frac{\text{Im}\{Z_L\}}{\text{Re}\{Z_L\}} \right)^2 \right] \quad (5)$$

$$2\pi f_{sw} L_{res} = \text{Im}\{Z_L\} \left[1 + \left(\frac{\text{Re}\{Z_L\}}{\text{Im}\{Z_L\}} \right)^2 \right]. \quad (6)$$

For our design, the desired load resistance R_L of the amplifier is 2.5 Ω , and the resonant inductor L_{res} to enable ZVS operation is set to 60 nH.

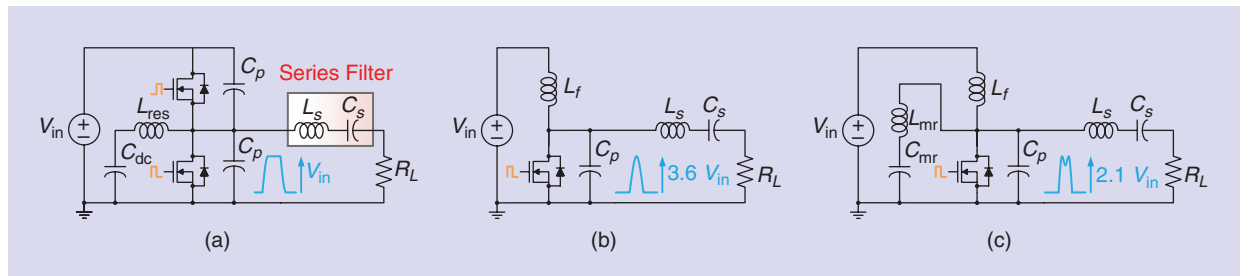


Figure 2. (a) A schematic of the class-DE amplifier, where C_{dc} serves as a dc-blocking capacitor. (b) A schematic of the class-E amplifier and (c) class-EF₂ amplifier.

Filtering and Output Matching Network

As the load resistance is given as $50\ \Omega$ instead of the desired $2.5\ \Omega$, an LC impedance-matching network is required. To perform the impedance transformation, we insert a low-pass, low-to-high, L-matching network between the series filter and the load resistance. To transform $50\ \Omega$ to $2.5\ \Omega$ at 13.56 MHz, the required shunt capacitance is 1,023 pF, and the series inductance is 128 nH. The low-pass matching network provides an additional function by serving as filter. As a part of the criteria, the amplifier's output must have its harmonic power at least 40 dB below the carrier's. Although the matching network provides -40 -dB/decade attenuation past its resonant frequency, it is generally not enough to satisfy the requirement. Therefore, we use the series-resonant network [see Figure 2(a)] to further help filter the output power. The series filter is a simple LC network with its resonant frequency tuned to 13.56 MHz. The final inductor and capacitor values can be calculated from the network's quality (Q) factor from (7):

$$Q_s = \frac{2\pi f_{sw} L_s}{R_L} \quad (7)$$

Having a higher Q_s results in greater filter attenuation; however, the tradeoff with utilizing a higher Q factor is that the inductance value increases, potentially leading to greater losses. In our design, we target a -50 -dBc attenuation for the third harmonic, resulting in a Q factor of 7.5 and $L_s = 222$ nH, $C_s = 620$ pF.

Auxiliary Stages

DC-DC Converter Stage

Because the PWM generator block and the gate driver contain logic integrated circuits (ICs) that can operate only up to a maximum 5-V dc supply, we must include a subsystem that can generate this bus voltage from

TABLE 1. A performance comparison among various switch-mode PA topologies with soft-switching capabilities. (For the class-DE circuit in this table, the duty cycle (D) is set to 0.33. A greater duty cycle leads to higher transistor utilization.)

Topology	Voltage Stress (V_{pk})	Switch Count (N)	Transistor-Utilization Factor (C_{pmr})
Class DE	V_{in}	2	0.26 ($D = 0.33$)
Class E	$3.6 V_{in}$	1	0.18
Class EF ₂	$2.1 V_{in}$	1	0.25
Class E/F	$3.14 V_{in}$	1	0.21

the main 12-V dc input. The simplest solution is to utilize a low-dropout (LDO) linear voltage regulator. Although LDOs are easy-to-use, inexpensive options, the downside is that they produce significant loss at high output currents, making them impractical for maximizing the total efficiency of the PA. An alternative is to utilize a dc-dc converter. The rules of the SDC state that participants are not allowed to include preconstructed submodules. Therefore, we designed a buck-boost converter utilizing the TPS63060 IC, which includes integrated power switches and voltage-regulation control circuitry [10]. Figure 4 displays the schematic for the buck-boost design. The additional components to include are the inductor, which we selected as an off-the-shelf 3.3- μ H inductor; the feedback resistors ($R_{FB1} = 1\ \text{M}\Omega$, $R_{FB2} = 111\ \text{k}\Omega$); and dc-filtering capacitors, which are 10- μ F ceramic capacitors.

RF Input to PWM Conversion

The class-DE amplifier also requires two pulsewidth-modulated signals to drive the switch gates. These two signals must have equivalent duty cycles of 0.4 and be

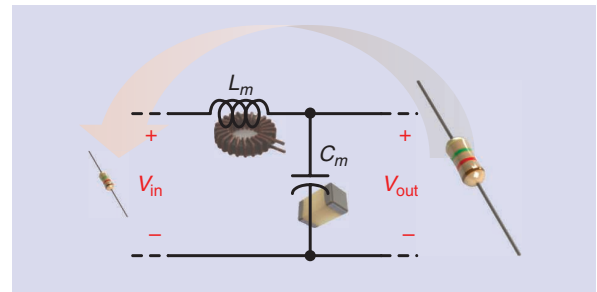


Figure 3. A diagram of the low-pass, low-to-high, L-matching network.

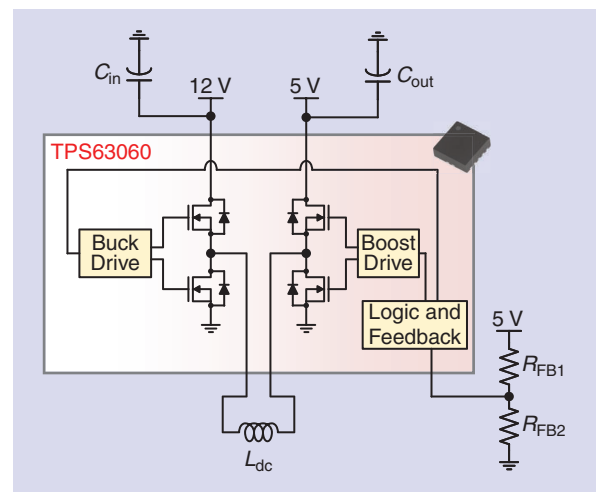


Figure 4. A schematic of the dc-dc converter block used to produce the 5-V supply rail.

The power dissipation from the gate drive can significantly lower the efficiency of the amplifier, which means that careful consideration of the switching device and gate-driving circuitry must be given.

180° phase shifted. To acquire these signals, our design must include supplementary circuitry that converts the 10-dBm sinusoidal input to the two PWM voltages. The additional circuitry is diagrammed in Figure 5.

First, we feed the 10-dBm signal into the positive input of a comparator with the negative input connected to ground, the positive supply rail tied to the 5-V bus, and the negative supply terminal tied to ground. This allows the comparator to generate the square waveform of a 0.5 duty cycle as the comparator outputs high during the positive half cycle of the sine input and outputs low during the negative half cycle of the input. The comparator IC that we selected has a part number of TLV3501. Next, the square wave drives a logic buffer and a logic inverter to create two 180° phase-shifted square waves. To lower the duty cycle from 0.5 to 0.4, the outputs of the buffer and inverter drive a resistor-capacitor-diode dead-time generator circuit to slow the rising ramp time of the square waveform. These two signals are inputted into logic buffers to create the final gate waveforms of a 0.4 duty cycle.

Gate Power Loss and Device Selection

In HF switch-mode converters and amplifiers, a gate-drive IC buffers between the PWM signal and the transistor gate. The transistor gate can be modeled as

a resistance (R_{gate}) in series with a capacitance (C_{gate}), which is typically on the order of tens to hundreds of picofarads for power MOSFETs. As a result, the power dissipation from the gate drive can significantly lower the efficiency of the amplifier, which means that careful consideration of the switching device and gate-driving circuitry must be given. In general, there are two methods used to periodically charge and discharge a gate capacitance. The first method is driving the gate with a voltage source, as depicted in Figure 6(a). The gating power loss is described by (8), where P_{gate} is the power consumption and V_{gate} is the voltage required to enhance the device:

$$P_{\text{gate}} = f_{\text{sw}} C_{\text{gate}} V_{\text{gate}}^2. \quad (8)$$

For a voltage-source gate driver, the power dissipation is proportional to the gate capacitance and the square of the gate-enhancement voltage. Therefore, to minimize the gating loss, we must select a power device with a small gate capacitance and a low turn-on voltage. Another benefit of GaN transistors is that they ordinarily have the lowest gate capacitance and voltage [11]. For the GS61004B GaN high-electron mobility transfer, the gate capacitance is 260 pF according to the data sheet and the on-state voltage is 5 V, which results in $P_{\text{gate}} = 88 \text{ mW}$ per switch [9].

The second method used to periodically charge and discharge a transistor gate is a current-source driver, as presented in Figure 6(b). The gate power loss is described by (9):

$$P_{\text{gate}} = R_{\text{gate}} C_{\text{gate}}^2 V_{\text{gate}}^2 f_{\text{sw}} \left(\frac{t_{\text{rise}} + t_{\text{fall}}}{t_{\text{rise}} t_{\text{fall}}} \right). \quad (9)$$

Unlike the voltage-source driver, the current-source-based gate driver's dissipation is proportional to the

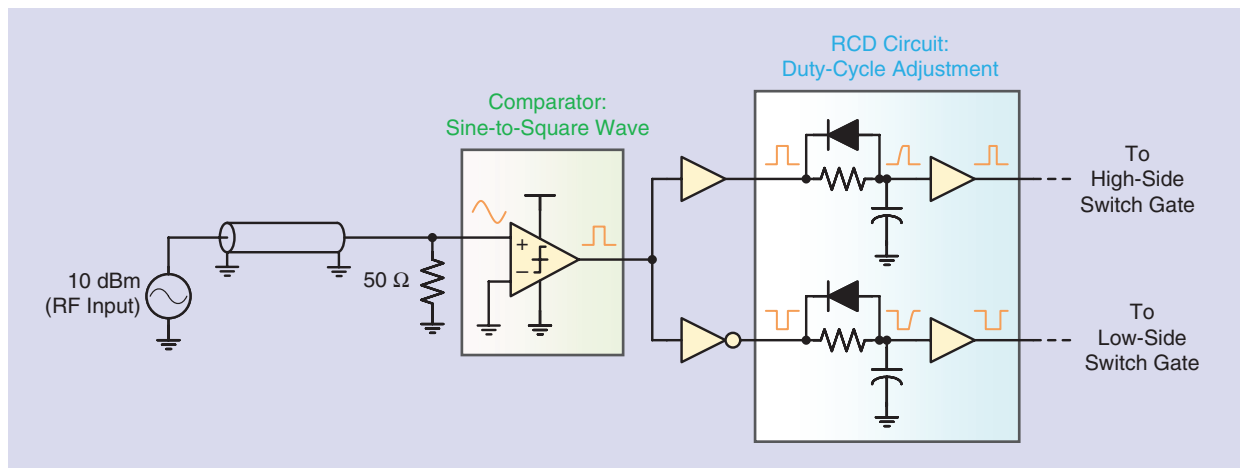


Figure 5. A schematic of the circuit used to convert the 10-dBm sinusoidal input to the PWM signals used to drive the transistor gates. RCD: resistor capacitor diode.

gate resistance R_{gate} . Thus, if the switching device has negligible gate resistance, the gating power loss can be neglected and the gate capacitance can be resonantly charged and discharged. However, additional circuitry must be included to develop a current-source gate driver, as demonstrated by Chen et al. [12].

Half-Bridge Driving Solutions

As the class-DE PA includes a high-side transistor with its source referenced to the switching node, the high-side gate-drive voltage must be referenced to the switching node. There exist two common methods for resolving this challenge. The first is to utilize a bootstrap circuit, as shown in Figure 7(a). For this method, the PWM signal is communicated through a signal isolator, which is often a commercial IC or broadband transformer with low coupling capacitance. The gate driver (“GD” in the schematic) has its supply voltage held constant with a large decoupling capacitor. When the switching voltage is low, the capacitor has its charge restored from the 5-V supply with the conduction path activated by the diode. To ensure symmetry between the high- and low-side transistors, the low-side switch should also contain a bootstrap diode and signal isolator so that the propagation delay and gate-drive supply voltage can be matched.

The secondary method used to power the high-side gate driver is to utilize isolated dc–dc converters. The dc–dc converters provide supply rails that can be referenced to any node, but it is crucial that they contain low coupling capacitance so that they can be immune to common-mode transients. Due to the competition’s rules, participants cannot utilize this option unless

This behavior has greatly popularized the class-E topology as it allows high efficiency at HF operating ranges.

they develop custom isolated dc–dc converters. Therefore, we utilized the bootstrap technique. The gate-drive IC that we selected is the PE29102 from pSemi (USA), which contains internal signal isolators.

Magnetics Design

Careful consideration must be given to designing the magnetic components as they can be difficult to achieve high power densities, especially at HFs [13]. The inductors in RF PAs follow the same procedures as magnetic components in switch-mode power converters. Generally, circuit designers set a maximum limit on the magnetic flux density (B-field) as magnetic cores have saturation limits and suffer from core loss, which scales with the B-field. In general, the upper limit for

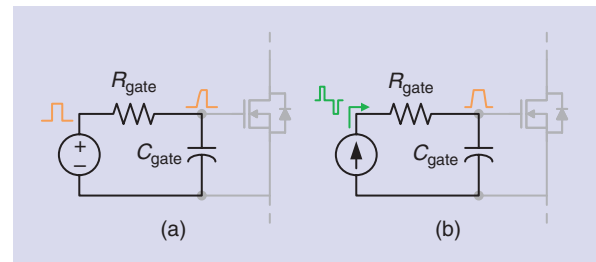


Figure 6. (a) The schematic of a voltage source-based gate driver and (b) a current-source-based gate driver.

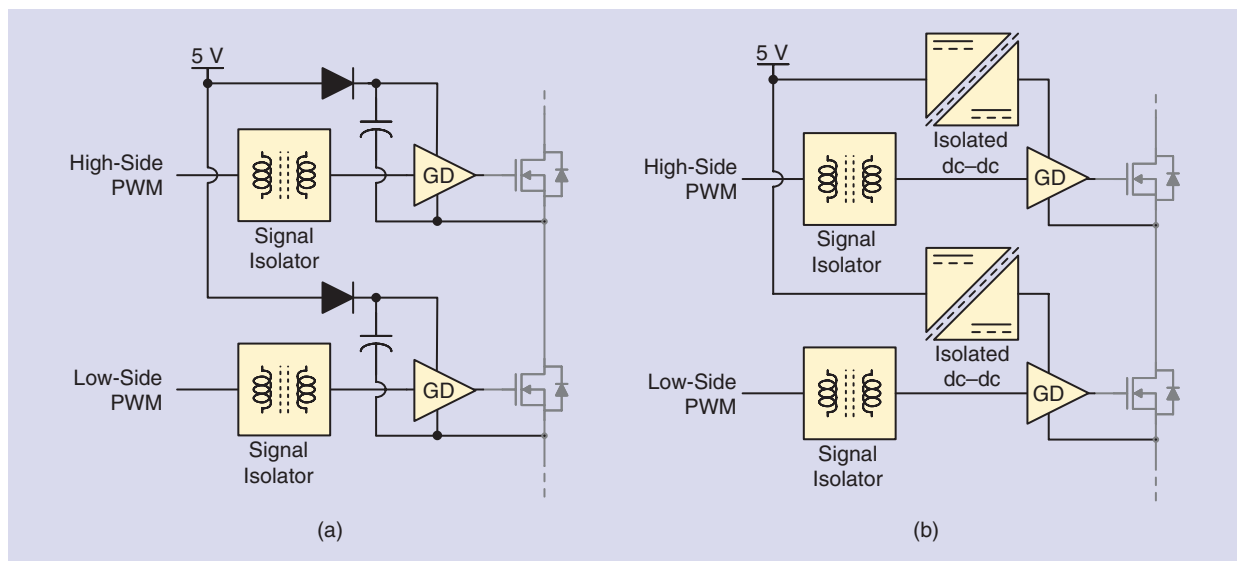


Figure 7. The schematic of two half-bridge gate driving methods. (a) Bootstrapping with a diode and capacitor and (b) generating additional gate-drive (GD) supply rails with isolated dc–dc converters.

acceptable core loss is approximately 500 mW/cm^3 [14]. The circuit designers have various options in the core material selection. In the HF/very HF ranges, air-core magnetic components or powdered-iron toroids are commonly used. For this amplifier design, we utilize the 67 low-permeability ferrite material from Fair-Rite Products Corporation (USA), which demonstrates a high performance factor of roughly 10 MHz [14]. Low-permeability ferrite materials are also available in planar core shapes, making them easy to insert air gaps, which allow fine-tuning of the inductance value. The inductor design in power converters involves determining two terms: number of turns of the winding (N) and length of the air gap l_g [15]. This is assuming that the cores have already been selected. The procedure can be described as follows:

- Determine the maximum B-field based on the saturation limit of the core or the tolerable core loss.
- Determine the peak current ($i_{L,\text{max}}$) through the inductor based on the circuit design.
- Calculate the maximum energy stored in the inductor based on $E_{\text{max}} = (1/2)Li_{L,\text{max}}^2$.
- Determine the minimum l_g based on $E_{\text{max}} = (1/2)(A_c l_c B_{\text{max}}^2 / \mu_c \mu_0) + (1/2)(A_c l_{g,\text{min}} B_{\text{max}}^2 / \mu_0)$, where l_c is the length of the core and A_c is the area of

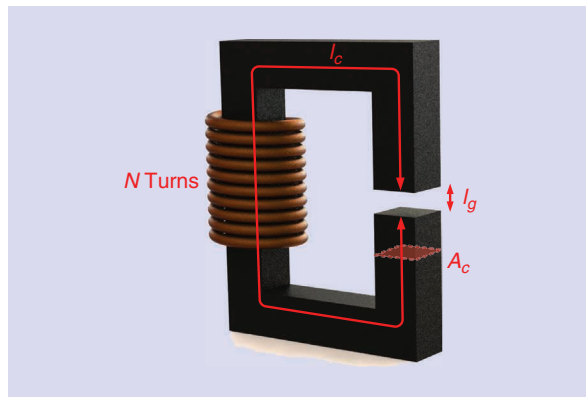


Figure 8. The physical diagram for an inductor design, where N is the number of turns of the winding, l_g is the length of the air gap, l_c is the length of the core, and A_c is the cross-sectional area of the core.

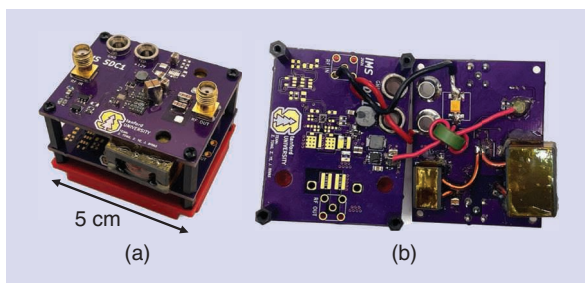


Figure 9. (a) A photo of the PA system. (b) The bottom-side view of the amplifier.

the core, which can be obtained from the core's data sheet.

- Determine the number of turns based on: $N = \sqrt{L(l_g + (l_c/\mu_c))/A_c \mu_0}$, where $l_g \geq l_{g,\text{min}}$ such that N can be a whole number.

The parameters of the core are shown in Figure 8. As there exist various core shapes, data sheets generally provide an effective A_c and l_c for the core.

As an example, we select the 9367053002 planar EQI core from Fair-Rite for the resonant inductor. The core has an effective area of $A_c = 0.61 \text{ cm}^2$ and an effective length $l_c = 2.52 \text{ cm}$. According to Hanson et al, to generate 500 mW/cm^3 at 13.56 MHz, the B-field through the core would be approximately 10 mT [14]. From our LTSPICE simulation, the peak current through the inductor is 1.75 A and the inductance value is 60 nH. Thus, by following the aforementioned procedures,

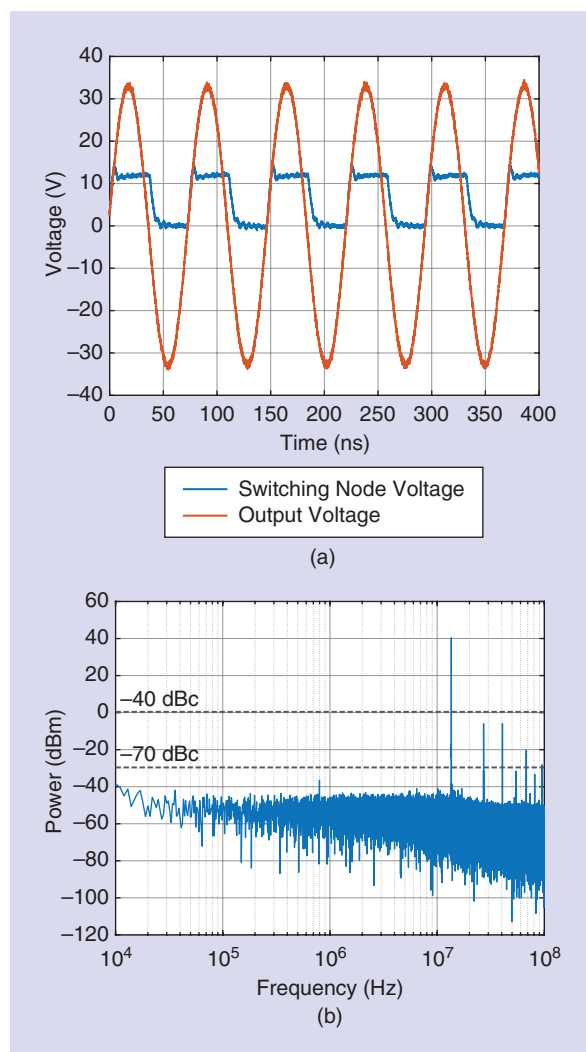


Figure 10. (a) Time-domain waveforms of the measured switching-node voltage of the class-DE amplifier (blue) and measured output voltage. (b) The fast Fourier transform of the output power.

the maximum stored energy of the inductor is 91.9 nJ, resulting in an air-gap length of 0.1 mm and one turn. The series inductor in the class-DE amplifier can be designed in a similar fashion. For this inductor, we selected the 9367054002 EQI core using $N = 2$ and $l_g = 0.2$ mm.

Result

The demonstration of our design is depicted in the photo in Figure 9. In the competition, the amplifier is connected to a 50- Ω load through a coaxial cable. The power delivered to the RF load is measured by a Rhode & Schwarz spectrum analyzer with a bandwidth from 9 kHz to 40 GHz. The recorded power at 13.56 MHz was 10.6 W, and the measured dc input power was 12.18 W. Therefore, the overall efficiency of the converter is 87%. Figure 10(a) displays the measured switching-node voltage waveform and output voltage waveform of the PA using a Keysight DSOX3014T oscilloscope. Finally, Figure 10(b) shows the fast Fourier transform of the output voltage sampled at 10 Gsa/s. The peak at 13.56 MHz corresponds to the fundamental power with the amplitude at roughly 40 dBm. Additionally, the four other peaks above the -70-dBc line in Figure 10(b) correspond to the second, third, fifth, and seventh harmonics, respectively. This satisfies the -70-dBc nonharmonic spurs limitation requirement because all peaks above -70 dBc are harmonics. Furthermore, the peaks that are above -70 dBc are still below -40 dBc, satisfying the harmonic power limitations.

Conclusions

This article summarized the winning design for the High-Efficiency Power Amplifier for 13.56 MHz SDC in IMS 2021. The amplifier featured a class-DE circuit topology using commercial GaN transistors, enabling its high-efficiency performance. As a result, the PA was able to deliver 10.6 W of RF power at 13.56 MHz, achieving 87% total efficiency. We discussed the various design choices that led to the PA's high efficiency, which satisfied the competition criteria, including topology selection, filter and matching network design, auxiliary circuits used to generate alternative dc supply voltages, sine wave-to-PWM conversion, gate-drive selection, and magnetic component design. Although we presented a simple design that can meet the targeted specifications, the efficiency of the PA could likely be further improved through resonant gate-drive techniques that reduce gating loss, and the use of novel passive components such as high-Q, piezoelectric resonators [16], [17], leading to possible future research directions.

Acknowledgments

The authors would like to thank Dr. Frederick Raab for supervising and judging the competition as well as for his helpful feedback. The authors also thank Dr. Lei Gu for 3D printing the base support for the amplifier and the script to design the magnetic components.

References

- [1] F. Raab *et al.*, "HF, VHF, and UHF systems and technology," *IEEE Trans. Microw. Theory Techn.*, vol. 50, no. 3, pp. 888–899, 2002, doi: 10.1109/22.989972.
- [2] W. Liang *et al.*, "Low-mass RF power inverter for cubesat applications using 3-D printed inductors," *IEEE J. Emerg. Select. Topics Power Electron.*, vol. 5, no. 2, pp. 880–890, 2017, doi: 10.1109/JESTPE.2016.2644644.
- [3] L. Gu, G. Zulauf, A. Stein, P. A. Kyaw, T. Chen, and J. M. R. Davila, "6.78-MHz wireless power transfer with self-resonant coils at 95% DC-DC efficiency," *IEEE Trans. Power Electron.*, vol. 36, no. 3, pp. 2456–2460, 2021, doi: 10.1109/TPEL.2020.3014042.
- [4] A. Grebennikov, *RF and Microwave Power Amplifier Design*, 2nd ed. New York, NY, USA: McGraw-Hill, 2015.
- [5] N. O. Sokal and A. D. Sokal, "Class E-a new class of high-efficiency tuned single-ended switching power amplifiers," *IEEE J. Solid-State Circuits*, vol. 10, no. 3, pp. 168–176, Jun. 1975, doi: 10.1109/JSSC.1975.1050582.
- [6] D. Hamill, "Class DE inverters and rectifiers for DC-DC conversion," in *Proc. PESC Rec. 27th Annu. IEEE Power Electron. Specialists Conf.*, 1996, vol. 1, pp. 854–860, doi: 10.1109/PESC.1996.548681.
- [7] S. D. Kee, I. Aoki, A. Hajimiri, and D. Rutledge, "The class-E/F family of ZVS switching amplifiers," *IEEE Trans. Microw. Theory Techn.*, vol. 51, no. 6, pp. 1677–1690, 2003, doi: 10.1109/TMTT.2003.812564.
- [8] L. Gu, G. Zulauf, Z. Zhang, S. Chakraborty, and J. Rivas-Davila, "Push-pull class Φ_2 RF power amplifier," *IEEE Trans. Power Electron.*, vol. 35, no. 10, pp. 10515–10531, 2020.
- [9] "Enhancement mode GaN transistor datasheet," GaN Systems Inc., GS61004B 100V, rev. 200402, 2020.
- [10] "High input voltage, buck-boost converter with 2-A switch current," Texas Instruments, TPS6306x, Nov. 2011.
- [11] Z. Tong, L. Gu, Z. Ye, K. Surakitbovorn, and J. Rivas-Davila, "On the techniques to utilize SiC power devices in high- and very high-frequency power converters," *IEEE Trans. Power Electron.*, vol. 34, no. 12, pp. 12181–12192, 2019, doi: 10.1109/TPEL.2019.2904591.
- [12] Y. Chen, F. Lee, L. Amoroso, and H.-P. Wu, "A resonant MOSFET gate driver with efficient energy recovery," *IEEE Trans. Power Electron.*, vol. 19, no. 2, pp. 470–477, 2004, doi: 10.1109/TPEL.2003.823206.
- [13] C. R. Sullivan, B. A. Reese, A. L. F. Stein, and P. A. Kyaw, "On size and magnetics: Why small efficient power inductors are rare," in *Proc. Int. Symp. 3D Power Electron. Integr. Manuf. (3D-PEIM)*, 2016, pp. 1–23, doi: 10.1109/3DPEIM.2016.7570571.
- [14] A. J. Hanson, J. A. Belk, S. Lim, C. R. Sullivan, and D. J. Perreault, "Measurements and performance factor comparisons of magnetic materials at high frequency," *IEEE Trans. Power Electron.*, vol. 31, no. 11, pp. 7909–7925, Nov. 2016, doi: 10.1109/TPEL.2015.2514084.
- [15] R. W. Erickson and D. Maksimovic, *Fundamentals of Power Electronics*, 2nd ed. Norwell MA, USA: Kluwer, 2001.
- [16] W. D. Braun *et al.*, "Optimized resonators for piezoelectric power conversion," *IEEE Open J. Power Electron.*, vol. 2, pp. 212–224, Mar. 2021, doi: 10.1109/OJPEL.2021.3067020.
- [17] J. D. Boles, J. J. Piel, and D. J. Perreault, "Enumeration and analysis of DC-DC converter implementations based on piezoelectric resonators," *IEEE Trans. Power Electron.*, vol. 36, no. 1, pp. 129–145, 2021, doi: 10.1109/TPEL.2020.3004147.



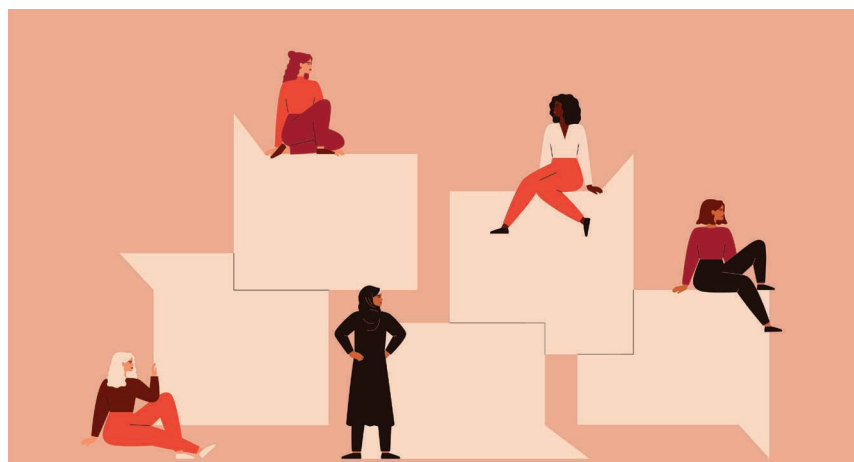


Women in Microwaves

3MT's Positive Impact: Personal and Professional Growth

■ Valentina Palazzi

I took part in the IEEE Microwave Theory and Techniques Society (MTT-S) International Microwave Symposium (IMS) Three Minute Thesis (3MT) competitions twice (Figures 1–3). The first time was at IMS2019. I had just completed my Ph.D. degree and started my postdoctoral work at the University of Perugia, Italy. I did not have an exact idea of what it was about. Soon after my paper was accepted for presentation, I received an email from the 3MT Chairs Erin Kiley and John Bandler, asking me to submit a 30-s video they would use for the selection of the finalists for the 3MT competition. I remember thinking: it is impossible! Three minutes is already too short a time to clearly describe the subject of my paper. The second problem was that we had to avoid technical jargon. Again, this is impossible! My paper concerned a 3D-printed microfluidics-based Butler matrix in coaxial technology. How could I possibly explain what a Butler matrix



or a coaxial cable was without using technical jargon in such a short time?

The beauty of a 3MT competition lies in the simplicity of its rules, which also makes it so tough: all contestants are given a maximum of 3 min to describe the results of their research to a nontechnical audience, with the support of just a single static slide. There is no room for shortcuts: only you, with your words and gestures, must succeed in catching the attention and the interest of a varied audience in less than 3 min, among a number of trained young scientists coming from the best universities and research



Figure 1. The author presenting her 3MT presentation at IMS2019. (Photo courtesy of John Bandler, 3MT cochair.)

Valentina Palazzi (valentina.palazzi@unipg.it) is with the Università degli Studi di Perugia, Perugia, 06123, Italy.

Digital Object Identifier 10.1109/MMM.2021.3132195
Date of current version: 3 February 2022

centers of the world. Unsurprisingly, I was quite daunted.

In retrospect, I must say that the whole journey from the selection among the finalists to the actual presentation in Boston was about removing my misconceptions and disbeliefs. In three months of webinars and one-to-one meetings with our “coaches” Erin and John, I learned that everything is relatable to any kind of audience in any given time amount. The key lies in planning and asking the right questions. Indeed, as I learned, the point was not how to explain a Butler matrix to a nontechnical audience. The point was: Does a nontechnical audience care what a Butler matrix is? Which aspects of my research have an impact on the life of the target audience of my presentation to make them willing to listen to me?

My speech ended up talking about the potential of 3D-printed electronics to improve the performance of next-generation telecommunication systems, which was illustrated by means of a parallelism between electronics and art (my second passion). I would have never imagined I could complete it in less than 3 min.

Sherry Hess, the IEEE MTT-S Women in Microwaves (WIM) subcommittee chair and Master of Ceremonies at the event, recognized how personal and cathartic this speech was for me, and she decided to give me her prize, which made me feel very honored and proud (Figure 4). Receiving support and appreciation from a person whom I sincerely admire meant a lot to me, and it gave me the boost I needed in that moment to pursue my career. I also remember that some people stopped me after the event and asked for additional details on my research, which was thoroughly rewarding.

I decided to apply again two years later, at IMS2021. The topic of my paper was 3D-printed wireless vibration sensors. This time I knew much better what to expect, and I was less worried about turning my work upside down, looking for what could be appealing to the audience. I was actually eager



Figure 2. The IMS2019 3MT competitors; the author is second from left, back row.



Figure 3. -A screenshot from the author's 3MT presentation at IMS2021.



Figure 4. From left: Sherry Hess, John Bandler, and the author at IMS2019.

to try wild metaphors and thought-provoking questions.

Still, there were some new issues to handle. First, the fact that the speech was virtual created unexpected challenges. The room for gestures was reduced with respect to a live speech since we had to stay within the range of the camera. Therefore, walking around was not possible, and every single movement had to be considered and tuned in advance. The videos were prerecorded by the organizers, who gave us a maximum of two shots. So, understanding where to look, which pace to keep, and how to be engaging in the absence of any feedback became very important aspects to study (Figure 3). Although I had had many phone calls and Zoom meetings by that time, just like the rest of the world during the pandemic, I had never paid attention to these aspects, and later on I found them to be very important for effective online communication.

The second challenge was the new format of the training sessions. The one-to-one meetings were replaced by collective training calls with all of the other finalists. The fear of being judged by the other participants

conflicted with my desire to learn and experiment. Fortunately, the latter won, and I actively took part in the sessions. I say “fortunately” for two reasons: first, because I grew a lot together with the others, not only thanks to the feedback that I received, but also by pondering the corrections and observations for the other contestants; and second, because of the unexpected network of relationships that evolved from this experience.

Among the other finalists, there was Yali Zhang, a Ph.D. student at the University of Minnesota, who contacted me at the end of one of the training sessions. She remembered that we were also 3MT finalists at IMS2019, where we had a brief exchange before the performance. She told me that her supervisor, Prof. Rhonda Franklin, was organizing a WIM session at IMS2021 and asked me if I wanted to be part of the team. I said yes and started attending the meetings on Saturday afternoons, where I found some of the most well-known women leaders of our community.

Rhonda asked Yali and me to work together on the second part of the event, which was dedicated to the

current WIMs. She suggested that we interview women leaders in their field to record their vision for the future of microwaves and that we organize the contributions in a video (Figure 5).

What followed was an intensive period, where we alternated 3MT training sessions, in which we were taught how to be effective speakers, with video editing and interview sessions, where we then applied our acquired principles to direct our interviewees. What an incredible experience! I cannot translate into words how inspiring these meetings were. We interviewed ten women leaders—from governments, academic institutions, and companies worldwide—asking them what was “the next big thing” they expected in their research field. Of course, they had a lot to say. One thing that I learned is that nobody is a leader by chance: it requires energy, passion, and vision. But we needed brief answers, of 1 min or shorter, and some of them found it difficult to summarize everything they wanted to say (which was exactly what I thought at the beginning of my 3MT experience). So, we talked with them until we identified the most impactful aspects that had to be included in the video—only then did we proceed with the recording. This way, we could see the power of the 3MT training in action before our eyes.

The icing on the cake of this period was the outcome of the 3MT competition: my prerecorded speech won the second-place award. Considering the high level of the competition, I am very proud of this result and grateful to the judges.

I feel that the 3MT experience left a profound impression on me and on my work. As a nonnative English speaker, it helped me understand a different way of expressing concepts. It gave me a new perspective on how to communicate my results and prepare my lectures. It also offered me the opportunity to get in touch with the wonderful WIM community. I have many fond memories of this experience, of which I am very grateful.



Figure 5. A screenshot from the WIM interview (top row, from left: the author and Yali Zhang).





New Products

■ Ken Mays

Welcome to a further installment of the “New Products” column in *IEEE Microwave Magazine*. In this issue, we present six new items that may be of interest to the RF/microwave and wireless communities.

Anritsu Introduces Rubidium Signal Generator Family

Anritsu Company introduces the Rubidium signal generator family that delivers outstanding signal purity and frequency stability, even at high-output power levels, across a broad frequency range of 9 kHz–43.5 GHz. Coupled with built-in, easy-to-use, at-location frequency and power calibration capability, Rubidium offers exceptional overall utility and long-term value in a broad range of commercial and military/aerospace measurement applications.

Signal purity is critical to a wide range of measurement applications, from radar testing to testing analog-to-digital converters (ADCs) and digital-to-analog converters (DACs). The Rubidium signal generator offers ground-breaking, low, single-sideband

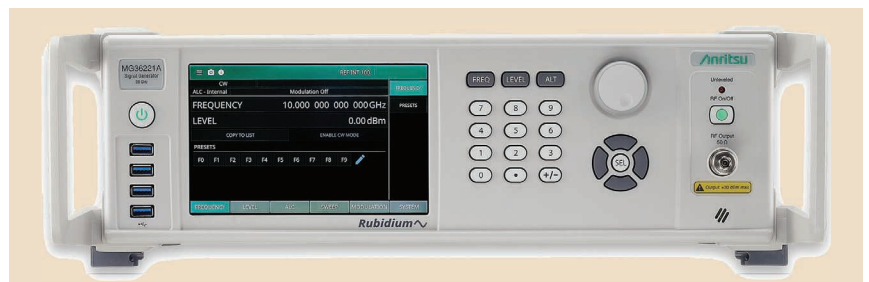
Products listed in *IEEE Microwave Magazine* are restricted to hardware, software, test equipment, services, applications, and publications for use in the science and practice of RF/microwave or wireless engineering. Product information is provided as a reader service and does not constitute endorsement by IEEE or the IEEE Microwave Theory and Techniques Society. Absolute accuracy of listings cannot be guaranteed. Contact information is provided for each product so that interested readers may make inquiries directly.

Please submit “New Products” column information to microwave.newproducts@ieee.org.

(SSB) phase noise of -136 dBc/Hz (typical) and -140 dBc/Hz (measured) at a 10-GHz and 10-kHz offset, respectively, which are unmatched in the industry. Coupled with best-in-class harmonic and spurious performance, the signal generator enables customers to make measurements with better accuracy. The exceptional frequency stability is achieved either by an optional internal Rubidium reference or by locking

the signal generator’s time base to a 1-PPS reference from an optional internal global navigation satellite systems (GNSS)/GPS atomic clock receiver.

The Rubidium signal generator features built-in, on-site frequency and level calibration that is easily accessible with the touch of a button on the GUI interface. This feature ensures customer level, the desired accurate frequency, time savings, enhanced



Digital Object Identifier 10.1109/MMM.2021.3131837
Date of current version: 3 February 2022

convenience, and increased instrument availability. An Anritsu continuous-wave USB power sensor is required for on-site level calibration. An internal GNSS/GPS atomic clock receiver or ultrastability Rubidium time base option is required for on-site frequency calibration.

Rubidium's amplitude-modulation (AM), frequency-modulation (FM)/phase-modulation (PM), and pulse-modulation capabilities enable a wide range of complex, analog-modulated signals. An internal, low-frequency generator can produce seven waveform types to modulate the carrier. Additionally, the simultaneous modulation of AM/FM, AM/PM, or FM/pulse is capable of generating complex modulation waveforms such as chirps. Broad signal simulation capabilities are built into the signal generator for pulsed radar testing.

The signal generator is housed in a 3-U chassis with a 7-inch touch screen on the front panel with a traditional keypad/dial interface. A wide range of options are offered to achieve optimum cost to function and measurement flexibility.

Rubidium can be used in multiple applications. It is ideal for low phase-noise applications, such as testing radar subsystems, up/down converters, or high-speed ADCs/DACs. The signal generator is well suited for conducting nonlinear measurements without additional filters because of the exceptionally low harmonic, subharmonic, and nonharmonic performance at standard and high-output power levels. The instrument can be used for a variety of interference measurements, as a signal source to test devices and systems, and as a frequency reference in calibration and metrology labs.

To learn more, please visit www.anritsu.com.

New Performance Oscilloscope With High Bandwidth and Touchscreen Display

B&K Precision, a leading designer and manufacturer of reliable, cost-effective test and measurement instruments,



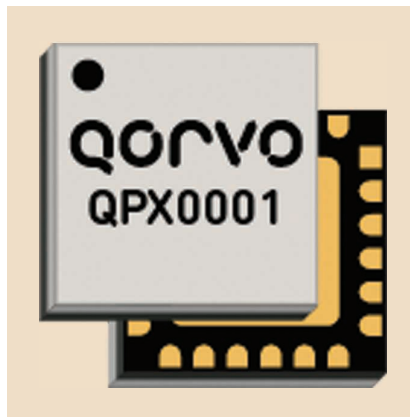
announces the 2560B series, providing up to 350 MHz of bandwidth in a four-channel configuration with power analysis, built-in 50-MHz waveform generator, and serial decoding standard in every model.

The features include a best-in class memory depth of up to 200 Mpts for signal acquisition and 2 Mpts for fast Fourier transform, fast waveform update rates of 120,000 waveforms per second, and a large, 10.1-in capacitive touch display with touchscreen gestures for creating zone triggers and adjusting waveform parameters.

To learn more about the 2560B series and all its features, please visit www.bkprecision.com.

Qorvo Introduces New Compact I/Q Gallium Arsenide Mixer Product Family

Qorvo, a leading provider of innovative RF solutions that connect the world, introduces a family of compact quadrature intermediate frequency mixers, or IQ mixers, which address the needs of wideband and high-frequency applications such as



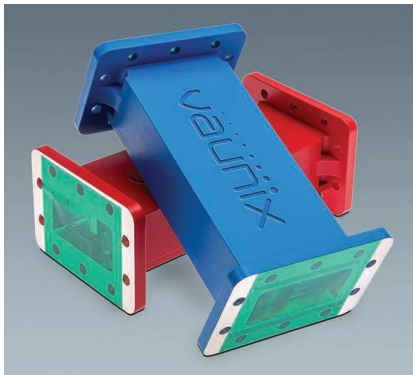
phased-array radar, satellite communications, and electronic warfare. These four new I/Q mixer products, QPX0001, QPX0002, QPX0003D (die), and QPX0004D(die), help to extend and strengthen Qorvo's existing mixer portfolio by delivering industry-leading broadband performance while covering an impressive operating frequency range from 2.5 up to 40 GHz. The products offer excellent image rejection (greater than 20 dB) and are a much smaller alternative to higher-cost, hybrid I/Q mixers and SSB upconverter assemblies.

For inquiries, please visit <https://www.qorvo.com/>.

New 5G-Mitigation Filters Feature 1.1-dB Insertion Loss

Vaunix, a leading provider of wireless system design and testing components and equipment, has announced the release of a new line of red and blue Lab Brick waveguide filters designed for use as 5G interference-mitigation devices in today's complex satellite communication (Satcom) systems. Five C-band models are available in the following popular designated Satcom application frequency bands: 3,780–4,200, 3,820–4,200, 3,900–4,200, 4,000–4,200, and 4,020–4,200 MHz. Each model features an impressive insertion loss of just 1.1 dB, with excellent rejection and return loss characteristics.

As cellular network operators are working to introduce and install advanced 5G, LTE, and WiMax network equipment, a particular design challenge is that high-power C-band 5G systems are now operating around Satcom receivers that also carry critical business communications, television, weather, and other essential services. As a result, next-generation 5G Satcom systems need built-in advanced interference mitigation in their receiver systems using the best RF/microwave waveguide filters to suppress unwanted signals. Installing high-performance 5G-mitigation filters such as these recently introduced by Vaunix will dependably protect against Satcom receiver front-end

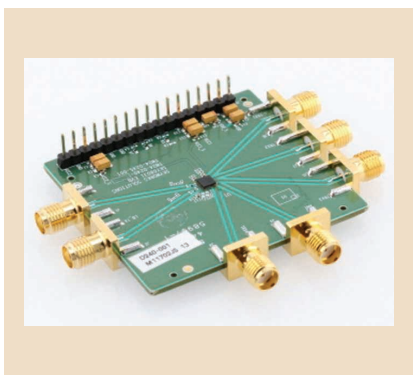


overload (or oversaturation) and result in optimal receiver performance. They are available in easily identifiable red or blue colors to match industry-standardized band designations and feature standard flat or grooved waveguide flanges that address both U.S. (CPR[1]229) and European Union (UDR40, PDR40) standards for interconnectivity.

To learn more, please visit www.vainix.com.

SKY68031-11 Low-Profile, Multiband, Massive Internet of Things Front-End Module

Skyworks is pleased to introduce SKY68031-11, the world's smallest, multiband RF front-end (RFFE) module for licensed, low-power, wide area network [NB-Internet of Things (IoT)] applications including asset tracking, health and fitness wearables, smart metering, and industrial monitoring.



This module integrates the entire RF front-end necessary for a cellular IoT radio operating in low-band (5, 8, 12, 13, 14, 17, 18, 19, 20, 26, 28, and 85) and midband (1, 2, 3, 4, 25, 39, 66, and 70) frequencies. The front-end module monolithically integrates a broadband power amplifier, transmit harmonic filters, antenna switch, and MIPI RFFE controller, all in a compact, 3 × 3-mm package. Up to six different bias conditions can be predefined and programmed through the MIPI interface to optimize power amplifier performance and reduce current consumption.

For more information, please visit www.skyworksinc.com.

Rohde & Schwarz Extends Portable Analyzer Frequency Ranges Up to 44 GHz

Rohde & Schwarz (R&S) has extended its popular R&S Spectrum Rider FPH family with the introduction of new base models offering measurement frequencies up to 44 GHz. A new 44-GHz model has been added to the existing R&S FPH models, which have measurement frequencies from 5 to 6 kHz and from 13.6 to 26.5 GHz. In addition, three new versions with tracking generators are available with measurement frequencies up to 13.6, 26.5, and 44 GHz.

The R&S Spectrum Rider FPH was the industry's first handheld spectrum analyzer to deliver solid RF performance for measurements in the field and in the lab. The large buttons and multitouch gesture screen make it very easy to operate. The new, higher-frequency models enable the versatile R&S Spectrum Rider to perform a broader range of measurement tasks. With high sensitivity of -160 dBm and measurement accuracy of typically 0.5 dB between 10 MHz and 3 GHz, the R&S Spectrum Rider offers class-leading RF performance. The new



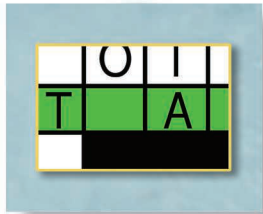
models support field applications such as verification of 5G, broadcast, radar, defense, and satellite communications links.

Weighing just 3.2 kg for the 44-GHz model, the R&S Spectrum Rider is optimized for mobile use. Its battery lasts up to 4.5 h, making it the longest-lasting, 44-GHz, handheld spectrum analyzer for field tasks. The backlit keypad allows users to work in the dark, and the nonreflective display supports a daylight mode for improved readability in direct sunlight.

This handheld spectrum analyzer family boasts a large-format, capacitive touchscreen that makes it easy to intuitively adjust settings such as frequency, span, and reference level, and to set markers. Plus, large buttons and a practical multifunction wheel facilitate operation with gloves in outdoor environments. The analyzer can be remotely controlled via a USB or local area network and, for even more convenience, the R&S MobileView app for iOS or Android provides seamless remote control of the device.

The R&S Spectrum Rider spectrum analyzers are a part of the R&S Essentials portfolio. All the models are now available from Rohde & Schwarz and selected distribution partners. For inquiries, please visit <http://www.rohde-schwarz.com>.





Enigmas, etc.

DC Block and RF Choke

■ Takashi Ohira

To boost the performance of last month's rectifier, we add a dc block capacitor and an RF choke inductor, as shown in Figure 1. Also added is a shunt resistor inside the power source (e.g., $50\ \Omega$ for standard RF generators). Assuming the current source to be $I_1 \cos \omega t$, imagine a picture of the current waveform $i(t)$ flowing down through the shunt resistor. By running a mental-SPICE simulator, which of the following shapes does $i(t)$ exhibit?

- (a) raised cosine
- (b) delayed cosine
- (c) inverted cosine
- (d) truncated cosine.

Takashi Ohira (ohira@tut.jp) is with the Toyohashi University of Technology, Toyohashi, Aichi, 441-8580, Japan. He is a Life Fellow of IEEE.

Digital Object Identifier 10.1109/MMM.2021.3131834
Date of current version: 3 February 2022

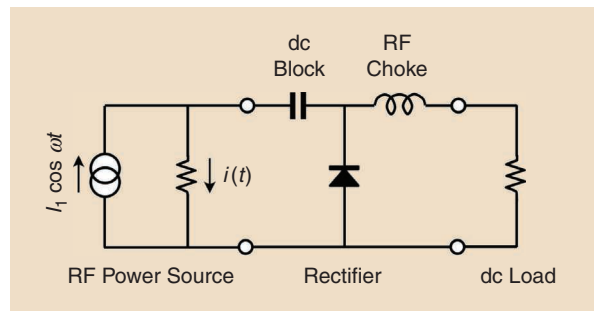


Figure 1. A single-shunt diode rectifier with a dc block and an RF choke.

Note that the dc block capacitance and RF choke inductance are both sufficiently high for simplicity.



Microwave Surfing (continued from page 10)

I am reminded of Mark Twain, who wrote at the end of Chapter 28 of Huckleberry Finn [7]: "...and you pays your money and you takes your choice!"

Acknowledgments

I would like to thank Prof. Kwo Ray Chu of the National University of Taiwan for writing to me about my earlier columns on this topic [3] and sending me a copy of his recent paper on the subject.

References

- [1] A. Fox, "Why sparks fly when you microwave grapes," *Science*. Accessed: Nov. 5, 2021. [Online]. Available: <https://www.sciencemag.org/news/2019/02/why-sparks-fly-when-you-microwave-grapes>
- [2] R. Bansal, "Turnstile: Wrath of grapes," *IEEE Antennas Propag. Mag.*, vol. 61, no. 3, pp. 90–91, Jun. 2019, doi: 10.1109/MAP.2019.2907902.
- [3] R. Bansal, "The wrath of grapes? [Microwave Surfing]," *IEEE Microw. Mag.*, vol. 20, no. 7, pp. 11–12, Jul. 2019, doi: 10.1109/MMM.2019.2909617.
- [4] H. K. Khattak, P. Bianucci, and A. Slepkov, "Linking plasma formation in grapes to microwave resonances of aqueous dimers," *PNAS*.

- Accessed: Nov. 5, 2021. [Online]. Available: <https://www.pnas.org/content/116/10/4000>
- [5] "Top 10 stories of 2019," *Proc. Nat. Acad. Sci. U.S.A.* <https://www.pnas.org/page/topten2019> (accessed Dec. 3, 2021).
 - [6] M. S. Lin, L. C. Chiu, L. R. Barnett, Y. F. Tsai, and K. R. Chiu, "On electromagnetic wave ignited sparks in aqueous dimers," *Phys. Plasmas*, vol. 28, no. 10, p. 102,102, 2021, doi: 10.1063/5.0062014.
 - [7] W. Safire, "On language: You pays yer money," *NY Times Magazine*, Feb. 28, 1988. Accessed: Dec 10, 2021. [Online]. Available: <https://www.nytimes.com/1988/02/28/magazine/on-language-you-pays-yer-money.html>

